2022

Toward A Comprehensive Water Quality Model For The Chesapeake Bay Using Unstructured Grids

Xun Cai
William & Mary - Virginia Institute of Marine Science, nicolecx12@gmail.com

Toward a Comprehensive Water Quality Model for the Chesapeake Bay using Unstructured Grids

---

A Dissertation

Presented to

The Faculty of the School of Marine Science

William and Mary

In Partial Fulfillment

of the Requirements for the Degree of

Doctor of Philosophy

---

by

Xun Cai

May 2022

APPROVAL PAGE

This dissertation is submitted in partial fulfillment of

the requirements for the degree of

Doctor of Philosophy

Xun Cai

Approved by the Committee, January 2022

Y. Joseph Zhang, Ph.D.
Committee Chair / Advisor

Jian Shen, Ph.D.
Committee Co-Chair / Co-Advisor

Mark Brush, Ph.D.

Marjorie A. M. Friedrichs, Ph.D.

Carlton Hershner, Ph.D.

Carl Cerco, Ph.D.
US Army Engineers, retired
Annapolis, MD, USA

TABLE OF CONTENTS

ACKNOWLEDGEMENTS

This dissertation has been made possible by an incredibly supportive network of mentors, colleagues, friends, and family. First and foremost, I would like to express my deepest thanks to my advisors Drs. Joseph Zhang and Jian Shen for their scientific guidance. Also, thanks are due to my committee members Drs. Carl Cerco, Carlton Hershner, Marjy Friedrichs, and Mark Brush for their knowledge and suggestions. I also gratefully acknowledge many colleagues whose questions and comments help to improve this study.

This dissertation benefitted from technical and data support from many individuals. Dr. Eric J. Walter dispensed tremendous technical assistance for using the SciClone cluster at the William and Mary. Drs. James Perry, Donna Bilkovic, Marcia Berman, and other CCRM scientists provided photos and shared their knowledge on the Pamunkey River marshes for the reference. Dr. Dan Yu developed a 30-yr database of physical forcings of the Chesapeake Bay model, which is utilized in this study. The SCHISM developer group, including many intelligent programmers around the world, reviewed my code and model developments when I committed to the Github. Dr. Karinna Nunez helped to map the local bathymetry in the study area. Dr. David Weiss helped with the use of desktops and ArcGIS tools.

This dissertation is financially supported by the VIMS Graduate Research Grants, Virginia Commonwealth Research Fellowship, the California Department of Water Resources (Contract number 4600011601), and in part by an appointment to the Research Participation Program at the Chesapeake Bay Program Office, U.S. Environmental Protection Agency, Region 3 administered by the Oak Ridge Institute for Science and Education through an interagency agreement between the U.S. Department of Energy and U.S. Environmental Protection Agency. Simulations presented in this dissertation were conducted using the computational facility SciClone at the William and Mary which were provided with assistance from the National Science Foundation, the Virginia Port Authority, Virginia's Commonwealth Technology Research Fund, and the Office of Naval Research.

A special thank-you to the VIMS Office of Academic Studies (Dr. Linda Schaffner, Jennifer Hay, Cathy Cake, and John Griffin), Ombud Faculty Dr. Deborah Steinburg, and CCRM Administrative Coordinator Dawn Fleming for being so supportive to me.

The VIMS community has been a supportive group of friends, especially Fei Da, who became my classmate in 2011, and too many to name here, from whom I received tremendous help and joy in life. I am extremely grateful to Mary Margaret and Jim Hutchins for giving me the supports, role models, and company as our American family. I am thankful for the supports from my parents and grandparents. Finally, I thank my husband and best partner Qubin Qin who always helps me face numerous challenges on this path.

ABSTRACT

Chesapeake Bay is one of the most productive ecosystems on the US east coast which supports various living resources and habitat, and therefore has significant impacts on human beings and ecosystem health. Developing the capability of accurately simulating the water quality condition in the Chesapeake Bay, such as seasonal hypoxia, phytoplankton production, and nutrient dynamics, helps to better understand the interactions of hydrodynamical and biochemical processes, and more importantly, to predict conditions under changing climate and human intervention. Currently, most Chesapeake Bay models use structured grids that lack the flexibility for local refinements to fit complex geometry over both large and small scales, which hampers the allocation of local TMDLs for shallow water and small tributaries. In addition, few of them extend their simulations beyond the water column state variables, such as dissolved oxygen and nutrients, to include other living resources such as vegetation. These limitations motivate the model developments in this dissertation of: (1) a new comprehensive water quality model using high-resolution unstructured grids, which possesses the cross-scale capability to study interactions among water bodies and processes of different scales; and (2) a tightly coupled tidal marsh model, which is linked to the water quality model for water column to study the interactions between the marshes and surrounding aquatic system. The new modeling tool can be effectively utilized as a powerful tool for adaptive management in the Chesapeake Bay and can also be exported to other estuaries in the world.

In this dissertation, Chapter 2 focuses on the development of a high-resolution water quality model in the water column and sediment flux part of the water quality model. This part of this study also demonstrates the importance of the correct representation of geometry, and the detrimental effects of artificial bathymetry smoothing on model simulations. Chapter 3 of this dissertation studies the impacts of sea-level rise (SLR) on seasonal hypoxia and phytoplankton production in the Chesapeake Bay with the newly developed water quality model. SLR is predicted to increase the hypoxic volume in the Chesapeake Bay by altering the physical processes and enhancing the estuarine respirations. Phytoplankton production in the shallow shoals is also predicted to increase under SLR, as a result of increased light utilization. Chapter 4 of this dissertation focuses on developing a new marsh model in the hydrodynamic-water quality model framework. This new model extends the model coverage to the tidal wetlands which are periodically inundated. The tidal marshes are suggested to affect the estuarine oxygen, carbon, and nutrient dynamics through tidal exchange, e.g., contributing the diel DO cycle. Chapter 5 studies the impacts of SLR on the biochemical processes in the York River Estuary, a tributary of the Bay that has extensive tidal marshes, with the fully-coupled hydrodynamic-water quality-marsh model. The SLR is predicted to enhance the exchanges between the marshes and the adjacent channel, which in turn further impacts the estuarine biochemical processes.

Toward a Comprehensive Water Quality Model for the Chesapeake Bay using Unstructured Grids

1. Introduction

The Chesapeake Bay (the Bay thereafter) is one of the largest estuaries in the world, whose watershed (166,534 km^2) covers part of six states (New York, Pennsylvania, Delaware, Maryland, Virginia, and West Virginia) and the whole of Washington, D.C. There are 18 million people who live in the watershed, alongside cities, farms, wastewater treatment plants, and industry; human activities thus strongly affect the water quality in the Bay and ecosystem health. Facing the degraded water quality conditions (e.g., eutrophication, hypoxia, SAV habitat loss), the Bay has been the focus of research and environmental restoration programs since 1976 when the U.S. Congress directed the U.S. Environmental Protection Agency to conduct a study of the Bay's water quality and resources (Bockstael et al., 1989). Since then, predictive models have been developed to guide the management of the Bay (Carl and Noel, 2013). One advantage of using numerical models is that, when properly calibrated with observation, they can be used to investigate research questions and evaluate multiple plausible management scenarios. Besides the predictions based on human-Bay intervention, such as the changes in the wastewater loading, the water quality models can also provide guidance on potential mitigation measures for the changing climate.

In the 1990s, Cerco and Cole (1993) started to use a numerical model to help to fill the observation gaps, to quantitively and qualitatively understand the ecological processes and mechanisms in the Bay, and to re-evaluate the nutrient reduction goals. Since then, multiple types of models have been utilized in the Chesapeake Bay, from simplified conceptual or statistical models (e.g., Murphy et al., 2011; Lee et al., 2013) to complex three-dimensional hydrodynamic-biogeochemical models (e.g., Cerco, 1995; Park et al., 1995; Cerco, 2000; Xu and Hood, 2006; Li et al., 2009; Lanerolle et al., 2011; Brown et al., 2013; Testa et al., 2014; Feng et

al., 2015; Xia and Jiang, 2016). In particular, the fully coupled three-dimensional hydrodynamic-biogeochemical models can describe well the nonlinear interactions of various processes and are more frequently used for forecasting and policymaking purposes (Irby et al., 2016). Among the fully coupled 3D numerical models, unstructured-grid (UG) models have the flexibility to resolve the complex coastline, and to use locally fine-resolution grids for small tributaries (Xia and Jiang, 2016). Sufficient resolutions as enabled by unstructured models provide cross-scale capability in capturing more realistically physical processes including those in shallow areas and tributaries, which in turn improves the simulations of water quality variables (Cerco and Noel, 2013; Xia and Jiang, 2016). Thus, the development of a fully-coupled hydrodynamic and water quality model for the Bay using unstructured grids has the potential to significantly improve the current modeling capability and provide better guidance for the management for water quality conditions in dissolved oxygen, water clarity, and chlorophyll.

On particularly useful application of the UG model is found in the shallow waters. Facing the accelerating sea-level rise (SLR) under the changing climate, the shallow regions of the Bay have larger relative changes in local water volume than the mainstem and hence, the local environment in the shallow regions may exhibit greater sensitivity to the SLR. Therefore, a comprehensive water quality model with the shallow waters and intertidal zones well represented would fill in an important knowledge gap that has not properly been addressed so far. The vegetation (e.g., tidal marshes and seagrass) plays an important role in the shallow-water ecosystem (Cerco and Moore, 2001). The roles of vegetation on the aquatic system are complex, as it interacts with hydrodynamics, geomorphology, and biochemical processes. As a result, different types of vegetation models have been developed to simulate one or some of these processes over varying time scales. For example, significant progress has been made in the past

century in simulating the impact of vegetations on flow, wave transformation, and turbulence (Chow, 1959; Shimizu, 1994; Naot et al., 1996; Lopez and Garcia 2001; Wu et al., 2007; Zhang et al., 2020); and the two-way dynamic interactions between vegetation biology and hydrodynamics has been recently incorporated into our water quality model (Cai, 2018; Zhang et al., 2020). Besides modeling the impact of vegetation on hydrodynamics, efforts have also been made on the simulations of the geomorphologic dynamics under SLR, which considers the vegetation biomass, the extent of distribution, and its response to the changing climate. For example, several marsh models focus on the evolution of marshes on a long-term time scale (Morris, 2002; Fagherazzi et al., 2004; Kirwan and Murray, 2007; Marani et al., 2007; Townend et al., 2010). These long-term models mostly focus on the feedback between biomass, elevation, and sedimentation, but not the nutrient dynamics (Morris et al., 2002; Fagherazzi et al., 2012). As a result, this kind of long-term geomorphology model is not usually linked to the water quality models which focus on the phytoplankton and nutrient dynamics in seasonal or annual time scales. On the other hand, Buzzelli et al. (1999) applied a marsh model with focus on the short-term biological interactions between the marsh growth/metabolism and the aquatic system nutrient dynamics. Cerco and Tian (2021) incorporated source/sink terms to represent marsh function in a water quality model. However, this vegetation model is treated as an offline box model, and the biogeochemical dynamics in marshes are not coupled into hydrodynamic-water quality models for system-wide simulations. In general, it is challenging to apply a grid with fine enough resolution to account for the patchiness of the vegetation and interaction between water and vegetation. Ideally, the marsh habitat studies would require the model domain cover the inter-tidal flooding zone as well as the surrounding environment in very high resolution, so the numerical model needs to be sufficiently robust to handle the inundation processes (Zhang et al.,

2016). In the new comprehensive water quality model for the Bay and other estuaries where extensive vegetation exists, we believe it is important to include this type of small-scale biochemical vegetation model to further improve the modeling capability in the shallow regions.

In this dissertation, I developed a new comprehensive water quality model with unstructured grids in the Bay. This new model is calibrated and validated against observations of salinity, chlorophyll-a, dissolved oxygen, nutrients, and phytoplankton productions for the mainstem and major tributaries, based on multiple model skill scores in **Chapter 2**. This chapter also demonstrated the importance of having 1) an accurate representation of bathymetry to correctly predict hypoxia and other processes, and 2) a high-resolution model grid for tributaries to correctly simulate water quality state variables. **Chapter 3** studied the influence of sea-level rise (SLR) on seasonal hypoxia and phytoplankton production in the Bay using the model validated in chapter 2. Besides the SLR effects on the main stem, this chapter emphasized the significant changes of phytoplankton productions in the shallow shoals. The modeling exercise in this chapter indicates that shallow water habitat with multiple primary producers plays an important role in bay water quality and shallow regions such as the intertidal zones should be included in the new comprehensive Bay model. Next, a tidal marsh model is developed in **Chapter 4** that is embedded inside the hydrodynamic-water quality model. Model results suggest that tidal marshes influence the estuarine biochemical processes actively, for example, the marshes affect the local diurnal DO cycle by exporting dissolved organic carbon and high sediment oxygen demand through tidal exchange. **Chapter 5** studies the impacts of SLR on the biochemical processes and tidal marshes in the York River Estuary, a tributary in the lower Bay. SLR is predicted to increase tidal range under SLR and prompt more material exchange between the tidal marshes and the adjacent channel, thus further affect the oxygen, carbon, and nutrient

dynamics. Lessons learned from each study and the future directions to further improve our current knowledge on water quality processes are summarized in **Chapter 6**. The main outcome from this dissertation is a well validated UG hydrodynamic-WQ model that is getting ready for management use by CBPO as their Phase 7 estuarine model.

Literature Cited

Buzzelli, C.P., Wetzel, R.L. and Meyers, M.B., 1999. A linked physical and biological framework to assess biogeochemical dynamics in a shallow estuarine ecosystem. *Estuarine, Coastal and Shelf Science*, *49*(6), pp.829-851.

Cai, X., 2018. *Impact of submerged aquatic vegetation on water quality in cache slough complex, Sacramento-San Joaquin delta: a numerical modeling study*. The College of William and Mary.

Cerco, C.F., 1995. Simulation of long-term trends in Chesapeake Bay eutrophication. *Journal of Environmental Engineering*, *121*(4), pp.298-310.

Cerco, C.F., 2000. Phytoplankton kinetics in the Chesapeake Bay eutrophication model. *Water Quality and Ecosystems Modeling*, *1*(1-4), pp.5-49.

Cerco, C.F. and Cole, T., 1993. Three-dimensional eutrophication model of Chesapeake Bay. *Journal of Environmental Engineering*, *119*(6), pp.1006-1025.

Cerco, C.F. and Moore, K., 2001. System-wide submerged aquatic vegetation model for Chesapeake Bay. *Estuaries*, *24*(4), pp.522-534.

Cerco, C.F. and Noel, M.R., 2013. Twenty-one-year simulation of chesapeake bay water quality using the CE-QUAL-ICM eutrophication model. *JAWRA Journal of the American Water Resources Association*, *49*(5), pp.1119-1133.

Cerco, C.F. and Tian, R., 2021. Impact of Wetlands Loss and Migration, Induced by Climate Change, on Chesapeake Bay DO Standards. *JAWRA Journal of the American Water Resources Association*.

Chow, Te V., 2010. *Applied hydrology*. Tata McGraw-Hill Education.

Bockstael, N.E., McConnell, K.E. and Strand, I.E., 1989. Measuring the benefits of improvements in water quality: the Chesapeake Bay. *Marine Resource Economics*, *6*(1), pp.1-18.

Brown, C.W., Hood, R.R., Long, W., Jacobs, J., Ramers, D.L., Wazniak, C., Wiggert, J.D., Wood, R. and Xu, J., 2013. Ecological forecasting in Chesapeake Bay: using a mechanistic–empirical modeling approach. *Journal of Marine Systems*, *125*, pp.113-125.

Fagherazzi, S., Kirwan, M.L., Mudd, S.M., Guntenspergen, G.R., Temmerman, S., D'Alpaos, A., Van De Koppel, J., Rybczyk, J.M., Reyes, E., Craft, C. and Clough, J., 2012. Numerical models of salt marsh evolution: Ecological, geomorphic, and climatic factors. *Reviews of Geophysics*, *50*(1).

Fagherazzi, S., Marani, M. and Blum, L.K., 2004. *The ecogeomorphology of tidal marshes*. American Geophysical Union.

Feng, Y., Friedrichs, M.A., Wilkin, J., Tian, H., Yang, Q., Hofmann, E.E., Wiggert, J.D. and Hood, R.R., 2015. Chesapeake Bay nitrogen fluxes derived from a land-estuarine ocean biogeochemical modeling system: Model description, evaluation, and nitrogen budgets. *Journal of Geophysical Research: Biogeosciences*, *120*(8), pp.1666-1695.

Irby, I.D., Friedrichs, M.A., Friedrichs, C.T., Bever, A., Hood, R.R., Lanerolle, L.W., Li, M., Linker, L., Scully, M., Sellner, K. and Shen, J., 2016. Challenges associated with modeling low-oxygen waters in Chesapeake Bay: a multiple model comparison. *Biogeosciences*, *13*(7), p.2011.

Lanerolle, L.W.J., Patchen, R.C. and Aikman, F., 2011. The second generation Chesapeake Bay operational forecast system (CBOFS2) model development and skill assessment.

Li, M., Zhong, L. and Harding, L.W., 2009. Sensitivity of plankton biomass and productivity to variations in physical forcing and biological parameters in Chesapeake Bay. *Journal of Marine Research*, *67*(5), pp.667-700.

López, F. and García, M.H., 2001. Mean flow and turbulence structure of open-channel flow through non-emergent vegetation. *Journal of Hydraulic Engineering*, *127*(5), pp.392-402.

Marani, M., D'Alpaos, A., Lanzoni, S., Carniello, L. and Rinaldo, A., 2007. Biologically-controlled multiple equilibria of tidal landforms and the fate of the Venice lagoon. *Geophysical Research Letters*, *34*(11).

Morris, J.T., Sundareshwar, P.V., Nietch, C.T., Kjerfve, B. and Cahoon, D.R., 2002. Responses of coastal wetlands to rising sea level. *Ecology*, *83*(10), pp.2869-2877.

Naot, D., Nezu, I. and Nakagawa, H., 1996. Hydrodynamic behavior of partly vegetated open channels. *Journal of Hydraulic Engineering*, *122*(11), pp.625-633.

Park, K., Kuo, A.Y., Shen, J. and Hamrick, J.M., 1995. A three-dimensional hydrodynamic-eutrophication model (HEM-3D): Description of water quality and sediment process submodels.

Shimizu, Y., 1994. Numerical analysis of turbulent open-channel flow over a vegetation layer using a κ-ε turbulence model. *Journal of Hydroscience and Hydraulic Engineering, JSCE*, *11*(2), pp.57-67.

Testa, J.M., Li, Y., Lee, Y.J., Li, M., Brady, D.C., Di Toro, D.M., Kemp, W.M. and Fitzpatrick, J.J., 2014. Quantifying the effects of nutrient loading on dissolved O2 cycling and hypoxia in Chesapeake Bay using a coupled hydrodynamic–biogeochemical model. *Journal of Marine Systems*, *139*, pp.139-158.

Townend, I., Fletcher, C., Knappen, M. and Rossington, K., 2011. A review of salt marsh dynamics. *Water and Environment Journal*, *25*(4), pp.477-488.

Wu, C.H., Yuan, H. and Young, C.C., 2008. Non-hydrostatic modeling of vegetation effects on wave and flow motions. In *Estuarine and Coastal Modeling (2007)* (pp. 304-321).

Xia, M. and Jiang, L., 2016. Application of an unstructured grid-based water quality model to Chesapeake Bay and its adjacent coastal ocean. *Journal of Marine Science and Engineering*, *4*(3), p.52.

Xu, J. and Hood, R.R., 2006. Modeling biogeochemical cycles in Chesapeake Bay with a coupled physical–biological model. *Estuarine, Coastal and Shelf Science*, *69*(1-2), pp.19-46.

Zhang, Y.J., Gerdts, N., Ateljevich, E. and Nam, K., 2020. Simulating vegetation effects on flows in 3D using an unstructured grid model: model development and validation. *Ocean Dynamics*, *70*(2), pp.213-230.

Zhang, Y.J., Ye, F., Stanev, E.V. and Grashorn, S., 2016. Seamless cross-scale modeling with SCHISM. *Ocean Modelling*, *102*, pp.64-81.

Chapter 2

2. A numerical model study of hypoxia in Chesapeake Bay using an unstructured grid model: validation and sensitivity to bathymetry representation

Published in *JAWRA Journal of the American Water Resources Association*

October 2020

DOI: 10.1111/1752-1688.12887

Abstract

A three-dimensional unstructured-grid hydrodynamic and water quality model (SCHISM-ICM) is applied successfully for the Chesapeake Bay. The model is validated with observations of salinity, chlorophyll-a, dissolved oxygen, nutrients, and phytoplankton productions from the year 1991 to 1995 for the mainstem and some major tributaries, based on multiple model skill scores. Model experiments are conducted to test the importance of having 1) an accurate representation of bathymetry in order to correctly predict hypoxia and other processes, and 2) a high-resolution model grid for tributaries to correctly simulate water quality variables. Comparison with the model experiment results with bathymetry smoothing indicates that bathymetry smoothing, as commonly used for many systems, changes the stratification and lateral circulation pattern, resulting in more salt intrusion into shallow water regions, and an increase of the freshwater age. Consequently, a model with bathymetry smoothing can lead to an unrealistic prediction of the distribution of hypoxia and phytoplankton production. Local grid refinement shows significant improvement of model simulations on local stratification and water quality variables. Overall, the use of a high-resolution unstructured grid model leads to a faithful representation of the complex geometry, and thus a seamless cross-scale capability for simulating water quality processes in the Bay including tributaries and tidal creeks.

2.1 Introduction

As one of the largest and most productive estuaries in the US, Chesapeake Bay plays a significant role in serving wildlife and human beings. The Chesapeake Bay has been continuously affected by human activities, such as urbanization and agricultural overfertilization, which leads to eutrophication and algal blooms (Nixon, 1995). Hypoxia, defined as dissolved oxygen (DO) concentration lower than 2 mg L^{-1}, is one of the severe consequences related to eutrophication and algal blooms (Seliger et al., 1985). In summer, hypoxia of Chesapeake Bay is generally caused by strengthened vertical stratification, accelerated respiration of organic matter sinking from spring bloom, and reduced solubility in warmer water that decreases oxygen supply from the water surface (Taft et al., 1980; Kemp et al., 1992; Murphy et al., 2011). Stratification largely reduces DO vertical exchange, preventing the transport of surface DO-rich water to the bottom; the remineralization of organic matter accumulated in the bottom water and sediment further consumes DO. Furthermore, nutrient fluxes from the bottom sediment induce summer algal bloom that further increases water column respiration. Therefore, seasonal hypoxia has been observed in the Chesapeake Bay since the 1930s (Newcombe and Horne, 1938).

Numerical modeling has been applied to study the complex ecosystem of Chesapeake Bay since the late last century (Cerco, 1995; Cerco and Noel, 2013). Working hand in hand with observation, numerical modeling helps to fill the observation gaps and to quantitively and qualitatively understand the ecological processes and mechanisms (Cerco, 1995). Different types of models have been utilized in the past several decades in Chesapeake Bay, from simplified conceptual or statistical models (Murphy et al., 2011; Lee et al., 2013) to complex three-dimensional hydrodynamic-biogeochemical models (Cerco, 1995; Park et al., 1995; Cerco, 2000; Xu and Hood, 2006; Li et al., 2009; Lanerolle et al., 2010; Brown et al., 2013; Testa et al., 2014;

Feng et al., 2015; Xia and Jiang, 2016). In particular, the fully coupled three-dimensional hydrodynamic-biogeochemical models can describe well the nonlinear interactions of various processes and are more frequently used in forecasting and policymaking (Irby et al., 2016). An inter-model comparison for eight complex models has been conducted by Irby et al. (2016) and they concluded that all these models have similar skills in simulating magnitude and seasonal variability of DO in the mainstem of the Bay. However, the unstructured-grid (UG) models have the flexibility to resolve the complex coastline, and to use locally fine-resolution grids for small tributaries, where Xia and Jiang (2016) showed such an application. Sufficient resolutions as enabled by unstructured models provide cross-scale capability in capturing more realistic physical processes and relevant interactions in shallow areas and tributaries, which in turn improves the simulations of water quality variables (Cerco and Noel, 2013; Xia and Jiang, 2016; Cai et al., 2021). Despite the great promise shown by UG models, significant challenges remained until recently. As explained in Ye et al. (2018), bathymetry representation in models requires further scrutiny as it underpins a model's representation of physical processes such as gravitational circulation and freshwater plume. Another important consideration for water quality simulation is the computational efficiency in the face of high resolution used to resolve small tributaries and creeks, which may exert outsized influence on Bay water quality (Xia and Jiang, 2016). Traditional explicit or split explicit models are limited by stability constraints that require small time steps for high resolution.

SCHISM (Semi-implicit Cross-scale Hydroscience Intergrated System Model) has been applied to the Chesapeake Bay by Ye et al. (2018) with several major improvements from previous models: (1) high-resolution triangular-quadrangular unstructured horizontal grid and novel hybrid vertical grid with shaved cells near the bottom (Zhang et al., 2015), (2) semi-

implicit numerical algorithm which allows relatively large time steps (e.g., 150s in this study) with very fine resolution, and (3) an accurate non-smoothed representation of the original bathymetry (Zhang et al., 2016; Ye et al., 2018). With the high model skill obtained on the simulation of hydrodynamics, in this paper we proceed to couple SCHISM with a water quality model to study the seasonal hypoxia in the Chesapeake Bay, with special attention paid to the importance of accurate representation of bathymetry and its impact on water quality simulation. In section 2.2 we describe the available data, model setup, and analysis methods used in this study. Results of a 5-year (1991 to 1995), selected in this study because they are the primary benchmark management period for EPA) simulation and model skill assessments are presented in section 2.3. In section 2.4, we discuss the effects of non-smoothed bathymetry on model simulations of hypoxia and other related processes. The model's flexibility is demonstrated in a tributary by applying two grids with or without local refinements. A short conclusion is presented in Section 2.5.

2.2 Methods

2.2.1 Available monitoring data and watershed loadings

We utilize the database of water quality monitoring networks from the Chesapeake Bay Program (CBP), in the main Bay and its tributaries since 1984 (http://www.chesapeakebay.net/data). These biogeochemical data are generally measured once (winter) or twice (summer) a month. The measurements are conducted at the surface, above the pycnocline, below the pycnocline, and near the bottom, respectively. There is wide coverage of variables – including nutrients, sediments, planktons, water temperature, salinity and DO. In

addition to this database, long-term observed data used by Harding et al. (2002) is also used in this study for some cross-comparisons to calibrate the modeled phytoplankton production.

The watershed of Chesapeake Bay covers an area of about 167,000 km^2, which includes parts of New York, Pennsylvania, Delaware, Maryland, Virginia, West Virginia, and the District of Columbia (Kemp et al., 2005). The watershed loading information used in this study is from the Phase 6 Watershed Model of the Chesapeake Bay Assessment Tool (CAST; Shenk and Linker, 2013). The top three major sources of freshwater flow into the Bay are the Susquehanna, Potomac, and James Rivers. In terms of volume flux, the upper Bay (mainly the Susquehanna River) contributes 58.93% on average for 1991 to 1995 of the total inflow. The upper Bay watershed loading contributes 60.50% on average of dissolved inorganic nitrogen, and 43.19% of total inorganic phosphorus. Among the years from 1991 to 1995, 1993 and 1994 are two wet years. The maximum spring discharge is over 1.15 km^3/day and the loadings of inorganic phosphorus are over 100,320 kg/year for 1993 and 74,862 kg/year for 1994, respectively, which are more than twice of the other years. The annual loadings of dissolved inorganic nitrogen are 1,633,000 kg/year for 1993 and 1,598,900 kg/year for 1994, respectively, which are about 50% larger than other years (Fig. 2-1).

2.2.2 Model description: SCHISM-ICM

SCHISM (Semi-implicit Cross-scale Hydroscience Integrated System Model, Zhang et al., 2016; schism.wiki) is a derivative product of the original SELFE (Semi-implicit Eulerian Lagrangian Finite Element) model (Zhang and Baptista, 2008). It is an open-source community-supported modeling system based on unstructured grids, designed for seamless simulation of 3D baroclinic circulation across creek-lake-river-estuary-shelf-ocean scales (Zhang et al., 2016). The

main features of SCHISM include a semi-implicit time-stepping scheme applied in a hybrid finite-element and finite-volume framework to solve the Navier-Stokes equations in hydrostatic form, and as a result, the time step is not restricted by the CFL (Courant-Friedrichs-Lewy) condition, thus improving numerical efficiency. The Eulerian-Lagrangian method is used to treat the momentum advection to further boost numerical efficiency and stability. The superior stability afforded by SCHISM and its flexible vertical gridding system (Zhang et al., 2015) allows it to use non-smoothed bathymetry to faithfully represent physical processes; the detrimental effects of bathymetry smoothing as commonly used for terrain-following coordinate models have been documented in Ye et al. (2018).

ICM (Integrated Compartment Model), which is originally developed by the U.S. Army Corps of Engineering (ASCE) Research and Development Center as one of the components of the water quality model package to study the eutrophication processes in the Chesapeake Bay, is a flexible, widely-applicable eutrophication model (Cerco and Cole, 1993). The fully coupled SCHISM-ICM represents a 3D hydrodynamic and eutrophication model, where SCHISM provides physical transport fields and ICM simulates the spatial and temporal distribution of 21 water quality state variables by solving a mass-balance equation for local biological kinetic processes (Park et al., 1995). The local kinetic processes of ICM cover the interactions between phytoplankton, nutrients, and DO in the water column (Fig. 2-2). The photosynthesis of phytoplankton consumes inorganic nutrients and produces DO, while respiration consumes DO and recycles nutrients. Meanwhile, the remineralization of organic nutrients and carbon in the water column further consumes DO. Reaeration provides sources of oxygen from the atmosphere. The sediment flux model developed by DiToro and Fitzpatrick (1993) was incorporated into ICM, which simulates remineralization processes in the sediment (Fig. 2-2).

The sediment flux model is driven by the net settling of particulate organic carbon, nitrogen, phosphorus, and silica from the overlying water column and outputs the sediment oxygen demand (SOD) and inorganic nutrients fluxes into the water column through remineralization processes.

2.2.3 Model setup

The model setup closely follows that for a previous hydrodynamic study presented in Ye et al. (2018). In this study, the grid still covers the entire Bay from Cape Henry near the entrance to the Conowingo Dam in the Susquehanna River. The ocean side is still from Lewes, DE in the north to Beaufort Inlet, NC in the south, but the offshore boundary is cut along the shelf break to boost computational efficiency (Fig. 2-3). The grid contains 27,374 nodes and 43,009 elements. The resolution varies from about 2.4 km for the continental shelf to 550 m for the main channel near the Bay mouth and 250 m for Upper Bay and tributaries, with a minimum grid size of ~100 m. The new flexible vertical grid system LSC^2 (Localized Sigma Coordinates with Shaved Cells) as developed by Zhang et al. (2015) consists of a variable number of levels from deep (52 layers at 1000 m depth) to shallow (11 layers at 6 m depth); the average number of vertical in the whole domain is 33.4.

The model was forced at the open boundary by elevation interpolated from two tide gauges at Lewes, DE and Beaufort, NC, using the inverse distance interpolation method. 15 km around the ocean boundary, salinity, and temperature are nudged to prescribed values as follows, with a maximum relaxation time scale of 1 day. The ocean salinity is nudged to World Ocean Atlas' monthly climatological data. The temperature is nudged to the Simple Ocean Data Assimilation (SODA) from 01/01/1991 to 10/06/1992 (when HYCOM is not available) and

HYCOM from 10/07/1992 to 12/31/1995. As the Gulf Stream cuts through part of the model domain we rely on SODA and HYCOM to bring its signal in and out of the domain. Atmospheric forcing, such as wind and radiation fluxes, is derived from the North American Regional Reanalysis (Mesinger et al., 2006). A non-split time step of 150 s is used in this model. Vertically implicit transport solver TVD^2 (two total variation diminishings; Ye et al., 2016) is applied for the main Bay and ocean part. The horizontal solver uses TVD in the deeper depths (>5 m) and an upwind solver for the shallow depths. The vertical turbulence mixing scheme used in this model is k-k1.

The algal assemblage group, diatom (PB1), green algae (PB2), and cyanobacteria (PB3), along with three groups of carbon, five groups of nitrogen, four groups of phosphorus, chemical oxygen demand and DO, are simulated in the model. A sediment flux model is activated and has been warmed up over 5 years before the simulations. Key parameters are listed in Table 1.

2.2.4 Analysis methods

Besides directly comparing the outputs of physical and water quality variables, we also calculate the phytoplankton production and freshwater age from the Susquehanna River. We integrate over the water column for each element to get the local phytoplankton production:

$$\mathrm{PP} = \sum_{n=1}^{n}(\mathrm{PB1}_n \cdot \mathrm{GP1}_n + \mathrm{PB2}_n \cdot \mathrm{GP2}_n + \mathrm{PB3}_n \cdot \mathrm{GP3}_n) \cdot \mathrm{dep}_n \quad (2\text{-}1)$$

where PP is the phytoplankton production (g C/m^2/day). $\mathrm{PB1}, \mathrm{PB2}, \mathrm{PB3}$ are three groups (diatom, green algae, and cyanobacteria) of phytoplankton carbon-based concentration in this element over each layer respectively (g C/m^3). $\mathrm{GP1}, \mathrm{GP2}, \mathrm{GP3}$ are growth rates of the three phytoplankton groups (day^{-1}), n is layer number and dep is layer thickness (m).

To calculate the age, age tracers are injected from the Susquehanna River. The method is based on the work of Deleersnijder et al. (2001) and Shen and Hass (2004).

2.2.5 Estimation of hypoxic volume

Observed profile DO data at stations (as used by Bever et al., 2013) is interpolated/extrapolated into the current SCHISM UG grid to cover the entire Chesapeake Bay. The DO profiles are firstly interpolated onto 0.1 m vertical resolution with linear interpolation/extrapolation with a minimum value of zero from the surface down to the seabed. And then the interpolated observations of each vertical layer are linearly interpolated horizontally onto every UG grid node. Sensitivity to the UG grid resolution is also tested with convergence achieved within 1% when the resolution is doubted, and therefore the 'observed values' reported here are accurate. The hypoxic layer thickness is calculated at each node and the hypoxic volume at each element is the product of the element area and averaged hypoxic layer thickness among the three/four nodes.

2.3 Model assessment

2.3.1 Salinity and temperature

CBP observations along the transect of the main stem are first used to evaluate model skills (Fig. 2-4). In Fig. 2-4ab, the observations are represented by colored circles so that the model skill is highest if the circles completely disappeared into the background. In addition, observations including other stations from 1991 to 1995 are also used for whole Bay comparisons in the form of a target diagram (Fig. 2-4c). The overall RMSE (Root Mean Square Error) are 2.08 PSU for surface salinity and 2.04 PSU for bottom salinity, respectively, which are

slightly lower than the skill scores reported in Ye et al. (2018). The corresponding RMSE for temperature are 1.47 ºC and 2.05 ºC, respectively, for surface and bottom. Therefore, the model can capture temporal and spatial variabilities reasonably for both salinity and temperature (Fig. 2-4). The transect along the main channel in Fig. 2-4b gives information on the averaged salinity profile. The salinity profile is generally well captured by the model throughout the whole Bay, with slight over-estimations at certain lower-Bay stations (e.g. CB7.3). The stratification in the mid-lower Bay is slightly over-estimated. The bottom salinity distribution as shown in Fig. 2-4a suggests that the model captures the salt intrusion in the channel and shallow areas equally well. Note that while aggregated skill scores such as those shown in Fig. 2-4 and in Irby et al. (2017) are useful first assessment, they often miss important pieces of information on the temporal and 3D variability as well as key processes such as runaway stratification observed in the mid and upper Bay. More detailed comparisons such as CTD profiles are needed to holistically assess qualitative and quantitative skills of the model. These detailed comparisons are omitted here for brevity but can be viewed in Ye et al. (2018) for a different period (2011-4). In general, the model is often able to capture the variability of stratifications both in the main stem and in the tributaries (provided that adequate resolution is used there; cf. Section 2.4.3). This is mostly attributed to a few model features including higher-order monotonic transport, faithful representation of the underlying bathymetry and flexibility as provided by the 3D gridding system.

2.3.2 Water quality state variables and hypoxia

Model predictions of selected water quality state variables are extensively compared with CBP observations along the main channel and in some tributaries in 1991-1995. RMSE, CC

(correlation coefficient), and RE (relative error) are used to assess model errors against observations at both surface and bottom (Table 2-2). Complementing the table of statistics is the time series comparison at typical stations in upper, mid, lower Bay, and some tributaries as shown in Fig. 2-5 and Fig. 2-6.

The model captures the seasonal cycles and inter-annual variability of chlorophyll-a, DO, and NO_3^- (Fig. 2-5). Most spring/summer blooms are captured by the model in terms of both timing and magnitude, although there is some over-estimation of bottom chlorophyll-a when concentration is very low at some stations. DO is reasonably predicted by the model with low RMSE (normalized RMSE close to 0.75 for the surface and close to 0.5 for the bottom), high CC (> 0.65), and low RE (< 20%). The overall RMSE of DO is 1.53 g/m^3 for surface and 1.93 g/m^3 for bottom. The modeled bottom DO correlate well with observations with a slightly delayed recovery in fall (Fig. 2-5). Bottom low DO is captured well at all of the selected typical stations except for over-estimations at CB6.2 and LE3.4. The modeled inorganic nitrogen has high correlations with observations (i.e., CC > 0.65 for surface and > 0.5 for bottom). Surface NO_3^- is well captured by the model at all stations. The modeled total organic nitrogen and total phosphorus have relatively low correlations with observations but low RMSE and RE (Table 2-2), which suggests the modeled values are within a reasonable range of observations. A comparison of the seasonal cycle of phytoplankton production from observations by Harding et al. (2002) suggests that the model shows a sensible cycle and magnitude in different parts of the Bay, with over-estimations for spring and in the upper Bay (Fig. 2-6). However, since the observations are monthly mean values for seventeen years (1982-1998), with uncertainty up to 0.7 g C/m^2/day, the model seems reasonable in predicting the phytoplankton productions.

The hypoxic volume we estimated from observations agrees well with the result from Chesapeake Bay Program volumetric inverse distance squared interpolator program version 4.63 (USEPA, 2003; Bever et al., 2013). And the model reasonably captured the observed hypoxic volume (Fig. 2-7). The difference between model estimation and observation interpolation for averaged hypoxic volume from June to August is mostly smaller than 1 km^3 except for the year 1993 when an extraordinarily large hypoxic volume is observed. The predicted along-channel distributions of summer hypoxia are in good agreement with both synoptic summer surveys and five-year averaged observations (Fig. 2-8). For the synoptic comparison, 20 main stem stations covered by the monitoring cruise are temporally averaged over a 5-day cruise window and then spatially interpolated to generate the along-channel distributions (Fig. 2-8a-e). These plots demonstrate that the model is capable of capturing the key features of the along-channel distributions of hypoxia, including the location of the oxycline. To assess the model's ability to capture the along-channel severity of the hypoxia during Jun. 1 to Sep. 30 of the 5 years, the bottom DO is compared at all main stem stations (Fig. 2-8f). The model results are averaged over a five-day window around each survey. Fig. 2-8f demonstrates a good prediction of the hypoxic zone (< 2 g/m^3) along the main stem, with slight over-estimations of 0.8 to 1.5 g/m^3 for the lower Bay (in the non-hypoxic zone). The comparison of the averaged bottom DO with observations suggests a broad agreement in the upper Bay, shoal area, and major tributaries (Fig. 2-8g-k).

2.4 Discussion

2.4.1 Importance of bathymetry on simulating hypoxia in Chesapeake Bay

2.4.1.1 Model experiment with bathymetry smoothing

One of the reasons for the high model skill of SCHISM on hydrodynamics is attributed to an accurate representation of bathymetry (Ye et al., 2018). Therefore, in this paper, we study the model sensitivity to the bathymetry for water quality variables. A numerical sensitivity experiment, similar to the one shown in Ye et al. (2018), is conducted to expound the importance of bathymetry in predicting hypoxia. In this test, the whole domain is smoothed with a volume-conservative filter (Ye et al., 2018), and the parameter settings are identical for both smoothed and non-smoothed cases. After bathymetry smoothing, the deepest part of the channel is up to 20 m shallower than that in the non-smoothed case, and correspondingly the shoals are deepened up to 13 m in the Eastern Shore of upper mid-Bay, thus effectively reducing the steep channel slopes (Fig. 2-9a-c). In most major tributaries such as the York River and the James River, the difference of the channel depths is up to 5 m, while for the Potomac River, the change is up to 12 m (Fig. 2-9a-c). To clearly show the effects on the vertical structures of state variables, we select one along-channel and three cross-channel transects. The along-channel transect follows the deepest region of its original bathymetry. Three typical cross-channel transects are chosen through the locations of the stations CB3.2, CB5.2, and CB6.4, which are near the Baltimore Harbor, the Potomac River, and the York River, respectively (Fig. 2-9d). The alteration to the bathymetry is clearly seen in these transects: the smoothed case loses much of the deep channel but has deeper shoal areas (Fig. 2-9e-g).

One gross error from the bathymetry smoothing, which is often glossed over, is clearly seen in the profile comparisons such as Fig. 2-9i: the observed and modeled profiles do not

properly align vertically. Obviously, manipulations to force the two depths to be consistent with each other would lead to other artifacts. As shown in both along-channel and cross-channel profiles, there is less salt intrusion over the upper Bay in the main channel with the smoothed bathymetry (Fig. 2-9h, i). For example, the bottom salinity around 39 ^{o}N is about 5 PSU less than the observed bottom salinity (Fig. 2-9i). The two cases result in quite different vertical profiles over the upper Bay channel, with the pycnocline being pushed too high relevant toward the water surface in the smoothed case, mostly due to shallower depth therein (Fig. 2-9hi). In the lower Bay, however, smoothing leads to a larger salt intrusion (Fig. 2-9, 10). The deepened depths in the shoal areas bring in saltier water there, and the reduced slopes increase the lateral exchange of salts and reduces lateral salinity gradients (Fig. 2-9e-g), which is a form of spurious diapycnal mixing (Zhang et al., 2016). The non-smoothed case has much deeper, narrower channels with steeper slopes, which leads to different lateral circulation patterns and sharper shoal-channel contrast (Ye et al., 2018) (Fig. 2-10). In addition, the non-smoothed case has an overall stronger stratification, with a different mixing pattern from the smoothed case (Fig. 2-13a-c). Over the cross-channel transect closed to CB5.2, the non-smoothed case also has increased mixing near the deep slope (Fig. 2-13b). We should remark that depending on the types of bathymetry smoothers used, the trend can be different from what is described here; however, in all cases, there are strong biases in the simulated salinity and lateral circulation patterns, and the shoal-channel contrast is always weakened. This has important implications for ecosystem functions as shown below.

2.4.1.2 Effects of smoothed bathymetry on summer hypoxia

Compare with observations, the non-smoothed case has a much better skill in capturing the hypoxia in the upper Bay (e.g. CB3.2) and major tributaries (e.g. the Potomac), partly because it simulates more accurate stratification and salt intrusion (Fig. 2-11). Insufficient salt intrusion in these areas forbids the capture of hypoxia in the case of smoothed bathymetry (more details of hypoxia in tributaries are discussed in section 2.4.3). An important bias due to smoothing is found in the form of under-estimation of DO in the shoals of mid- and upper Bay, so that it has an unrealistically broad hypoxia area (Fig. 2-11), which is consistent with a broad and uniform salt intrusion pattern (cf. Fig. 2-15; Ye et al., 2018). In the mid-Bay area, the larger lateral circulation brings the low-DO water in the channel to the shoals, resulting in mostly lower DO there if the bathymetry is smoothed (Fig. 2-11). Due to the higher DO in the channel and lower DO in the shoal in the smoothed case than in the non-smoothed case, the total hypoxia volume, however, tends to be underestimated (cf. Fig. 2-18).

2.4.1.3 Effects of smoothed bathymetry on phytoplankton production and nutrient budgets

Smoothing the bathymetry increases the shallow area (depth < 10m) by about 230.5km^2 (2.42%), which brings in more light supply for the whole Bay than the non-smoothed case to support phytoplankton production. The smoothing also decreases the depth of the mixing layer by about 1~2 m that tends to keep the phytoplankton stay near the surface (Fig. 2-17cd). As a result, in the smoothed case, the phytoplankton production increases to more than 0.7 g C/m^2/day (Fig. 2-12). In addition, the maximum phytoplankton production occurs in the channel slope between channel and shoal in non-smoothed case. This is because the areal phytoplankton production is limited by local volume and residence time (Qin and Shen, 2017), and a sufficient

large water depth is required to reach a high value. Another reason is that the shallow area often has a water depth less than the depth of euphotic zone, which limits phytoplankton to fully explore the light resource and hence limits the phytoplankton production (Cai et al., 2021). In the smoothed case, this region encroaches parts of the channel due to reduced slope.

Change of phytoplankton production can affect the annual budget of nutrients. To take total dissolved inorganic nitrogen as an example, the large depth-averaged concentration of channels in upper Bay spreads out to the shoal areas. Since most of the increase of phytoplankton production happens in upper Bay in the smoothed case, more DIN is consumed in this region. In the smoothed case, there is a decrease of about 0.1 g N/m^3 for depth-averaged DIN concentration in lower Bay. In terms of the whole water column, the decrease is about 1~3 g N/m^2.

Although the change in total production or total DIN budget is minor, bathymetry smoothing can make a difference up to more than 150% on production and 100% on DIN concentration in some shallow areas, which alternates the local distribution and events.

Freshwater age is another key indicator for assessing the impact of hydrodynamics and physical transport on the local biological processes. Compared to the non-smoothed case, the age of freshwater from Susquehanna River increases up to 40 days over the main Bay in the smoothed case (Fig. 2-13c). Typically in the James River, which is located closer to the bay mouth, an easier intrusion of aged water increases the water age towards the river head. While in the Rappahannock River, Choptank River, and Eastern Shore, where freshwater inflow is relatively small, smoothing induces more mixing which largely decreases the age of water in this region. Overall for the whole Bay, in the smoothed case the annually-averaged age at Bay mouth increases 9~40 days (Fig. 2-13e). This indicates a decrease of gravitational circulation in the smoothed case. The calculated total nitrogen export ratio (25 – 40%) for without smoothing case

is within a reasonable range from literature (Nixon et al., 1996). Wet year has smaller freshwater age along with larger nutrient export. The smoothed grid makes a difference of 2~14% on total nitrogen export ratio, with large effects from wet or dry years (Fig. 2-13d).

2.4.2 Grid refinement in a tributary

Baltimore Harbor is chosen for refinement because of its narrow channel and known severe hypoxia during summertime. While the narrow channel is often 'widened' under bathymetry smoothing, we refined the grid to capture this key feature in the system. A finer grid is generated for the shipping channels in order to better capture the saltwater intrusion: the horizontal resolution is refined to ~300m x ~100m in the along- and cross-channel directions, compared to ~500m x ~250m in the original grid (Fig. 2-14). The implicit scheme used in SCHISM ensures no penalty on the time steps (i.e. same time step is used for both grids).

Stronger salt intrusion to Baltimore Harbor is obtained with grid refinement. The known hypoxia in Baltimore Harbor is not simulated for the case of original grid and smoothed case, though the original non-smoothed one already simulated a clearer channel shape low-DO region than the smoothed case. The refined version has a clearer shape of hypoxia over this region (Fig. 2-15). The seasonal variations of the refined case in Fig. 2-16, compared with the original case, shows significant improvement. The original grid was not able to simulate the stratification inside the harbor well, so that there is little difference between the surface and the bottom chlorophyll-a in the original case. It has an over-estimated depth-averaged value and is not able to capture much of the observed surface algal blooms. In addition, the lack of strong stratification in the original grid also provides a significant amount of reaeration for bottom DO. The simulation of surface NO_3^- is also larger than observation but still has sensible inter-annual

variations in the case of the original grid. Refinement of tributary resolution improves the simulation of physical transport, stratification, and therefore the relevant water quality variables. This sensitivity test tells the next step to refine the unstructured grid into small tributaries with non-smoothed bathymetry is a sensible direction with relatively low cost of computational efficiency (5% increased computational time in the refined case due to the increased grid size).

2.4.3 Estimation of the effects of sea-level rise with non-smoothed bathymetry

We will briefly discuss the impact of bathymetry smoothing on the prediction of the trend under Sea Level Rise (SLR) for salinity and DO here and leave the more detailed discussion to the sequel paper (Cai et al., 2021). The SLR effects consist of both physical effects on the estuarine circulation, salt intrusion, and flooding, and indirect effects on hypoxia and biogeochemical processes.

Two SLR (+0.5m) cases are conducted based on the two cases (non-smoothed and smoothed) discussed in section 2.4.1. The increase of 0.5m is applied at the ocean boundary while the rest of the model setup is kept the same.

Overall, the smoothed case predicts larger salt intrusion caused by SLR (Fig. 2-17ab). In the non-smoothed case, the average increase is 0.79 PSU over the transect along the main channel and 0.81 PSU for the bottom salinity of the Bay; these are increased by 22.8% and 13.6%, respectively, under the smoothed case. The predicted increase of salt intrusion is more uniform both vertically and horizontally over the main stem in the case of smoothed bathymetry, while in the case of non-smoothed bathymetry, the increase of salinity is mostly concentrated in the upper 10m of the water column (thus moving the halocline upward), and a less increase occurs in the deep channels (Fig. 2-17ab). Along the main channel, the largest increase of

salinity occurs near 39.25°N (CB3.2; Fig. 2-17a). More exaggerated changes occur in some tributaries for the case of smoothed bathymetry, and the salinity even decreases in some western tributaries (Fig. 2-17b). These changes are highly questionable, which demonstrates the significance of using the unsmoothed representation of bathymetry with the UG grid in the SLR study (Cai et al., 2021).

The total hypoxia volume tends to be underestimated in the smoothed case by up to 3 km^3 (~2 km^3 for the July period) (Fig. 2-18a). More importantly, the change in the hypoxic volume due to SLR is exaggerated by ~2.5 km^3 (or 100% off) for the July period (Fig. 2-18b). This is consistent with the exaggerated change in salt intrusion in the entire system (Fig. 2-17).

2.4.4 Model uncertainties and limitations

We briefly discuss the remaining model uncertainties. Due to the scarcity of observations outside the Bay, there are uncertainties associated with the open boundary conditions, although we have partially mitigated this by extending the domain to the shelf break. To assess the uncertainties, we compare results from the base with some extreme/unrealistic tests. In the first test, algae are not allowed to grow outside the Bay, since we usually assign the same groups and parameters for the algae in/outside the Bay. In the second and third tests, we increase the averaged total inorganic phosphorus (TIP) concertation from 0.035g/m^3 to 0.06g/m^3 and decrease it to 0.01g/m^3, respectively, at the boundary. The two tests are used to investigate the impact of the net influx of phosphorus from the Bay mouth on the DO dynamics in the Bay, since it has been suggested that the coast input of phosphorus has a significant effect on the phytoplankton production in estuarine systems (Nixon et al., 1996).

Our results show little effect from the changes in the boundary conditions on the simulated summer hypoxia over the upper Bay, with an overall difference of less than $0.6g/m^3$ in winter (Fig. 2-19). The middle Bay and lower Bay receive a greater influence, but the difference is basically smaller than $1g/m^3$. If there is no algal growth outside the Bay, there will be less oxygen consumption inside the Bay except for the region closed to the mouth. Increasing or decreasing outside particulate inorganic phosphorus (PIP) slightly decreases or increases bottom DO concertation in most regions except for the area closed to the Bay mouth. Decreasing boundary inorganic phosphorus causes a larger change on bottom oxygen concertation than increasing it in most of the Bay areas, which indicates that phosphorus is limited inside the hypoxia zone. Overall, the influence of boundary conditions at the shelf break seems minor.

In this study, the three groups of phytoplankton are the only primary producers in the model. Besides phytoplankton, other primary producers, such as benthic algae, marsh, SAV (submerged aquatic vegetation), and macroalgae could play a significant role over shallow areas under certain conditions (Qin and Shen, 2019). The potential contributions of other producers, especially for shallow areas are not included since the focus here is the main stem. An SAV model has already been developed inside the framework of SCHISM-ICM (Cai, 2018; Zhang et al., 2019) and others may be added in the future.

2.5 Summary and conclusion

We have successfully applied the SCHISM-ICM to the simulation of water quality awith a focus of hypoxia in Chesapeake Bay. The model shows a good performance in simulating dynamics of water quality variables such as chlorophyll-a, DO, nutrients, and phytoplankton

productions. The bias of estimated hypoxic volume from model and observation is generally smaller than 1 km^3.

Sensitivity test results with bathymetry smoothing are found to be fundamentally inaccurate. Bathymetry smoothing alters the physical environment of the system, and hence has cascade implications on the simulations of the ecosystem, including over-estimation of bottom DO in the channel and tributaries and under-estimation over the shoal. The smoothing also increases depths of shallow-water areas, and leads to an increase in phytoplankton production up to 150% in some localized areas and a difference of 2-14% in nutrient export, partly due to the increased freshwater age. Comparisons with observations clearly demonstrate that it is important to use realistic bathymetry (with aid from high resolution) to provide accurate simulations for physical and biogeochemical processes, and to correctly predict the impact of sea-level rise on future summertime hypoxia, which is of great concern for the Bay management. The seamless cross-scale capability of SCHISM-ICM, together with its efficiency and robustness, can be effectively utilized as a powerful tool for adaptive management.

Literature Cited

Bever, A.J., M.A. Friedrichs, C.T. Friedrichs, M.E. Scully and L.W. Lanerolle. 2013. "Combining Observations and Numerical Model Results to Improve Estimates of Hypoxic Volume Within the Chesapeake Bay, USA." *Journal of Geophysical Research: Oceans*, *118*(10), pp.4924-4944. https:// doi.org/10.1002/jgrc.20331

Brown, C.W., R.R. Hood, W. Long, J. Jacobs, D.L. Ramers, C. Wazniak, J.D. Wiggert, R. Wood and J. Xu. 2013. "Ecological Forecasting in Chesapeake Bay: Using A Mechanistic–Empirical Modeling Approach." *Journal of Marine Systems*, *125*, pp.113-125. https://doi.org/10.1016/j.jmarsys.2012.12.007

Cai, X., 2018. "Impact of Submerged Aquatic Vegetation on Water Quality in Cache Slough Complex, Sacramento-San Joaquin Delta: A Numerical Modeling Study." Master thesis, College of William and Mary. http://dx.doi.org/10.25773/v5-8snw-1660

Cai, X., Shen, J., Zhang, Y.J., Qin, Q., Wang, Z. and Wang, H., 2021. Impacts of Sea-Level Rise on Hypoxia and Phytoplankton Production in Chesapeake Bay: Model Prediction and Assessment. *JAWRA Journal of the American Water Resources Association*. https://doi.org/10.1111/1752-1688.12921

Cerco, C.F., 1995. "Simulation of Long-Term Trends in Chesapeake Bay Eutrophication." *Journal of Environmental Engineering*, *121*(4), pp.298-310. https://doi.org/10.1061/(ASCE)0733-9372(1995)121:4(298)

Cerco, C.F., 2000. "Phytoplankton Kinetics in the Chesapeake Bay Eutrophication Model." *Water Quality and Ecosystems Modeling*, *1*(1-4), pp.5-49. https://doi.org/10.1023/A:1013964231397

Cerco, C.F. and T.M. Cole. 1994. “CE-QUAL-ICM: a three-dimensional eutrophication model, version 1.0. User’s Guide.” *US Army Corps of Engineers Waterways Experiments Station, Vicksburgh, MS*.

Cerco, C.F. and M.R. Noel. 2013. “Twenty-one-year Simulation of Chesapeake Bay Water Quality Using the CE-QUAL-ICM Eutrophication Model.” *JAWRA Journal of the American Water Resources Association*, *49*(5), pp.1119-1133. https://doi.org/10.1111/jawr.12107

Deleersnijder, E., J.M. Campin and E.J. Delhez. 2001. “The Concept of Age in Marine Modelling: I. Theory and Preliminary Model Results.” *Journal of Marine Systems*, *28*(3-4), pp.229-267. https://doi.org/10.1016/S0924-7963(01)00026-4

Di Toro, D.M. and J.J. Fitzpatrick. 1993. “*Chesapeake Bay sediment flux model. Final report* (No. AD-A-267189/9/XAB).” Hydroqual, Inc., Mahwah, NJ (United States).

Feng, Y., M.A. Friedrichs, J. Wilkin, H. Tian, Q. Yang, E.E. Hofmann, J.D. Wiggert and R.R. Hood. 2015. “Chesapeake Bay Nitrogen Fluxes Derived from A Land-Estuarine Ocean Biogeochemical Modeling System: Model Description, Evaluation, and Nitrogen Budgets.” *Journal of Geophysical Research: Biogeosciences*, *120*(8), pp.1666-1695. https://doi.org/10.1002/2015JG002931

Harding Jr, L.W., M.E. Mallonee and E.S. Perry. 2002. “Toward a Predictive Understanding of Primary Productivity in a Temperate, Partially Stratified Estuary.” *Estuarine, Coastal and Shelf Science*, *55*(3), pp.437-463. https://doi.org/10.1006/ecss.2001.0917

Irby, I.D., M.A. Friedrichs, C.T. Friedrichs, A. Bever, R.R. Hood, L.W. Lanerolle, M. Li, L. Linker, M. Scully, K. Sellner and J. Shen. 2016. “Challenges Associated with Modeling

Low-Oxygen Waters in Chesapeake Bay: A Multiple Model Comparison." *Biogeosciences*, *13*(7), p.2011. doi:10.5194/bgd-12-20361-2015

Kemp, W.M., W.R. Boynton, J.E. Adolf, D.F. Boesch, W.C. Boicourt, G. Brush, J.C. Cornwell, T.R. Fisher, P.M. Glibert, J.D. Hagy and L.W. Harding. 2005. "Eutrophication of Chesapeake Bay: Historical Trends and Ecological Interactions." *Marine Ecology Progress Series*, *303*, pp.1-29. doi:10.3354/meps303001

Kemp, W.M., P.A. Sampou, J. Garber, J. Tuttle and W.R. Boynton. 1992. "Seasonal Depletion of Oxygen from Bottom Waters of Chesapeake Bay: Roles of Benthic and Planktonic Respiration and Physical Exchange Processes." *Marine Ecology Progress Series*, pp.137-152. www.jstor.org/stable/24829928

Lanerolle, L.W., R.C. Patchen and F. Aikman. 2010. "The Second Generation Chesapeake Bay Operational Forecast System (CBOFS2): A ROMS-Based Modeling System." *Estuarine and Coastal Modeling (2009)* (pp. 621-642). https://doi.org/10.1061/41121(388)37

Lee, Y.J., W.R. Boynton, M. Li and Y. Li. 2013. "Role of Late Winter–Spring Wind Influencing Summer Hypoxia in Chesapeake Bay." *Estuaries and coasts*, *36*(4), pp.683-696. doi: 10.1007/s12237-013-9592-5

Li, M., L. Zhong and L.W. Harding. 2009. "Sensitivity of Plankton Biomass and Productivity to Variations in Physical Forcing and Biological Parameters in Chesapeake Bay." *Journal of Marine Research*, *67*(5), pp.667-700. https://doi.org/10.1357/002224009791218878

Mesinger, F., G. DiMego, E. Kalnay, K. Mitchell, P.C. Shafran, W. Ebisuzaki, D. Jović, J. Woollen, E. Rogers, E.H. Berbery and M.B. Ek. 2006. "North American Regional

Reanalysis." *Bulletin of the American Meteorological Society*, *87*(3), pp.343-360. https://doi.org/10.1175/BAMS-87-3-343

Murphy, R.R., W.M. Kemp and W.P. Ball. 2011. "Long-term Trends in Chesapeake Bay Seasonal Hypoxia, Stratification, and Nutrient Loading." *Estuaries and Coasts*, *34*(6), pp.1293-1309. doi: 10.1007/s12237-011-9413-7

Newcombe, C.L. and W.A. Horne.1938. Oxygen-poor Waters of the Chesapeake Bay. *Science*, *88*(2273), pp.80-81. doi: 10.1126/science.88.2273.80

Nixon, S.W., 1995. "Coastal Marine Eutrophication: A Definition, Social Causes, and Future Concerns." *Ophelia*, *41*(1), pp.199-219. https://doi.org/10.1080/00785236.1995.10422044

Nixon, S.W., J.W. Ammerman, L.P. Atkinson, V.M. Berounsky, G. Billen, W.C. Boicourt, W.R. Boynton, T.M. Church, D.M. Ditoro, R. Elmgren and J.H. Garber. 1996. "The Fate of Nitrogen and Phosphorus at the Land-Sea Margin of the North Atlantic Ocean." *Biogeochemistry*, *35*(1), pp.141-180. https://doi.org/10.1007/BF02179826

Park, K., A.Y. Kuo, J. Shen and J.M. Hamrick. 1995. "A Three-Dimensional Hydrodynamic-Eutrophication Model (HEM-3D): Description of Water Quality and Sediment Process Submodels." Special report in applied marine science and ocean engineering, no. 327. Virginia Institute of Marine Science, College of William and Mary. https://doi.org/10.21220/V5ZH9N

Qin, Q. and J. Shen. 2017. "The contribution of local and transport processes to phytoplankton biomass variability over different timescales in the Upper James River, Virginia."

Estuarine, Coastal and Shelf Science, *196*, pp.123-133. https://doi.org/10.1016/j.ecss.2017.06.037

Qin, Q. and J. Shen. 2019. "Pelagic Contribution to Gross Primary Production Dynamics in Shallow Areas of York River, VA, USA." *Limnology and Oceanography*, *64*(4), pp.1484-1499. https://doi.org/10.1002/lno.11129

Seliger, H.H., J.A. Boggs and W.H. Biggley. 1985. "Catastrophic Anoxia in the Chesapeake Bay in 1984." *Science*, *228*(4695), pp.70-73. doi: 10.1126/science.228.4695.70

Shen, J. and L. Haas. 2004. "Calculating Age and Residence Time in the Tidal York River Using Three-Dimensional Model Experiments." *Estuarine, Coastal and Shelf Science*, *61*(3), pp.449-461. https://doi.org/10.1016/j.ecss.2004.06.010

Shenk, G.W. and L.C. Linker. 2013. "Development and Application of the 2010 Chesapeake Bay Watershed Total Maximum Daily Load Model." *JAWRA Journal of the American Water Resources Association*, *49*(5), pp.1042-1056. https://doi.org/10.1111/jawr.12109

Taft, J.L., W.R. Taylor, E.O. Hartwig and R. Loftus. 1980. "Seasonal Oxygen Depletion in Chesapeake Bay." *Estuaries*, *3*(4), pp.242-247. http://www.jstor.com/stable/1352079

Testa, J.M., Y. Li, Y.J. Lee, M. Li, D.C. Brady, D.M. DiToro, W.M. Kemp and J.J. Fitzpatrick. 2014. "Quantifying the Effects of Nutrient Loading on Dissolved O2 Cycling and Hypoxia in Chesapeake Bay Using A Coupled Hydrodynamic–Biogeochemical Model." *Journal of Marine Systems*, *139*, pp.139-158. https://doi.org/10.1016/j.jmarsys.2014.05.018

Xia, M. and L. Jiang. 2016. "Application of An Unstructured Grid-Based Water Quality Model to Chesapeake Bay and its Adjacent Coastal Ocean." *Journal of Marine Science and Engineering*, *4*(3), p.52. https://doi.org/10.3390/jmse4030052

Xu, J. and R.R. Hood. 2006. "Modeling Biogeochemical Cycles in Chesapeake Bay with a Coupled Physical–Biological Model." *Estuarine, Coastal and Shelf Science*, *69*(1-2), pp.19-46. https://doi.org/10.1016/j.ecss.2006.03.021

Ye, F., Y.J. Zhang, M.A. Friedrichs, H.V. Wang, I.D. Irby, J. Shen and Z. Wang. 2016. "A 3D, Cross-Scale, Baroclinic Model with Implicit Vertical Transport for the Upper Chesapeake Bay and its Tributaries." *Ocean Modelling*, *107*, pp.82-96. https://doi.org/10.1016/j.ocemod.2016.10.004

Ye, F., Y.J. Zhang, H.V. Wang, M.A. Friedrichs, I.D. Irby, E. Alteljevich, A. Valle-Levinson, Z. Wang, H. Huang, J. Shen and J. Du. 2018. "A 3D Unstructured-Grid Model for Chesapeake Bay: Importance of Bathymetry." *Ocean Modelling*, *127*, pp.16-39. https://doi.org/10.1016/j.ocemod.2018.05.002

Zhang, Y.J., E. Ateljevich, H.C. Yu,, C.H. Wu and C.S. Jason. 2015. "A New Vertical Coordinate System for a 3D Unstructured-Grid Model." *Ocean Modelling*, *85*, pp.16-31. https://doi.org/10.1016/j.ocemod.2014.10.003

Zhang, Y. and A.M. Baptista. 2008. "SELFE: A Semi-Implicit Eulerian–Lagrangian Finite-Element Model for Cross-Scale Ocean Circulation." *Ocean modelling*, *21*(3-4), pp.71-96. https://doi.org/10.1016/j.ocemod.2007.11.005

Zhang, Y.J., N. Gerdts, E. Ateljevich, and K. Nam. 2020. "Simulating Vegetation Effects on Flows in 3D Using an Unstructured Grid Model: Model Development and

Validation." *Ocean Dynamics*, *70*(2), pp.213-230. https://doi.org/10.1007/s10236-019-01333-8

Zhang, Y.J., F. Ye,, E.V. Stanev and S. Grashorn. 2016. "Seamless Cross-Scale Modeling with SCHISM." *Ocean Modelling*, *102*, pp.64-81. https://doi.org/10.1016/j.ocemod.2016.05.002

Tables for Chapter 2

Table 2-1: Key parameters of ICM used in this study.

Parameter	Unit	Value		
Algae		***PB1***	***PB2***	***PB3***
Maximum growth rate	day^{-1}	3.5	2.4	1.5
Optimal temperature for growth	ºC	10	20	27
Carbon to Chlorophyll a ratio	g C per g Chl	50	60	60
Basel metabolism rate at temperature of 20 ºC	day^{-1}	0.02	0.02	0.04
Predation rate at temperature of 20 ºC	day^{-1}	0.3	0.2	0.1
Settling velocity	m day-1	0.6	0.4	0.075
Half saturation of nitrogen	g N m^{-3}	0.01	0.01	0.01
Half saturation of phosphorus	g P m^{-3}	0.001	0.001	0.001
Nutrients		***Carbon***	***Nitrogen***	***Phosphorus***
Dissolution/Hydrolysis rate of RPOM	day^{-1}	0.01	0.005	0.01
Dissolution/Hydrolysis rate of LPOM	day^{-1}	0.045	0.075	0.05
Heterotrophic respiration/Mineralization rate of DOM	day^{-1}	0.04	0.11	0.05
Settling velocity of POM	m day-1	0.4	0.4	0.4
Maximum nitrification rate at temperature of 24 ºC	g N m^{-3} day^{-1}	-	0.1	-

Table 2-2: Root mean square error (RMSE), correlation coefficient (CC) and relative error (RE) for model-data comparisons of certain water quality state variables from 1991 to 1995. Model outputs are interpolated onto the corresponding observation times at both surface and bottom to calculate the metrics (NaN due to insufficient amount of observations).

Region	*Station*	*Index*	*Layer*	*SAL*	*CHL*	*DO*	*NO_3^-*	*DIN*	*TON*	*TP*
Upper Bay	CB3.3C	RMSE	S	2.84	23.02	2.11	1.80	0.20	0.23	2.84
			B	2.06	19.12	2.41	2.32	0.13	0.19	2.06
		CC	S	0.89	-0.07	0.66	0.28	0.87	0.85	0.89
			B	0.73	0.12	0.75	-0.05	0.70	0.76	0.73
		RE(%)	S	24.66	7.17	3.83	56.94	7.61	17.85	24.66
			B	6.65	70.15	10.14	83.19	17.87	42.76	6.65
	CB4.1C	RMSE	S	2.40	9.44	1.75	1.98	0.16	0.19	2.40
			B	2.01	13.75	2.34	2.07	0.12	0.20	2.01
		CC	S	0.91	0.17	0.77	0.16	0.86	0.84	0.91
			B	0.69	0.32	0.78	0.05	0.59	0.65	0.69
		RE(%)	S	16.39	67.20	3.35	67.73	6.55	18.39	16.39
			B	5.07	75.08	12.66	66.21	34.22	54.19	5.07
	CB4.2C	RMSE	S	2.19	9.27	1.61	2.02	0.15	0.17	2.19
			B	1.92	9.47	2.01	1.55	0.12	0.17	1.92
		CC	S	0.94	0.08	0.84	0.11	0.85	0.83	0.94
			B	0.66	0.44	0.85	0.01	0.53	0.68	0.66
		RE(%)	S	14.87	96.34	5.01	72.51	3.31	15.77	14.87
			B	2.84	70.18	8.77	57.09	34.88	55.36	2.84
	CB4.3C	RMSE	S	2.22	9.24	1.68	1.96	0.15	0.17	2.22
			B	1.95	8.35	1.89	1.45	0.12	0.17	1.95
		CC	S	0.95	0.11	0.87	-0.17	0.86	0.83	0.95
			B	0.66	0.39	0.87	-0.07	0.51	0.72	0.66
		RE(%)	S	15.01	111.78	7.59	66.46	1.29	5.14	15.01
			B	2.39	65.96	5.33	53.97	39.03	55.24	2.39
	CB5.1	RMSE	S	1.84	7.58	1.41	1.82	0.12	0.13	1.84
			B	1.97	7.48	2.02	1.16	0.11	0.16	1.97
		CC	S	0.95	0.27	0.89	-0.21	0.86	0.86	0.95
			B	0.64	0.48	0.85	0.09	0.52	0.74	0.64
		RE(%)	S	11.01	78.94	3.45	60.62	1.13	12.43	11.01
			B	0.52	63.00	6.76	36.34	43.19	65.12	0.52
Mid-Lower Bay	CB5.2	RMSE	S	1.69	6.23	1.20	1.67	0.13	0.13	1.69
			B	1.86	8.69	1.69	1.05	0.10	0.14	1.86
		CC	S	0.95	0.29	0.91	-0.26	0.84	0.84	0.95
			B	0.68	0.41	0.89	0.11	0.51	0.74	0.68
		RE(%)	S	9.36	66.84	4.90	51.28	3.52	14.03	9.36
			B	1.46	63.64	3.70	29.82	60.94	61.07	1.46
	CB5.4	RMSE	S	1.71	7.85	1.50	1.06	0.14	0.14	1.71
			B	2.24	7.20	1.77	1.02	0.09	0.11	2.24
		CC	S	0.94	0.23	0.85	-0.15	0.74	0.76	0.94
			B	0.68	0.39	0.89	-0.02	0.48	0.75	0.68
		RE(%)	S	8.20	71.59	9.36	7.44	10.64	20.02	8.20
			B	5.03	54.07	17.76	15.40	61.79	48.40	5.03
	CB6.1	RMSE	S	1.54	12.45	1.28	1.15	0.10	0.11	1.54
			B	2.30	12.30	2.05	1.03	0.06	0.08	2.30
		CC	S	0.90	0.12	0.84	-0.19	0.80	0.79	0.90
			B	0.76	0.09	0.93	0.11	0.72	0.78	0.76
		RE(%)	S	2.79	16.09	5.61	0.85	13.95	38.07	2.79
			B	5.93	38.12	28.52	15.94	27.26	42.34	5.93
	CB7.3	RMSE	S	2.32	4.99	1.27	1.14	0.06	0.06	2.32
			B	1.51	5.03	1.73	0.84	0.02	0.03	1.51
		CC	S	0.83	0.04	0.80	-0.04	0.77	0.74	0.83
			B	0.57	-0.06	0.81	-0.17	0.44	0.41	0.57
		RE(%)	S	2.72	36.79	6.89	12.31	10.83	53.86	2.72

		B	1.10	8.02	14.63	5.05	42.56	57.15	1.10
WT5.1	RMSE	S	4.87	29.40	3.13	3.40	0.81	1.04	4.87
		B	9.57	13.80	4.44	3.92	0.85	0.85	9.57
	CC	S	0.74	0.29	0.47	-0.05	0.67	0.68	0.74
		B	0.59	0.17	0.85	-0.22	0.38	0.25	0.59
	RE(%)	S	53.34	44.13	11.90	94.04	130.97	166.46	53.34
		B	66.71	224.36	116.08	136.41	270.30	101.04	66.71
LE2.3	RMSE	S	2.06	8.27	1.26	1.39	0.16	0.18	2.06
		B	2.79	7.31	1.67	1.48	0.14	0.16	2.79
	CC	S	0.92	0.17	0.89	-0.04	0.80	0.80	0.92
		B	0.75	0.33	0.95	-0.16	0.67	0.77	0.75
	RE(%)	S	11.53	49.04	7.11	36.49	17.56	40.77	11.53
		B	11.97	16.01	19.21	44.34	48.96	57.30	11.97
LE3.4	RMSE	S	2.43	9.22	1.36	0.91	0.08	0.10	2.43
		B	3.25	NaN	1.88	1.25	0.09	0.12	3.25
	CC	S	0.93	-0.03	0.86	-0.01	0.45	0.40	0.93
		B	0.83	NaN	0.89	-0.35	0.53	1.00	0.83
	RE(%)	S	13.16	36.51	6.45	16.79	25.82	19.25	13.16
		B	16.84	NaN	10.40	23.77	24.89	793.57	16.84

Figures for Chapter 2

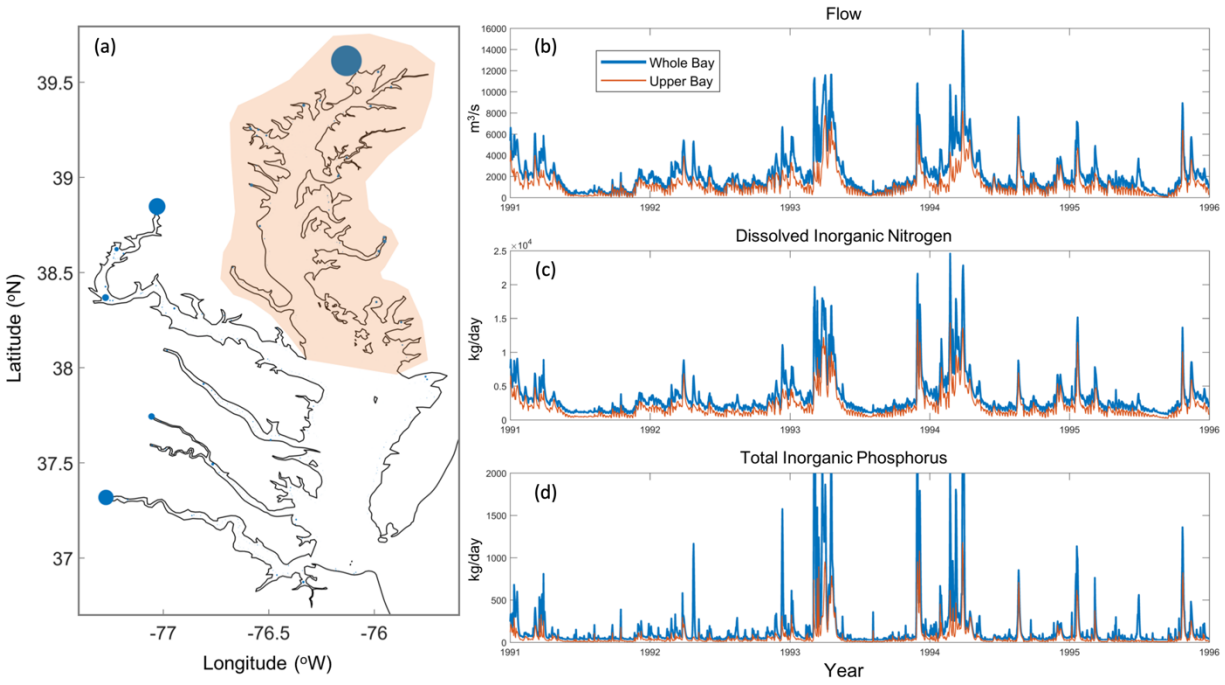

Fig. 2-1: (a) Distribution of averaged annual water loading into the Chesapeake Bay in blue spots proportional to the magnitude. (b-d) Time series of total loading of flow, dissolved inorganic nitrogen and total inorganic phosphorus from the whole Bay and upper Bay (marked in orange in panel (a)).

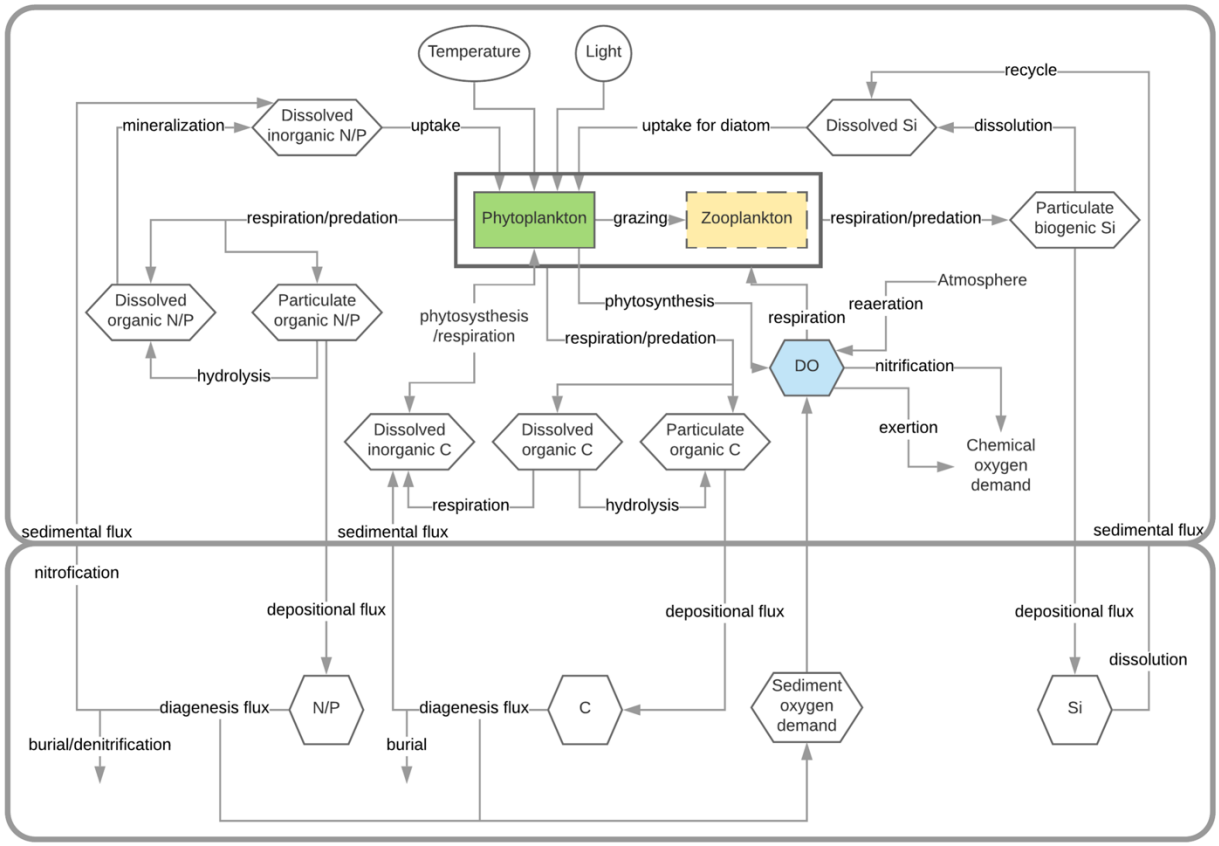

Fig. 2-2: ICM eutrophication model schematic (Cerco, 2000)

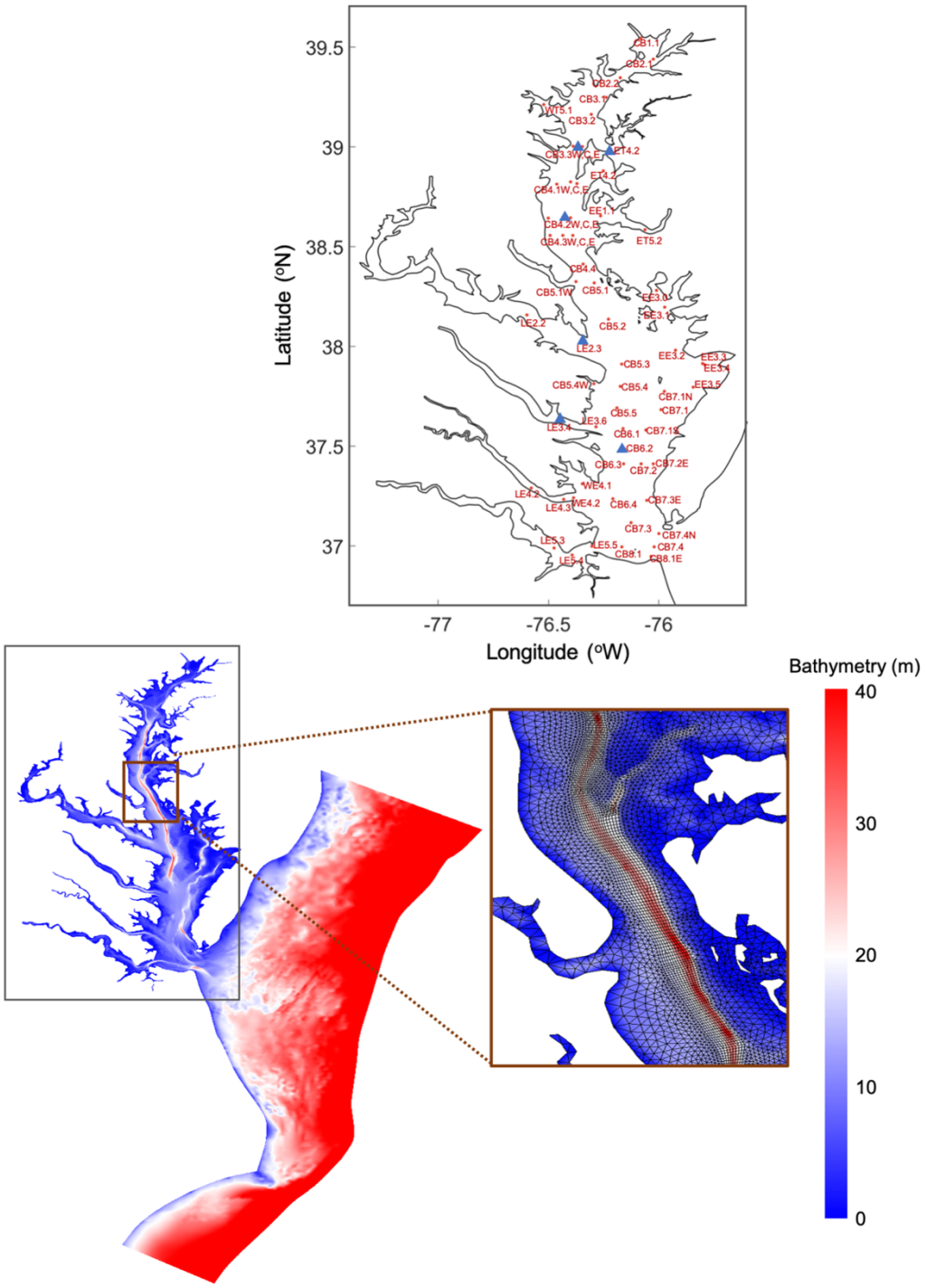

Fig. 2-3: Model Grid and major CBP stations used in this paper, where highlighted blue triangles represent the stations shown in Fig. 2-5.

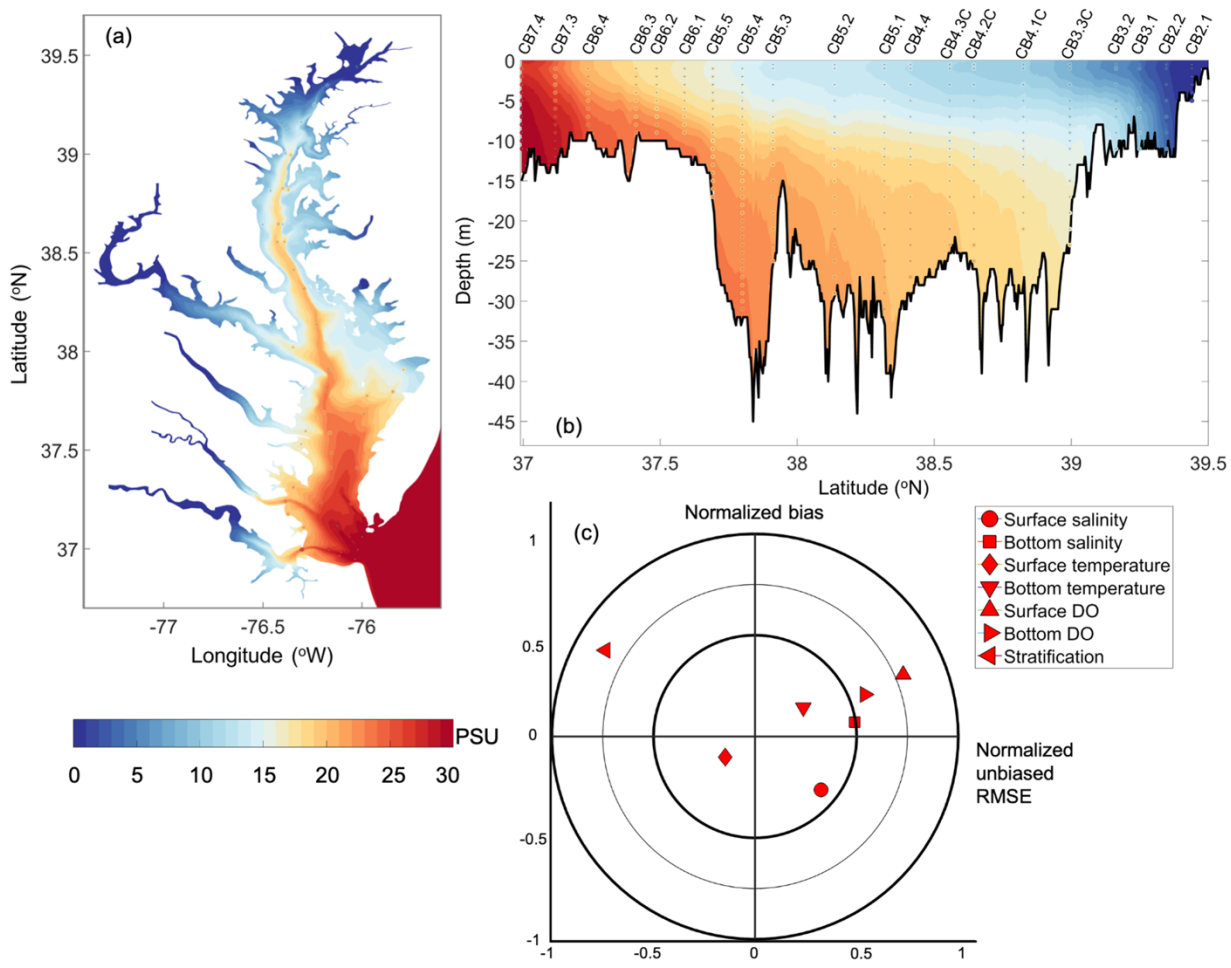

Fig. 2-4: Five-year averages of salinity (a) over the Bay bottom and (b) along the main stem. The colored contours represent model results; the colored circles with grey '+' represent Chesapeake Bay Program observations. (c) Target diagram for salinity, temperature, DO, and stratification model skill at all main stem stations (but stations with fewer than 60 3D measurement points are excluded).

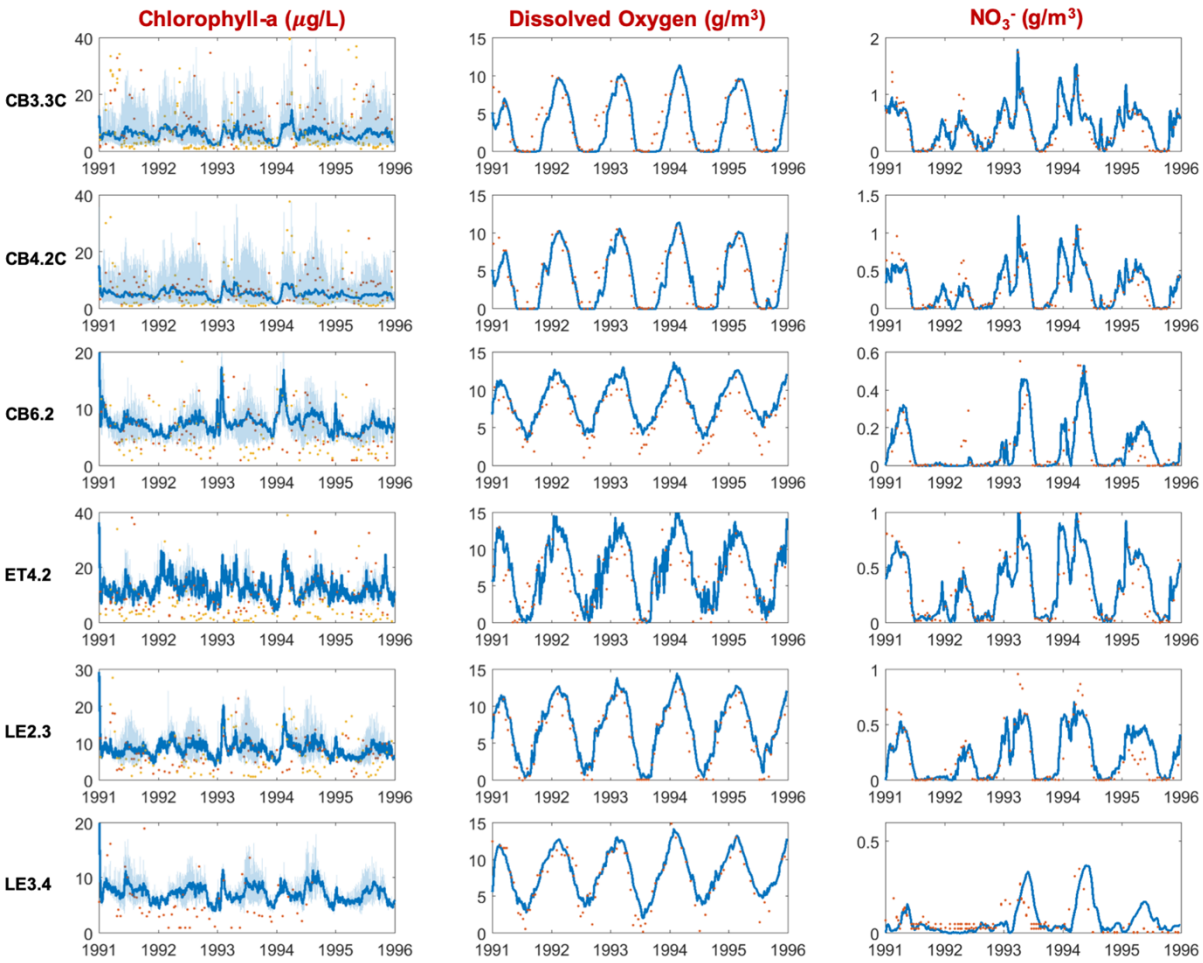

Fig. 2-5: Time series of observed and modeled depth-averaged chlorophyll-a, bottom DO and surface nitrate at main stem station CB3.3C (Upper-mid Bay), CB4.2C (Mid Bay), CB6.2 (Lower Bay), and tributary stations ET4.2 (Chester R.), LE2.3 (Potomac R.) and LE3.4 (Rappahannock R.). In the chlorophyll-a plots, red spots represent surface observation, yellow ones represent bottom. Blue lines represent modeled concentrations, where dark ones represent depth-averaged values and light blue ones represent both surface and bottom concentrations. For other plots, red spots represent observed and blue lines represent modeled DO and nitrate.

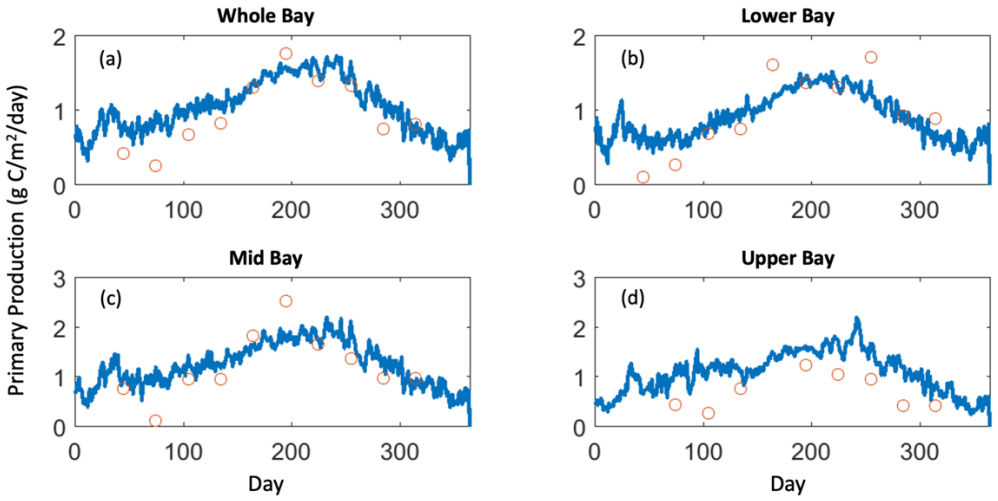

Fig. 2-6: Comparison of daily results from the five-year averaged modeled phytoplankton production with seventeen-year averaged observations (Harding et al., 2002) for (a) whole Bay, (b) lower Bay, (c) mid Bay and (d) upper Bay. Blue lines represent model results and red circles represent observations.

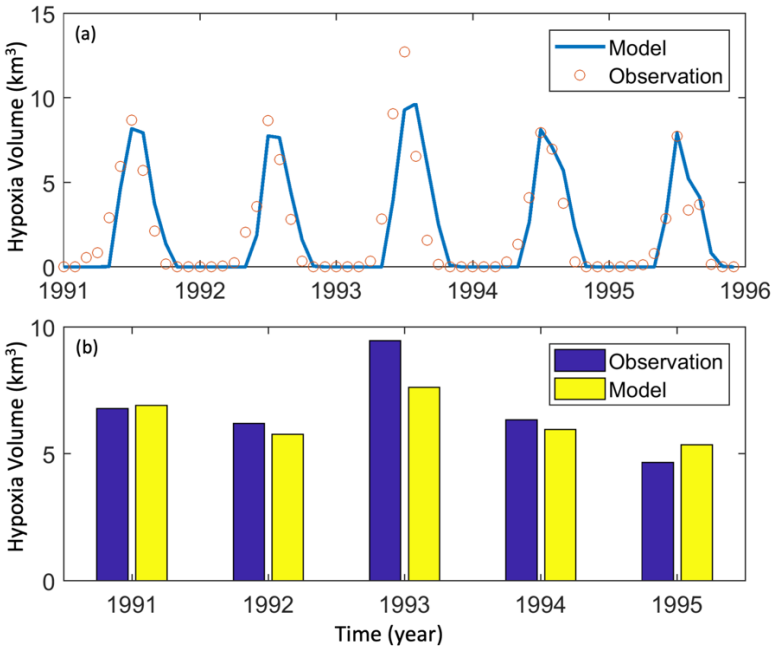

Fig. 2-7: Comparison of (a) interpolated monthly-averaged hypoxic volume from 1991 to 1995; (b) averaged hypoxic volume from June to August during each year of 1991-1995.

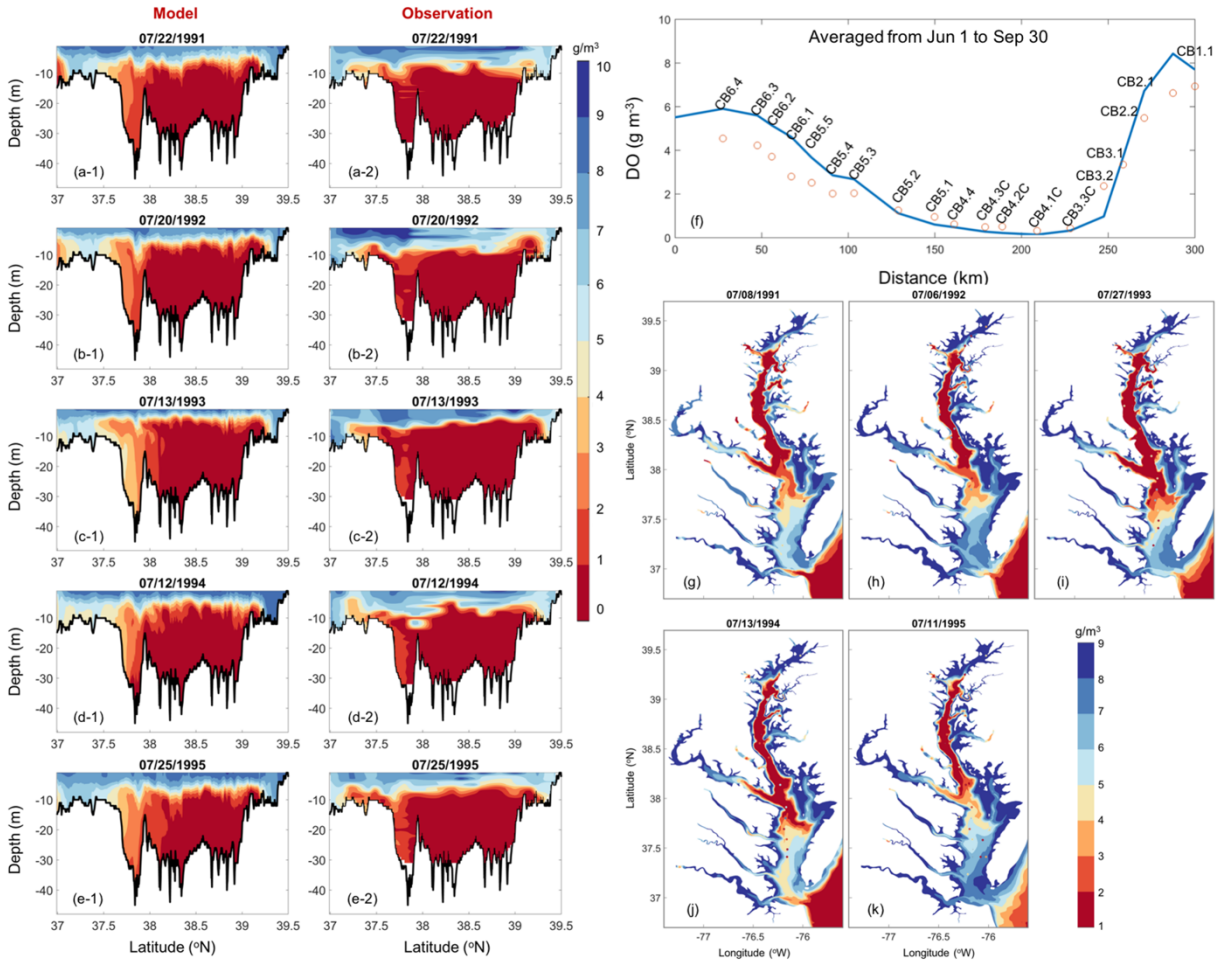

Fig. 2-8: Snapshot comparison of modeled and observed DO vertical profile along main channel on (a-1,2) July 22, 1991, (b-1,2) July 20, 1992, (c-1,2) July 13, 1993, (d-1,2) July 12, 1994 and (e-1,2) July 25, 1995 over a 5-day window time. (f) Five-year averaged bottom DO from Jun to Sep along main channel stations. Blue line represents model results and red circles represent Chesapeake Bay Program observations. Comparison of modeled and observed bottom DO on (g) July 8, 1991, (h) July 6, 1992, (i) July 27, 1993, (j) July 13, 1994 and (k) July 11, 1995 over a 4-day window. The colored contours represent model results; the circles with grey '+' represent Chesapeake Bay Program observations on that day.

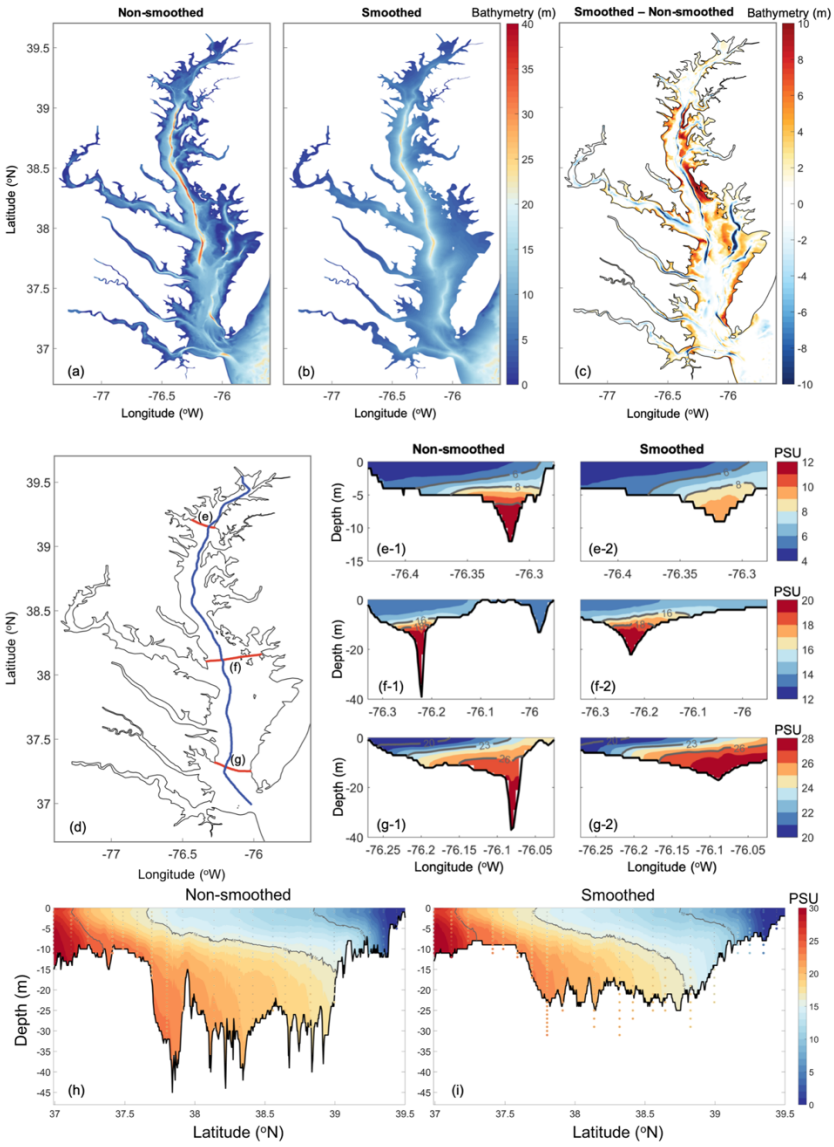

Fig. 2-9: (a,b,c) Non-smoothed and smoothed bathymetry and their difference. (d). Locations of three cross-channel transects for (e,f,g) and one along-channel transect for (h,i) respectively. (e,f,g-1,2): Five-year averages of salinity over cross-channel transects located closed to CB3.2, CB5.2 and CB6.4 for the case of non-smoothed and smoothed bathymetry. (h,i): comparison for the along-channel transects; the colored contours represent model results; the circles with grey '+' represent Chesapeake Bay Program observations. Due to bathymetry alteration the observed profiles are partially outside the model bottom in (i).

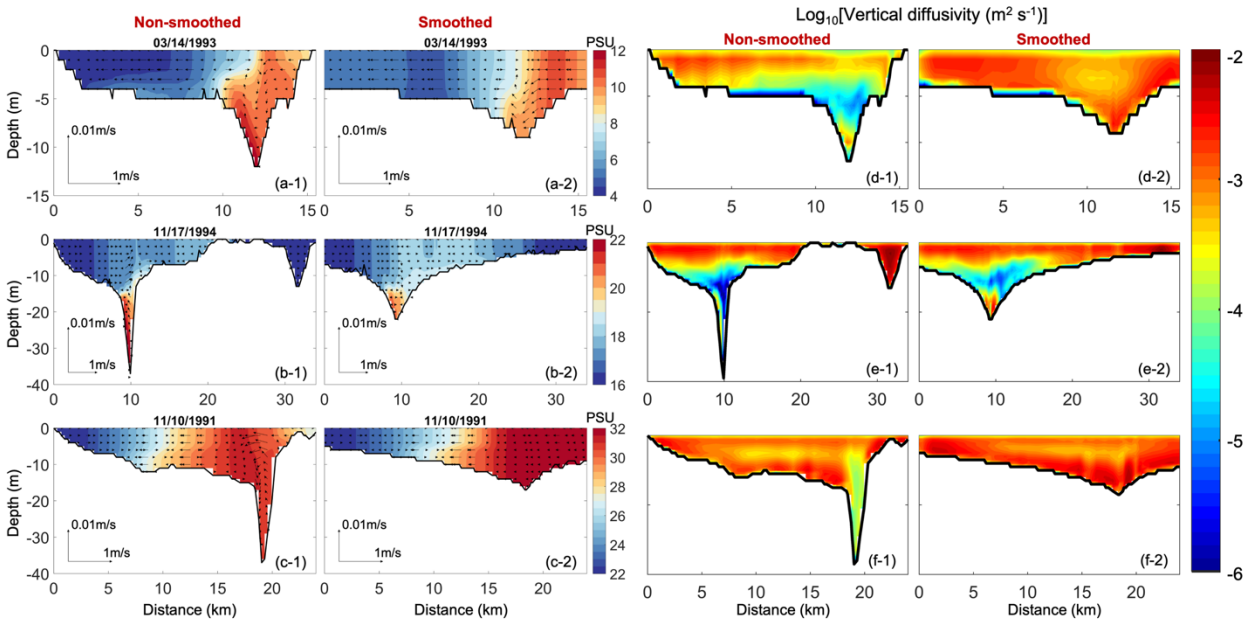

Fig. 2-10: Screenshots of lateral circulation over cross-channel transects located closed to (a) CB3.2, (b) CB5.2 and (c) CB6.4 (transect shown in Fig. 2-9) for the case of non-smoothed and smoothed bathymetry. The colored contours represent modeled salinity. The black arrows represent the flow direction along this transect with length proportional to the velocity magnitude. (d,e,f) 5-year-averages of vertical diffusivity in colored contours over cross-channel transects corresponded to (a,b,c) for the case of non-smoothed and smoothed bathymetry.

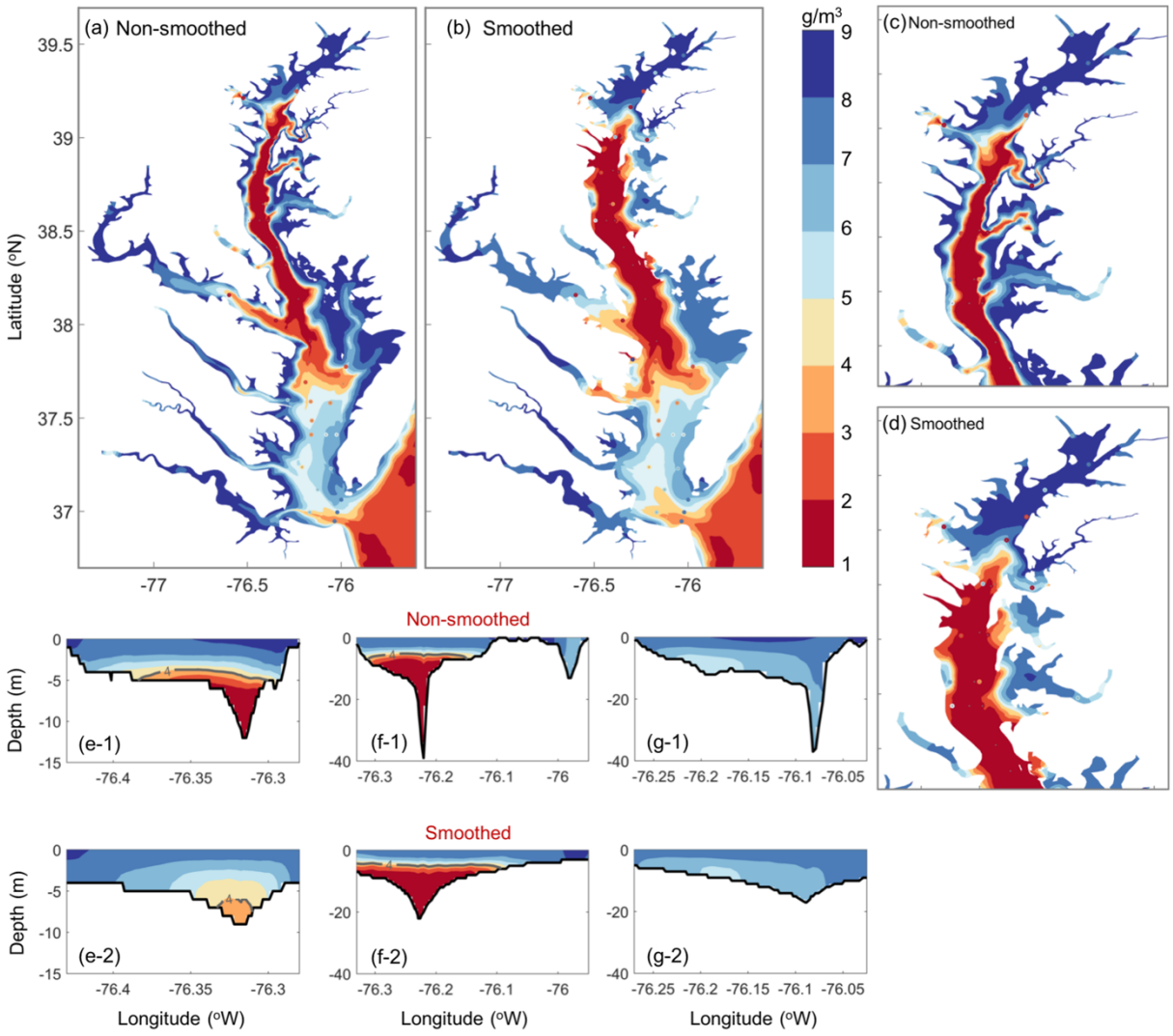

Fig. 2-11: (a-b) Averaged bottom oxygen concentration on July 11, 1994 over a 4-day window for the case of non-smoothed and smoothed bathymetry. (c-d). Zoomed in to the Bay mouth for (a-b). The colored circles with grey '+' represent Chesapeake Bay Program observations in (a-d). (e,f,g-1,2): Five-year averages of oxygen concentration in July over cross-channel transects located closed to CB3.2, CB5.2 and CB6.4 (transects shown in Fig. 2-9) for the cases of non-smoothed and smoothed bathymetry respectively.

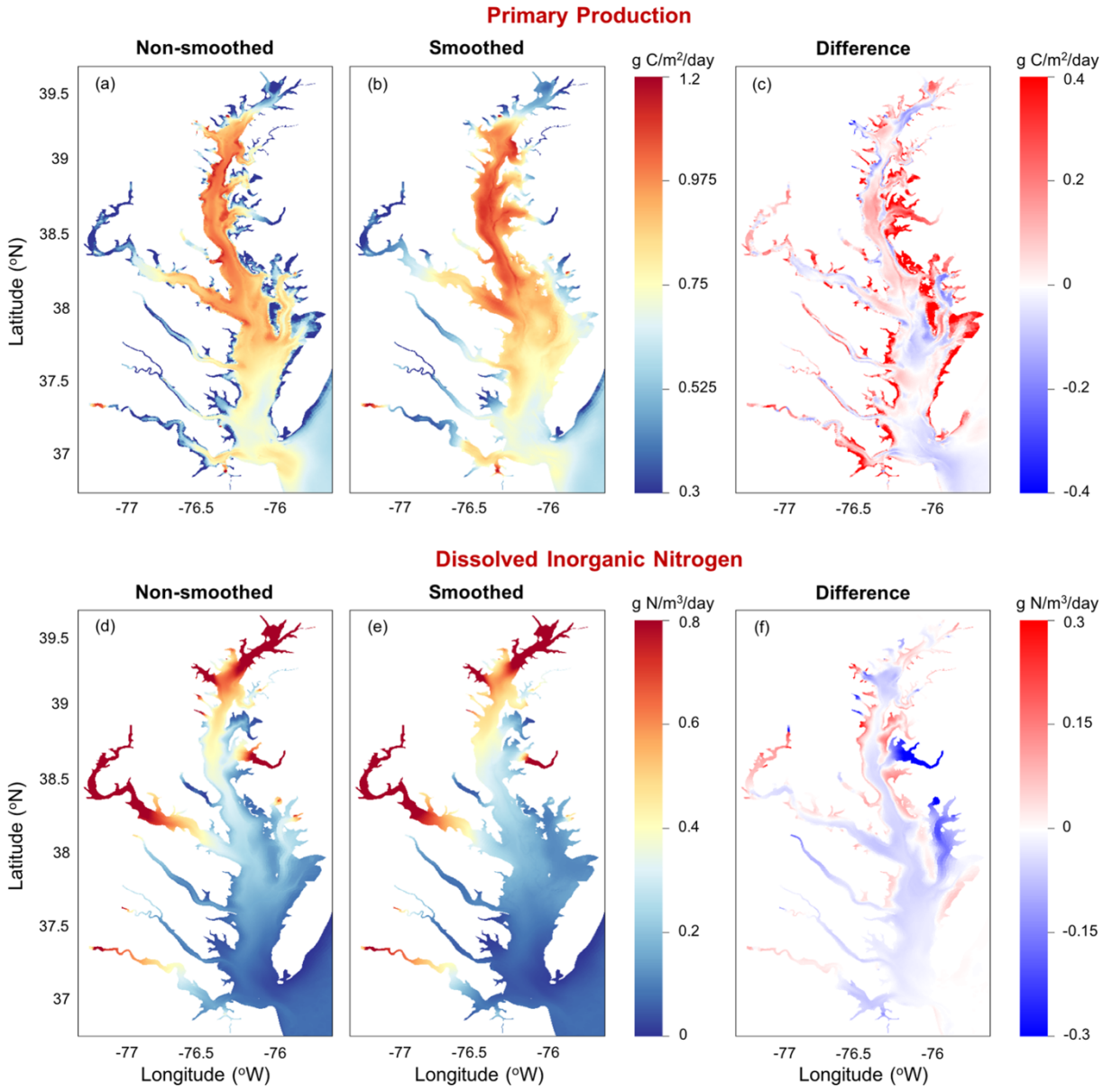

Fig. 2-12: (a,b) Five-year averages of phytoplankton production for the case of non-smoothed and smoothed bathymetry; (c) difference of phytoplankton production; (d,e) DIN concentration for the case of non-smoothed and smoothed bathymetry; (f) difference of DIN concentration. (difference = smoothed minus non-smoothed)

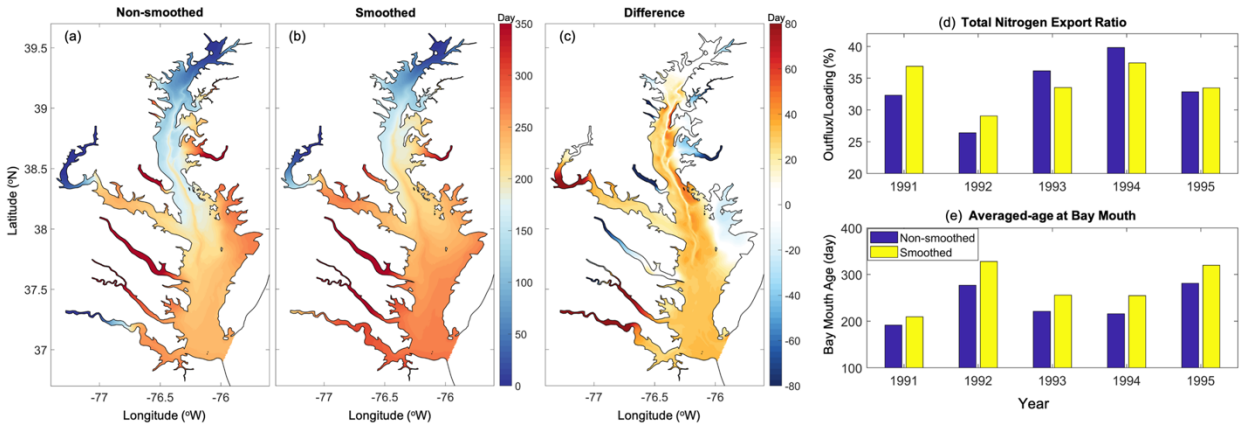

Fig. 2-13: (a,b) Five-year averages of freshwater age from Susquehanna River (depth-averaged) for the case of non-smoothed and smoothed bathymetry. (c) Five-year averaged difference of depth-averaged freshwater age between these two cases (smoothed minus non-smoothed). (d) Total nitrogen export ratio (outflux divided by loading) of each year. (e) Bay-mouth depth-averaged water age of each year for the case of non-smoothed and smoothed bathymetry. Blue bar represents non-smoothed case and yellow bar represents smoothed case.

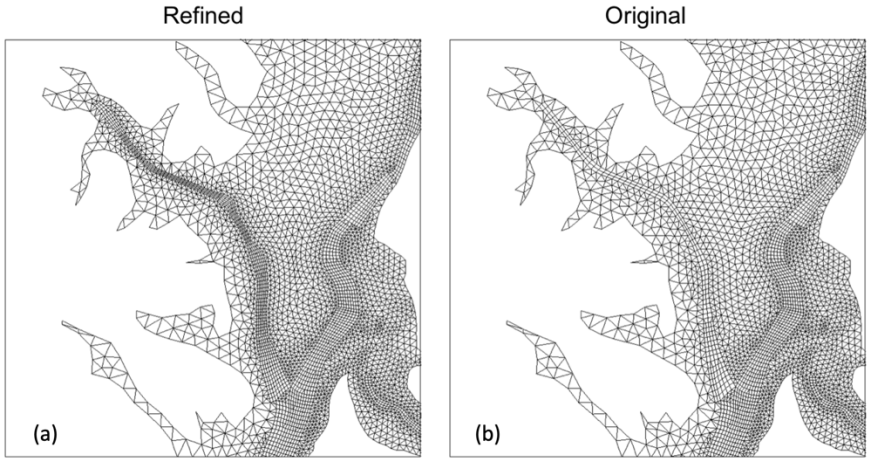

Fig. 2-14: Unstructured (a) refined and (b) original mesh from main channel into Baltimore Harbor.

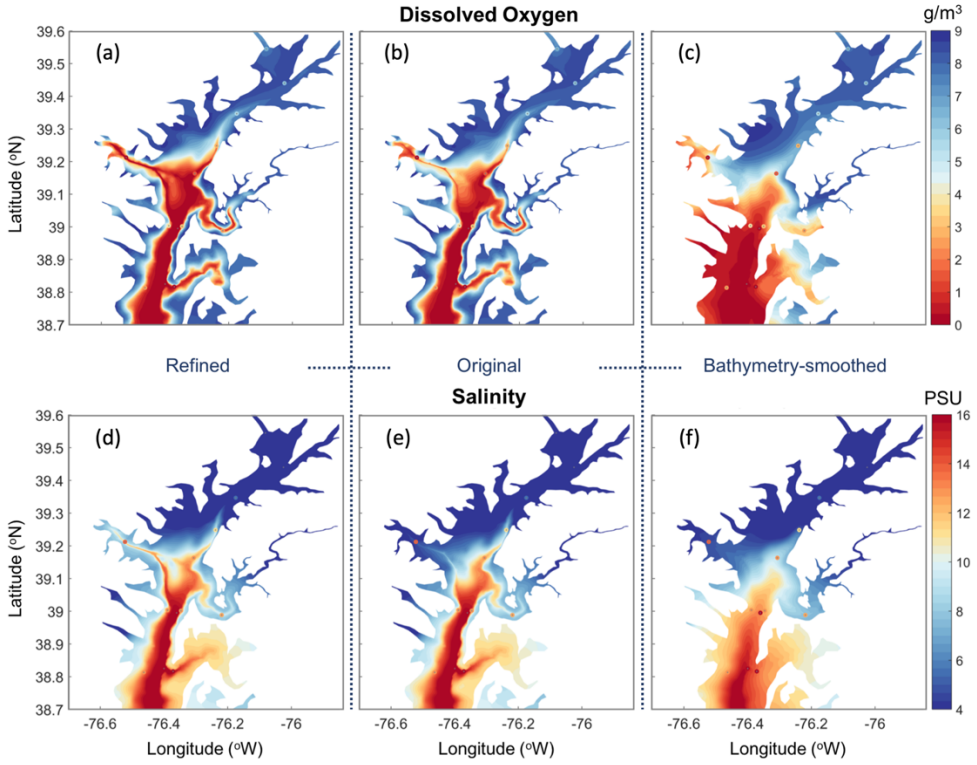

Fig. 2-15: Five-year averages of bottom oxygen concentration and salinity over Baltimore Harbor in July for the case of (a, d) refined grid (without bathymetry smoothing), original grid with (b, e) non-smoothed and (c, f) smoothed bathymetry respectively. The colored contours represent model results; the circles with grey '+' represent Chesapeake Bay Program observations.

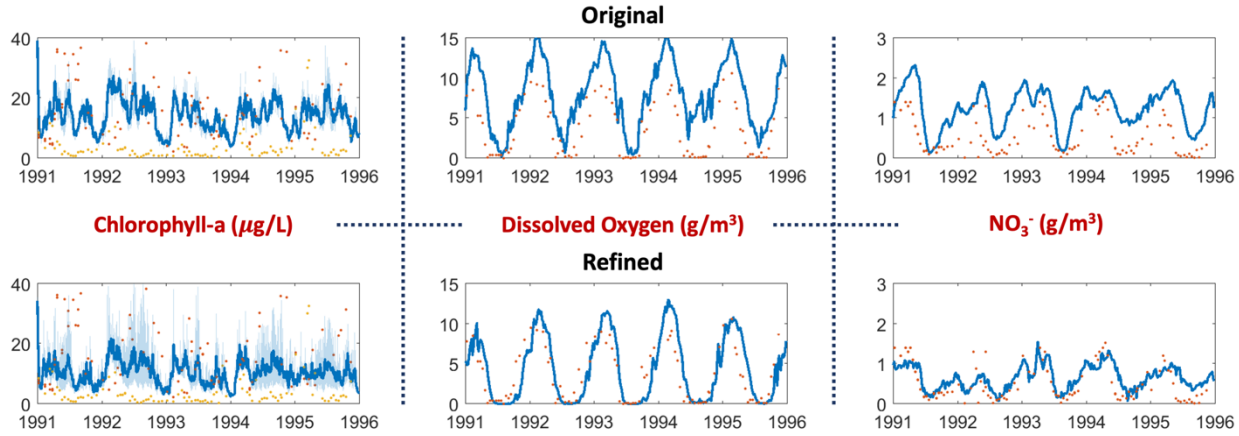

Fig. 2-16: Comparison of depth-averaged (dark blue line), bottom and surface (light blue lines) chlorophyll-a, bottom DO and surface nitrite at WT5.1 (cf. Fig. 2-3). Dots represent Chesapeake Bay Program observations. Red dots in plots of chlorophyll-a represent surface and yellow ones represent bottom.

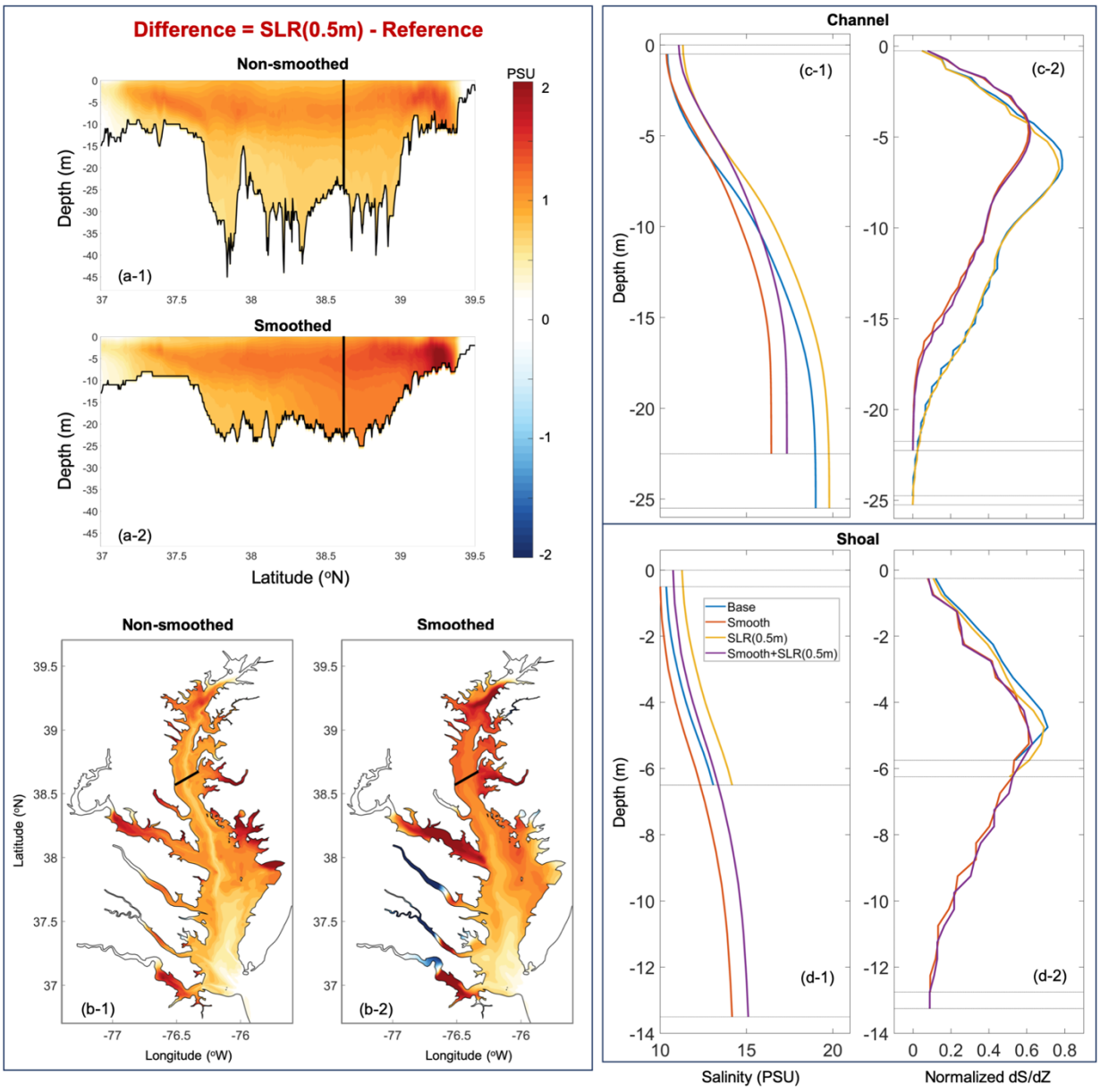

Fig. 2-17: Five-year averages of (a) along-channel salinity difference and (b) bottom salinity difference caused by SLR for non-smoothed and smoothed cases. Salinity profile and normalized ds/dz for (c) channel and (d) shoal marked black in (a,b).

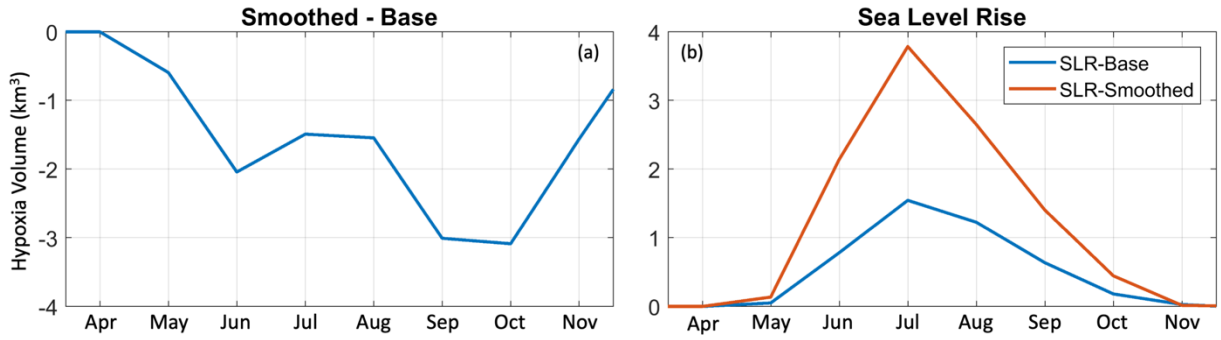

Fig. 2-18: (a) Difference of simulated hypoxic volume as the result of bathymetry smoothing. (b) Change of hypoxia volume caused by SLR (0.5m) for non-smoothed and smoothed cases.

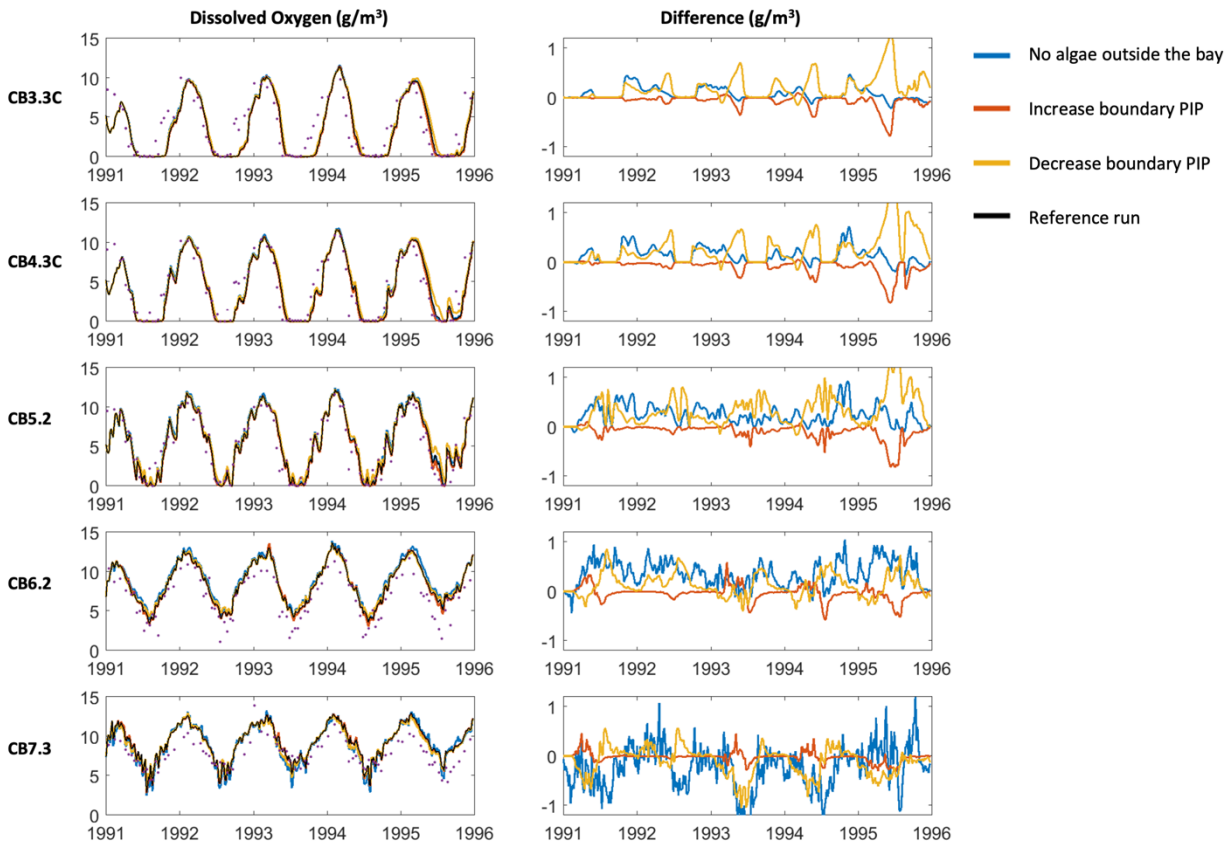

Fig. 2-19: Time series of DO concertation and the difference to the reference run (test - reference) in typical stations along the main stem over different regions. Purple dots represent Chesapeake Bay Program observations.

Chapter 3

3. Impacts of sea-level rise on hypoxia and phytoplankton production in Chesapeake Bay: model prediction and assessment

Published in *JAWRA Journal of the American Water Resources Association*

April 2021

doi: 10.1111/1752-1688.12921

Abstract

In this study, the influence of sea-level rise (SLR) on seasonal hypoxia and phytoplankton production in Chesapeake Bay is investigated using a 3D unstructured grid model. Three SLR scenarios (0.17 m, 0.5 m, and 1.0 m) were conducted for 1991 to 1995. Results show that the summer hypoxic volume (HV) increases about 2%, 8%, and 16%, respectively for these three scenarios compared with Base Scenario. The contributions of physical and biological processes on the increase in the HV were analyzed. With the projected SLR, enhanced gravitational circulation transports more oxygen-rich water in the bottom layer from the mouth. However, the pycnocline moves upwards along with increasing water depth, which largely prolongs the time for dissolved oxygen (DO) to be transported to the bottom. The altered physical processes contribute greatly to a larger HV bay-wide. Besides, SLR increases the whole Bay phytoplankton production, with a larger increase in shallow areas (e.g. 53% in areas with depth less than 1 m under SLR of 0.5 m). Enhanced light availability is suggested to be the major driver of blooming phytoplankton under SLR in shallow areas. While increased DO production over the euphotic zone is mostly released to the atmosphere and transported downstream, the increase in settled organic matter greatly promotes DO consumption in the water column. The increased respiration is another major cause of the HV increase besides the physical contributions.

3.1 Introduction

Hypoxia (dissolved oxygen (DO) concentration <= 2 mg L^{-1}), occurs in deeper regions of Chesapeake Bay (the Bay hereafter) in the summertime and has been recorded since the last century (Seliger et al., 1985; Hagy et al., 2004). The hypoxic volume (HV) in Chesapeake Bay ranges from 8 to 17 km^3, with larger HV observed in wet years (Bever et al., 2013; Hagy et al., 2004). The observed large HV decreases habitats for fish, invertebrates, and benthic macrofauna and therefore degrades the ecosystem by changing the food web and energy transfer between different trophic levels (Diaz and Rosenberg, 1996; Vaquer-Sunyer and Duarte, 2008). Besides, hypoxia changes nutrient cycling by inducing bottom nutrient release that further affects the ecosystem (Kemp et al., 1990)

The primary cause of hypoxia in the Bay is that DO consumption exceeds replenishment from the surface waters through the pycnocline. Net planktonic respiration, heterotrophic respiration, and benthic consumption of deposited organic matter are major components of the bottom water DO consumption (Kemp et al., 1992). The DO replenishment from the atmosphere decreases when the vertical stratification is strengthened and the solubility is reduced in warmer water in summer (Taft et al., 1980). For example, an increase in freshwater discharge from the Susquehanna River, which also brings excess nutrients, leads to a stronger stratification and therefore severe hypoxia (Seliger et al., 1985; Taft et al., 1980). Excessive anthropogenic loads of nutrients are recognized to be a major cause of eutrophication. The onset of hypoxia in the Bay usually starts after the spring algal bloom and the subsequent respiration of settled and enhanced accumulation of organic matter in the water column and bottom sediment (Newcombe and Horne, 1938; Murphy et al., 2011). After the initiation of hypoxia, increased nutrient flux

from the sediment supports the summer algal bloom which further increases the bottom water column DO consumption (Kemp et al., 1992; Murphy et al., 2011).

Worldwide sea-level rise (SLR) has been accelerating over recent years from about 1.7 mm yr^{-1} between 1901 to 2010 to about 3.2 mm yr^{-1} between 1993 to 2010 (IPCC, 2014). In Chesapeake Bay, the estimated trend of relative SLR, varying from 2.7 to 4.6 mm yr^{-1} for different locations over 1955 to 2007, is larger than the estimation for global mean SLR (Boon et al., 2010; Zervas, 2001). SLR is projected to be 0.3 - 0.7 m by 2050 and 0.7 - 1.6 m by 2100 (Rahmstorf, 2007; Najjar et al., 2010; Boesch et al., 2013). Under SLR, the bay-averaged salinity is predicted to increase by 0.5 with an SLR of 0.2 m (Hilton et al. 2008). The bay-averaged stratification is estimated to be strengthened under SLR, which reduces vertical exchange through the pycnocline and tends to diminish the bottom DO supply from the surface layer (Hong and Shen, 2012). Additionally, the residence time for substances discharged from the Susquehanna River is prolonged due to larger water volume under SLR (Hong and Shen, 2012). The changes in hydrodynamics could affect DO dynamics and hypoxic volume (HV).

Multiple numerical studies have been conducted to discuss the change in the hypoxic/anoxia volume in response to SLR in the Bay. However, diverse changes have been predicted. Both Wang et al. (2017) and Irby et al. (2018) showed an improvement in the DO conditions whereas Ni et al. (2017) suggested an increase in the summer HV. St-Laurent et al. (2019) made an explicit comparison between different models and showed that all the models predict the same trend of change in DO but disagree on the changes in HV. This suggests large uncertainties still exist in numerical modeling of the effects of SLR on hypoxia. The uncertainties may be largely due to the differences in model kinetic parameters and grid resolution. Another concern is the lack of a high-resolution grid that cannot well represent

shallow waters and tributaries in many of these models (Cai et al., 2020). There has been no report on what and how much change will happen in shallow regions under SLR, though tributaries and shallow water areas (water depths smaller than 2 m in this study) are expected to experience larger changes compared with the main stem of the Bay.

In this study, a high-resolution three-dimensional unstructured-grid (UG) model is used to investigate the effects of SLR on hypoxia. Besides studying the effects of SLR on the main stem, we also explore the changes in HV, flushing time, and phytoplankton production, with a focus on the tributaries and shallow water areas. This paper is organized as follows: a description of the model, scenarios, and analysis methods are presented in Section 3.2. Results of changes in hypoxic conditions and phytoplankton production are presented in Section 3.3. Section 3.4 presents the discussions on the drivers of the changes for hypoxia including inside the tributaries and shallow water areas. Section 3.5 summarizes the entire study.

3.2 Methods

3.2.1 SCHISM-ICM

We use a fully coupled hydrodynamic and water quality model, SCHISM-ICM, which couples the Semi-implicit Cross-scale Hydroscience Integrated System Model with the Integrated Compartment Model (ICM) for water quality simulation (Cerco and Cole, 1994; Zhang et al., 2016; Cai et al., 2020; schism.wiki). In addition, the sediment flux model which simulates the diagenesis and recycling process is incorporated into ICM (DiToro and Fitzpatrick, 1993). SCHISM-ICM solves physical and biogeochemical processes simultaneously. There are 21 water quality state variables simulated by ICM: algal assemblage group, comprised of diatom, green algae, and cyanobacteria, along with three groups of carbon, five groups of nitrogen, four

groups of phosphorus, chemical oxygen demand and DO. Local kinetic processes of these state variables are simulated by ICM, while evolution and spatial distribution of these state variables are simulated by SCHISM.

SCHISM uses a semi-implicit time-stepping scheme applied in a hybrid finite-element and finite-volume framework to solve Navier-Stokes equations and uses an Eulerian-Lagrangian method to treat the momentum advection. This numerical scheme ensures the time step is not restricted by the CFL (Courant-Friedrichs-Lewy) condition. For shallow water areas where high-resolution model grids are used, the time step can remain large in the hydrodynamic model. This largely improves numerical efficiency. In the vertical dimension, the model uses a highly flexible and efficient hybrid coordinate system LSC^2 (localized Sigma Coordinate with Shaved Cell), which allows a varying number of vertical grids at each node (Zhang et al. 2015). The high-resolution model grids, coupled with the hybrid vertical coordinate system for shallow water areas allow for seamless spatial cross-scale simulations. This makes it feasible to study the effects of SLR on shallow and deep areas as a whole.

3.2.2 Design of scenarios

The model domain for Chesapeake Bay and its tributaries is shown in Fig. 3-1. Base Scenario uses the current mean sea level as a reference datum for model simulations, and the model has been developed and calibrated by Cai et al. (2020). The simulation period is from 1991 to 1995, which is currently used as a reference period for management scenario simulations by the Chesapeake Bay Program (CBP). Besides the Bay proper, the grid extends farther offshore to the shelf break to minimize the influence of open ocean conditions on the interior of the Bay. The grid resolution varies from 2.4 km on the continental shelf to less than 100 m in

tributaries. A flexible vertical grid system LSC2 (Localized Sigma Coordinates with Shaved Cells) developed by Zhang et al. (2015) was applied in this study, which preserves the spatial variation of bathymetry in high fidelity. The number of vertical layers varies from 11 to 52 (33 on average) for the whole system with resolution varying from 0.5 to 19 m. The model uses a single non-split time step of 150 sec.

Interpolated elevations from two tidal gauges at Lewes, DE, and Beaufort, NC were used to force elevations at the ocean boundary. We obtained the boundary temperature from Simple Ocean Data Assimilation (SODA, Carton and Giese, 2008) from 01/01/1991 to 10/06/1992 (when HYCOM is not available) and hybrid coordinate ocean model (HYCOM, Chassignet et al., 2007) from 10/07/1992 to 12/31/1995. World Ocean Atlas monthly climatological data provided the ocean boundary salinity. We used constant values for the nutrients and other water quality variables in the ocean boundary because the ocean boundary is far away from the Bay mouth and the model simulation in the Bay was tested to be generally insensitive to the nutrient conditions at the ocean boundary (Cai et al., 2020). Phase 6 Watershed Model of Chesapeake Bay Assessment Tool (CAST) provided daily runoff and nutrient loads from the watershed for this study (Shenk and Linker, 2013). The daily loadings are linearly interpolated into each time step in this model. The atmospheric forcing and heat fluxes were obtained from the North American Regional Reanalysis (Mesinger et al., 2006).

SLR of 0.17 m, 0.5 m, and 1.0 m were added to the sea surface height at the ocean boundary of the Base Scenario, respectively for each SLR scenario. All scenarios share identical oceanic, watershed, and atmospheric forcings. In this study, since we focus on the effects of SLR as the sole driver to cause changes in transport and biochemical processes, all other processes, such as river discharge, wind, solar radiation, and nutrient loadings remain unchanged.

According to estimations from Dettmann (2001), the surface area of the Bay is 11,524 × 10^6 m^2 and the mean depth of it is 6.8 m. SLR of 0.5 m will increase the Bay volume (ΔVol) by 5.764 km^3 (7.4%) without considering the changes in the surface area. The average volume or depth increase is 7.4% of the original total volume and depth. For this study, the increase in the surface area in the low-lying area of the Bay due to SLR was not considered for comparing the model results with other published model results.

3.2.3 Analysis methods

3.2.3.1 Flushing time

Flushing time is the time it takes to replace the water mass of a waterbody and is often estimated by the ratio of the mass of a scalar in a reservoir to the rate of renewal of the scalar (Monsen et al., 2002). We calculated the flushing time for the major tributaries because the river discharge is estimated to be dominant for the water exchange in the Chesapeake Bay (Xiong et al., 2021). Flushing time can be estimated numerically by calculating the e-folding time. To calculate the e-folding time, passive tracers were released in each tributary twice a month. The e-folding time for each release was calculated as the time it takes for tracer concentration decreases to e^{-1} (about 37%) of the initial tracer concentration, and the values were then averaged for the year 1992 (Monsen et al., 2002).

3.2.3.2 Hypoxic volume

The hypoxic volume estimation follows the method in Bever et al (2013) for estimating the HV based on observations. Using the same method helps avoid any bias introduced by the estimation method when comparing the modeled HV with observations. The modeled DO

profiles at major CBP stations (as used by Bever et al. 2013) were interpolated/extrapolated onto the current SCHISM UG grid to cover the entire Chesapeake Bay before the total HV was calculated. A linear interpolation was used at each vertical layer, and the hypoxic layer thickness at each node was then calculated. The hypoxic layer thickness at each element is the averaged value among its three/four surrounding nodes. The total HV is the sum of HV in each element, which is the product of the element area and its hypoxic layer thickness.

3.2.3.3 Phytoplankton production

Local phytoplankton production was computed by integrating local phytoplankton production in each water column for the element:

$$\mathrm{GPP} = \sum_{i=1}^{n} (\mathrm{C1}_i \cdot \mathrm{G1}_i + \mathrm{C2}_i \cdot \mathrm{G2}_i + \mathrm{C3}_i \cdot \mathrm{G3}_i) \cdot \mathrm{dep}_i \quad (3\text{-}1)$$

where GPP is areal gross primary production of phytoplankton (g C m^{-2} day^{-1}), n is the number of layers in each element, i is the vertical layer index, $\mathrm{C1}, \mathrm{C2}, \mathrm{C3}$ are carbon-based phytoplankton biomass of three groups (diatoms, green algae, and cyanobacteria) over each layer respectively (g C m^{-3}), $\mathrm{G1}, \mathrm{G2}, \mathrm{G3}$ are growth rates of the three phytoplankton groups (day^{-1}), and dep is layer thickness (m).

3.2.3.4 Comparison of DO concentration and local change rates

DO concentration and its local change rate were calculated based on the absolute altitude in each vertical layer of the model for both Base and SLR Scenarios. To better compare the vertical profiles of these values between Base and SLR Scenarios, two references in the vertical coordinate were used. The first reference was set to be the bottom, and its vertical position is unchanged in the model. This reference helps to estimate the changes in DO in the bottom

hypoxic layer. The second reference was set to be the free water surface, which rises in each SLR Scenario. This reference helps to compare the contributions of local biological processes in the upper layer, such as phytoplankton growth.

3.2.3.5 Oxygen and nutrient fluxes

Oxygen and nutrient fluxes were calculated at twelve cross-sections from the Bay mouth to the head (Fig. 3-1). Influx and outflux were calculated as the sectionally-integrated products of along-channel flow velocity and concentration of DO or nutrient where the velocity direction is upstream into the Bay (marked as negative) and downstream (positive), respectively. The calculations of fluxes through each cross-section follows:

$$\begin{cases} \text{influx} = \int_{A(u<0)} (u \cdot \text{Var}) dA \\ \text{outflux} = \int_{A(u>0)} (u \cdot \text{Var}) dA \end{cases} \tag{3-2}$$

where u is the along-channel velocity (m s^{-1}), Var is DO or nutrient concentrations (g m^{-3}), A is the area of cross-sections (m^2). Five-year averages of monthly and annually influx, outflux, and net flux at each cross-section were then calculated.

3.3 Results

3.3.1 Dissolved oxygen under SLR

Changes in DO concentrations due to SLR (ΔDO; Δ = SLR Scenario – Base Scenario, thereafter) can be either positive or negative, where positive values of ΔDO mean increases in DO concentration after SLR and negative values mean decreases. For different SLR scenarios, ΔDO has different magnitudes but shows a similar distribution in general. The magnitude of

ΔDO tends to increase linearly with the magnitude of SLR. The bottom ΔDO varies spatially, and it is mostly negative in shallow areas but becomes positive in some hypoxic areas (DO concentration is lower than 2 g m^{-3}) (Fig. 3-2). From June to August, the bottom ΔDO approaches zero in the upper and mid-Bay (between latitude 38.5 ^{o}N and 39 ^{o}N). A positive ΔDO of 0.1 to 0.2 g m^{-3} can be seen in the region near 38 ^{o}N when SLR exceeds 0.17 m.

3.3.2 The hypoxia volume under SLR

HV generally increases (ΔHV > 0) with some interannual variations (Fig. 3-3). Take the case of SLR = 0.5 m as an example, ΔHV ranges from 0.5 to 1.0 km^3 for different years. The increase of HV is positively correlated to the magnitude of SLR. ΔHV is, on average, about 2%, 8%, and 16% of the current HV in the Base Scenario, respectively, for the scenarios of SLR of 0.17 m, 0.5 m, and 1.0 m. In addition, although each case of SLR leads to a change in total water volume (ΔVol), ΔHV maintains a relatively stable fraction (10% - 15%) of ΔVol.

As mentioned in the introduction, there are diverse predictions for ΔHV (Wang et al., 2018; Ni et al., 2017; Irby et al., 2018). Our predicted ΔHV has the same trend as Ni et al. (2017). St-Laurent et al. (2019) conducted a comparison between all the model predictions including the SCHISM-ICM model and showed the predicted trends of ΔDO are the same for all the models – positive ΔDO for the mid-lower Bay channel but negative for the shallow regions. The magnitude of ΔDO for each SLR scenario is comparable (St-Laurent et al., 2019). Our model result has a similar magnitude of ΔDO as ChesROMS-ECB (Irby et al., 2018), and lies between the CH3D-ICM (Wang et al., 2017) and UMCES-ROMS-RCA (Ni et al. 2017).

3.3.3 Phytoplankton production under SLR

Changes in gross phytoplankton production (ΔGPP) have a significant impact on hypoxia in the Bay (Murphy et al., 2011). ΔGPP corresponding to SLR in the water column is positive in most areas of the Bay (Figs. 4d, 4e). For shallow areas, the magnitude of ΔGPP can reach as high as 0.4 g C m^{-2} day^{-1} for the case of a 0.5 m SLR, i.e., a 50% increase in the phytoplankton production (Figs. 4b, 4e). For the scenarios of 0.17 m and 1.0 m SLR, the increases in the local production are up to about 18% and 80%, respectively (not shown in the figure). Large values of ΔGPP (e.g. > 0.15 g C m^{-2} day^{-1}) generally occur in shallow areas (< 2 m) with relatively low values of GPP (e.g. < 0.5 g C m^{-2} day^{-1}) in Base Scenario (Figs. 4b, 4c). In tributary channels where the water depth ranges from 1 to 4 m, ΔGPP is up to 0.2 g C m^{-2} day^{-1}. In the deep areas (e.g. > 8 m) where the GPP is large in Base Scenario (e.g. 0.8 to 1.4 g C m^{-2} day^{-1}), however, ΔGPP is much smaller and can even be negative (e.g. < 0.02 g C m^{-2} day^{-1}) (Figs. 4b, 4c).

High depth-integrated chlorophyll-a concentrations (denoted by Tchla) are more concentrated in deep areas in the upper-middle part of the main Bay and deep tributaries such as the Potomac River (Fig. 3-5a-1). In contrast, high depth-averaged chlorophyll-a concentrations (denoted by Mchla) are located in shallow areas in the upper-middle Bay regions, including shallow tributaries such as the Chester River (Figs. 5d, 5g). Changes in depth-integrated chlorophyll-a concentrations (ΔTchla) generally show a similar spatial distribution as ΔGPP (Figs. 5a-2, 5a-3). However, changes in depth-averaged chlorophyll-a concentrations (ΔMchla) can be both positive and negative over the Bay (Figs. 5b-2, 5b-3).

3.4 Discussion

3.4.1 The contributions of physical and biochemical processes to DO dynamics under SLR

3.4.1.1 Physical processes

SLR results in an increase in salinity throughout the Bay and the deep channel (Fig. 3-6a). Bay-averaged ΔS is about 0.7 for the case of a 0.5 m SLR, and ΔS increases linearly with the magnitude of SLR. Results show that the length of salt intrusion also increases with SLR and the seasonal pattern agrees with predictions in Hong and Shen (2012). For example, a 0.5 m of SLR increases salt intrusion length by about 5 km on average (not shown). The increase in salinity and salinity intrusion suggests that more DO-rich coastal water can be transported into the Bay in the lower layer. This is supported by the upward oxygen at the twelve cross-sections (Fig. 3-7).

SLR drives stronger gravitational circulation, which inputs more oxygen-rich water into the lower layer of the Bay from the coast, and exports more oxygen in the upper layer (Fig. 3-7). Although there is a net outflux of oxygen from the Bay annually (Figs. 7a-3, 7b-3), the elevated bottom oxygen influx increases the bottom oxygen concentration over the lower Bay as shown in Figs. 2b-2d. Compared with other model predictions for ΔDO in the Bay (e.g. Wang et al., 2017; Ni et al., 2017; Irby et al. 2018; St-Laurent et al. 2019), our model shows the positive ΔDO is more confined in the lower Bay due to the smaller influx of bottom oxygen at the location north to the Rappahannock Shoal (Cross-section 5) (Fig. 3-7b), which is different from other model predictions (St-Laurent et al., 2019). This smaller upstream transport shown in our model could result from the highly-resolved bathymetry in SCHISM relative to other models (Cai et al., 2020).

The overall Bay-averaged stratification is strengthened with the enhanced gravitational circulation. Under SLR, the pycnocline rises *relative to the bottom* (Fig. 3-6b). Meanwhile, the vertical salinity gradient (dS/dz) *relative to the sea surface* decreases, which indicates a slight increase in the mixing of DO near the surface (Fig. 3-6c). However, this does not necessarily mean that there is a higher DO flux transported from the upper layer into the lower layer of the water column. Previous studies suggest that the time for water parcels transported from the surface to the bottom, the vertical exchange time (VET), becomes longer in estuaries under SLR (Hong and Shen, 2012). This is caused by the pycnocline rise and the increased volume below the pycnocline. Thus, although the mixing of DO may be enhanced above the pycnocline, the overall time required for the DO in the upper layer to be transported to the lower layer increases. As a result, the oxycline rises *relative to the bottom* under SLR (Fig. 3-6d), which mainly drives the overall increase of HV (Fig. 3-3). On the other hand, the DO concentration increases under SLR at the same distance below the surface (Fig. 3-6e). This could be a result of enhanced mixing in the upper layer as discussed above, but could also be a result of the increased phytoplankton production, which will be discussed in the next sections.

The contribution of lateral circulation is also studied. Under SLR, the increase in water depth in shallow areas is more pronounced than in the deep channel, which can alter the lateral circulation. The model simulation shows that the lateral channel-shore exchange is strengthened along the lateral cross-section under SLR. For example, the averaged surface velocity along the cross-channel direction over section 9 (see Fig. 3-1) increases 2.35% when SLR is 1 m. The increased channel-shore exchange is expected to transport more oxygen from shallow areas to deep channels to decrease HV. However, the lateral circulation induced DO supply is minor, which is unable to offset baseline hypoxic conditions. On the other hand, the lateral advection of

low-oxygen water contributes to the decrease in the bottom DO concentration in the shallow areas (Fig. 3-2).

3.4.1.2 Biochemical processes

The enhanced gravitational circulation, strengthened stratification, and increased water depth/volume caused by SLR, as discussed in section 3.4.1, cannot fully explain the overall increased HV in the Bay since DO concentration increased in the deep channel of the mid-lower Bay. The model also suggests that the phytoplankton production increases under SLR, which produces more oxygen through photosynthesis, but consumes more DO through respiration. Surface DO for both deep (Figs. 6d, 6e) and shallow areas (Fig. 3-8a) changes little resulting from the air-sea equilibrium and advection. The local net rate of change in DO at the surface (1.1 g m^{-3} day^{-1}, Fig. 3-8b) is smaller than the difference between DO production rate and respiration rate (1.7 g m^{-3} day^{-1}, Figs. 8c, 8d), which suggests there is a net transport of DO from the water to the atmosphere. The outflux of DO by gravitational circulation near the surface also increases. Therefore, more oxygen produced by the increased phytoplankton production under SLR does not help much to increase the bottom oxygen concentration. Furthermore, the settled organic matter, from increased phytoplankton production under SLR, contributes to more water column respiration (Fig. 3-8d). The vertical distributions of local biochemical processes share the same trend as shown in Fig. 3-8 for both deep and shallow areas. The increased phytoplankton production under SLR increases the settling of organic matter, resulting in the sediment oxygen demand. Also, the deepened water column and increased residence time prolong the retention time of increased organic matters in the water column, resulting in increased water column respirations.

3.4.1.3 DO budget

We used a simple DO budget model to evaluate the contributions of both the physical transport and local biochemical processes to hypoxia in the region between cross-sections 7 and 8 (Fig. 3-1), and quantitatively compared the contribution of each process for Base and SLR scenarios (Fig. 3-9). The dominant processes are phytoplankton production, heterotrophic respiration, and net flux physical transport. Other processes, such as air-sea exchange and nitrification, have relatively fewer contributions to the budget. Under SLR of 1 m, contributions of all dominant processes on DO budget increase. The total DO consumption increases by 11.2% (Fig. 3-9b). Although the DO influx in the bottom layer increases under SLR (Fig. 3-7), the increased net flux transports more DO out of the Bay. The increased total respiration and DO outflux overwhelm the increased DO production, which leads to more loss of DO and an enlarged HV.

3.4.2 Changes in phytoplankton production under SLR

Since both Tchla and local depth increase, the positive ΔMchla shown in certain areas indicates that the local production, especially the local growth, is enhanced due to the effect of SLR (Fig. 3-5). In other areas, especially the main stem, the local Tchla is usually at a high level though ΔMchla is negative, implying that other local processes limiting the accumulation or growth of phytoplankton. For example, Mchla is diluted by increased water depth. Also, the increased water depth and enhanced stratification reduce the upward flux of recycled nutrients from the lower layer, which reduces the nutrients supply in the surface layer for phytoplankton to take up.

The enhanced gravitational circulation affects both the transports of nutrients and phytoplankton. To quantify the export and retention of substances affected by SLR in the Bay, the freshwater age of the Bay was computed following the method in Shen and Hass (2004). The overall water age of the Bay increases with SLR. With an SLR of 0.5 m, the annual freshwater age of the Bay mouth increased by 20 to 60 days for different years from the value of about 200 days in Base Scenario (Cai et al., 2020). An increased freshwater age suggests that more nutrients will be retained inside the Bay for phytoplankton growth (Nixon et al., 1996), which is also supported by the changes in nutrient flux under SLR (Fig. 3-10). The net outfluxes of both total nitrogen (TN) and dissolved inorganic nitrogen (DIN) decrease in all the seasons (Figs. 10a-1,2; 10b-1,2); and the net influx of total inorganic phosphorus (TIP) increases during most time of a year under SLR (Figs. 10a-3, 10b-3). Besides, the Bay-wide stronger stratification tends to maintain phytoplankton in the euphotic zone.

Besides the direct effects on phytoplankton growth, accumulation and distribution, it appears that SLR reduces the growth limitations of phytoplankton in many tributaries or certain regions of large tributaries (e.g. the Choptank River, the upstream of the Potomac River). The changes of water volume (water column depth), transport and circulation, flushing time, as well as the nonlinear interactions among them, influence the local phytoplankton growth by changing the local nutrient and light availabilities, and the detailed discussion about these interactions will be presented in section 3.4.3.

3.4.3 Changes in tributaries and shallow areas

3.4.3.1 Changes of flushing time of major tributaries

As discussed above, model results show that phytoplankton production increases significantly in tributaries and shallow areas under SLR. The increase in the GPP, however, is not proportional to the volume increase in most areas. Since nutrient loadings from the watershed are unchanged, the nutrient limitation for phytoplankton growth is mainly influenced by physical processes and nutrient consumption, and nutrient is less limited in tributaries. In this case, change in nutrient limitation under SLR for phytoplankton growth is expected to be minor in tributaries and shallow areas. Flushing time was computed for each major tributary to explore the local retention and dynamic processes that affect the dynamics of phytoplankton and nutrients.

Opposite to the situation that residence time of the Bay increases under SLR, the flushing time in most tributaries in the upper Bay (e.g. the Chester River) tends to decrease with SLR (Fig. 3-11a); however, this seems a relatively minor factor (see discussions below).

The flushing time of a tributary can be expressed as

$$\tau = \frac{V}{Q} \tag{3-3}$$

where V is the total volume and Q is the flux out of tributary (Monsen et al., 2002). The change in flushing time depends on the net effect of increases in volume and flux. Although SLR increases water volume, V, which tends to increase the flushing time, it also increases flux Q, as suggested by the classic estuarine circulation theory. According to the classic estuarine circulation theory (Hansen and Rattray, 1965; MacCready and Geyer, 2009), the velocity of the exchange flow is quantified by the expression:

$$u_E = \frac{g\beta\overline{s_x}H^3}{48K_m} \tag{3-4}$$

where g is the gravitational acceleration constant, $\beta \cong 7.7 \times 10^{-4}$ PSU^{-1}, $\overline{s_x}$ is depth-averaged salinity gradient in the along-channel direction, H is water depth, and K_m is the vertical eddy viscosity. The outflux can be expressed by the production of u_E and the cross-section area. This suggests that the increase of water depth increases both the velocity of the exchange flow and cross-section area. Therefore the increase of water depth increases the water exchange and shortens the flushing time (Hansen and Rattray, 1965; Shen and Lin, 2001). Since the outflux can increase if the exchange flow increases due to the enhanced gravitational circulation, the change in flushing time ($\Delta\tau$) depends on the competition between the increases in the volume and the increase in the flux resulting from increased gravitational circulation. $\Delta\tau$ can be either positive or negative for different tributaries.

3.4.3.2 Effects of sea-level rise on light supply in tributaries

The areal phytoplankton primary production is the integration of productivity over the water column. In estuaries, phytoplankton is distributed vertically in the upper mixed layer while photosynthesis occurs in the euphotic zone. The ratio of the depth of the euphotic zone (1% of the surface irradiance) to the depth of the mixed layer can alter the light availability in the water column and hence regulate the areal phytoplankton production (Cloern, 1987; Smith and Kemp, 1995). In deep areas where the depth of the euphotic zone is greater than the depth of the mixed layer, light is fully utilized in the water column and leads to maximum phytoplankton production. However, in areas where the depth of the euphotic zone is less than the depth of the mixed layer, light cannot be fully utilized and may prevent full growth of the phytoplankton production from reaching its maximum productivity (Brawley et al., 2003; Brush and Brawley, 2009; Cloern, 1987). In these shallow areas, the whole water column is usually within the

euphotic zone and hence the light availability can often be limited by the water depth. This has been widely observed in different estuaries that phytoplankton production is often less than the maximum values in the areas where the water depth is shallower than the euphotic depth (e.g., Boyer et al., 1993; Mallin et al., 1991; Cloern, 1987). Thus, in some shallow areas of the tributaries, the increase in water depth and change in hydrodynamics as a result of SLR can have a nontrivial impact on light supply for phytoplankton growth and hence on primary production. This can be examined quantitively using the equation for primary production. The phytoplankton productivity can be expressed as gross primary production and phytoplankton biomass (Cloern et al., 2014; Qin and Shen, 2017), and the depth-integrated phytoplankton gross primary production (GPP) is the integral of productivity from the surface to the bottom:

$$GPP = \int_0^H G_z C_z dz \tag{3-5}$$

where G_z and C_z are the gross growth rate and volumetric biomass at each depth z, respectively. For shallow areas where the water depth is less than the depth of the mixed layer depth, the phytoplankton can be assumed to be homogeneously distributed at each depth (for the sake of analytical solutions), and the biomass C_z can be assumed to be independent of depth and equal to the depth-averaged biomass. Therefore, depth-integrated phytoplankton production can be expressed as:

$$GPP = G \cdot C \cdot H \tag{3-6}$$

where G is depth-averaged gross growth rate (day^{-1}), C is depth-averaged phytoplankton biomass (g C m^{-3}), and H is water depth (m). Under light limitation, gross growth rate $G = G_m \cdot f(I)$, where G_m is the temperature-dependent maximum growth rate (day^{-1}) and $f(I)$ is the daily-averaged growth-limitation function for light (Chapra, 1997):

$$f(I) = \frac{e}{K_d \cdot H} \cdot (e^{-\frac{I_0}{I_{opt}} \cdot e^{-K_d \cdot H}} - e^{-\frac{I_0}{I_{opt}}}) \quad (3\text{-}7)$$

K_d is light attenuation coefficient (m^{-1}), I_0 is incident light irradiance at the surface and I_{opt} is optimal light intensity (langleys day^{-1}). Eqs. (3-6) and (3-7) suggest that under SLR, a possible change in GPP can result from changes in water depth, H, light attenuation, K_d, or phytoplankton biomass, C. Substituting Eq. (3-7) into Eq. (3-6) reads:

$$GPP = G_m \cdot C \cdot \frac{e}{K_d} \cdot (e^{-\frac{I_0}{I_{opt}} \cdot e^{-K_d \cdot H}} - e^{-\frac{I_0}{I_{opt}}}) \quad (3\text{-}8)$$

The effect of water depth on GPP is through its comparison with the depth of the euphotic zone (denoted by H_u). If water depth $H \geq H_u$, the utilization of the light by phytoplankton in the water column is not limited by the water depth. In this case, light irradiance approaches zero at the bottom. Since light irradiance at each depth z can be described by the Beer-Lambert law, $I(z) = I_0 e^{-k_d \cdot z}$, we have $I(H) = I_0 e^{-k_d \cdot H} \approx 0$. This results that $e^{-k_d \cdot H} \approx 0$ and $e^{-\frac{I_0}{I_{opt}} \cdot e^{-K_d \cdot H}} \approx 1$. Therefore, the daily-averaged growth-limiting function for light can be simplified as:

$$f^*(I) = \frac{e}{K_d \cdot H}(1 - e^{-\frac{I_0}{I_{opt}}}) \quad (3\text{-}9)$$

We used $f^*(I)$ to denote the $f(I)$ when the utilization of the light by phytoplankton in the water column is not limited by the water depth. If the water depth is less than the depth of the euphotic zone, $H < H_u$, i.e., light can penetrate ultimately to the bottom. In this case, the utilization of the light by phytoplankton in the water column is limited by the water depth, $I(H) = I_0 e^{-k_d \cdot H} > 0$ and $e^{-\frac{I_0}{I_{opt}} \cdot e^{-K_d \cdot H}}$ is less than 1. Obviously, $f(I) < f^*(I)$.

To describe $f(I)$ in the two cases $H \geq H_u$ and $H < H_u$, the daily-averaged growth-limiting function for light may be expressed as:

$$f(I) = r \cdot f^*(I) \tag{3-10}$$

where r is a factor ranging from 0 to 1, and it has the expression:

$$r = \frac{e^{-\frac{I_0}{I_{opt}} \cdot e^{-K_d \cdot H}} - e^{-\frac{I_0}{I_{opt}}}}{1 - e^{-\frac{I_0}{I_{opt}}}} \tag{3-11}$$

For the case $H \geq H_u$, r = 1 and $f(I) = f^*(I)$. For the case $H < H_u$, r < 1, and Eq. (3-11) suggests a positive correlation between r and $K_d \cdot H$. Over shallow areas where the whole water column is within the euphotic zone when the water becomes deeper, more light energy can be utilized in the water column until the local depth exceeds the 1% light level.

Correspondingly, Eq. (3-6) can be expressed explicitly as

$$GPP = G_m \cdot r \cdot \frac{e}{K_d}\left(1 - e^{-\frac{I_0}{I_{opt}}}\right) \cdot C \tag{3-12}$$

Eq. (3-12) suggests that the change of GPP under light limitation due to SLR can be explained quantitatively by the changes in r, C, and K_d.

Among the three factors r, C, and K_d, the increase in GPP is mainly driven by the increase in r under SLR in the Bay. The model results show that K_d is not a major factor in changing GPP. Except in certain areas with an extreme high phytoplankton biomass and particulate organic matter, the main stem and the channel areas of most tributaries exhibit a decrease in light attenuation (ΔK_d < 0) under SLR, but the magnitude of ΔK_d is small (<1%; Fig. 3-11a) and its impact on phytoplankton is minor. Changes in phytoplankton biomass C are also not likely a determining factor leading to an increase in GPP in the scenaries. Model results

show that the percentage increase in C after SLR is not as high as that in GPP in tributaries, and C even decreases in some locations. The change of biomass C is determined by local and transport processes (Qin and Shen, 2017; Qin and Shen, in revision):

$$\frac{dC}{dt} = GC - R_r C - R_m C - \frac{\omega_c}{H} C - FC \tag{3-13}$$

where R_r and R_m are respiration rate (day^{-1}) and mortality rate (day^{-1}), respectively, ω_c is the settling velocity of phytoplankton (m day^{-1}), and F is the flushing rate due to transport processes (day^{-1}). In the tributaries, the overall changes in flushing in tributaries are not large compared with their values in Base Scenario, suggesting the increase in C is mainly due to changes in local processes. Among the local processes, respiration and grazing rates are kept unchanged in the model, and the increase in C can only be through an increase in production or a decrease in settling due to an increase in water depth. While it is not clear if the increase in C is mainly due to the increase in GPP or the decrease in settling, the model results show that the increase in C is not the major factor in increasing GPP. Take the Choptank River, which has the largest positive ΔMchla, as an example. The mean water depth of the Choptank River is about 3.95 m, so the change of water depth is about 12.7% under the case of a 0.5 m SLR. In this river, ΔK_d is less than 0.005 m^{-1} over the river channel, which is a small value compared to K_d of about 0.4 m^{-1}, and K_d decreases less than 1%. Hence, the combined change in $K_d \cdot H$ increases about 11.6%, which corresponds to an increase in r. Calculations of model results show that GPP increases about 25% and C increases about 10% after a 0.5 m SLR (Figures 4, 5), so Eq. (3-12) suggests that the increase in r is about 13.6% under SLR, which is more than that in C or K_d. Thus, in those areas where the water depth is less than the depth of the euphotic zone, the increase in GPP

is mainly due to the increase in r, and the mechanism that SLR increases GPP is mainly through the increase in the percent of light utilized by phytoplankton in the water column.

The current model does not simulate benthic algae or submerged vegetation. For the areas with abundant benthic producers, the interactions between pelagic and benthic producers can alter the results (Qin and Shen, 2019). Under SLR, the elevated depth enhanced GPP in the water column, which could decrease the light supply to the benthic producers. When the SLR is 0.5 m, the overall decrease in light availability at the bottom ranges from 10% to 25% in the shoals where the benthic producers are supported by excess light before SLR (Fig. 3-11b). Bottom light supply experiences little change in deep regions where the benthic producer cannot survive anyway because of the limited light supply. Although the current model does not couple a benthic algal model (e.g. Cerco and Seitzinger, 1997) to explicitly estimate the response of the benthic producers to SLR, a reduction of less than 25% on benthic production is estimated based on the PI curve for benthic algae (Pinckney and Zingmark, 1993; Dodds et al., 1999). However, the reduction of benthic production also relies on the nutrient supply and the real irradiance reaching the bottom, so future work is required for this direction.

3.5 Summary and conclusion

We utilized a 3D unstructured-grid model (SCHISM-ICM) to evaluate the influence of sea-level rise (SLR) on seasonal hypoxia and phytoplankton production in Chesapeake Bay. Three scenarios (SLR = 0.17 m, SLR = 0.5 m and SLR = 1.0 m) were assessed based on the calibrated current condition (Base Scenario) (Cai et al., 2020) for the period from 1991 to 1995. Under SLR, the bottom DO was predicted to increase in the deep channel of the mid-lower Bay, but to decrease in other areas. Peak summer hypoxic volume (HV) is estimated to increase by

about 2%, 8%, and 16% for these three scenarios, respectively, compared with Base Scenario. SLR drives a total volume change (ΔVol) of 1.96 km^3, 5.76 km^3, and 11.52 km^3, respectively; and the changes in hypoxia volume (ΔHV) account for about 10% -15% of ΔVol.

Different physical and biological drivers are found to have diverse effects, either positive or negative, on the DO budgets and HV. SLR increases the flux of oxygen-rich water from the ocean into the Bay due to increased gravitation circulation and this tends to improve bottom DO. On the other hand, the enhanced stratification and the enlarged volume below the pycnocline will make it take a longer time for oxygen to be transported from the upper layer to the lower layer of the water column. SLR slightly increases lateral circulation but the minor increase fails to significantly enhance the channel-shoal exchange that refuels oxygen in the channel. In addition to the physical contributions, SLR increases phytoplankton production as a result of longer residence times, stronger stratification, and increased light supply in shallow waters; and the production increases up to 15%, 40%, and 80% for these three SLR scenarios, respectively, which in turn increases the water column DO respiration. The increased phytoplankton production and residence time enhance the settling of organic matter to the lower layer. Consequently, more oxygen is consumed that contributes to the increase in the HV. Overall, this model study suggests that both the altered physical processes and the higher respiration under SLR contribute to the enlarged HV.

Shallow areas in tributaries are highly impacted by SLR since the increased water depths are proportionally large compared with the original depths. The model result shows the largest increase in phytoplankton production occurs in the shallow water regions. The analysis shows that the increase in water depth increases light utilization in shallow areas of many tributaries

where the whole water column is within the euphotic zone. This facilitates phytoplankton growth and therefore increases the local production in those areas.

For the sake of simplicity and comparison to other studies, the current study only considered the impact of SLR. For shallow areas and tributaries, other factors can be important as well. Four such factors are the land use (that affects nutrient supply), presence of vegetation (either submerged or emergent), presence of benthic algae, and change in temperature. These complications are left to future studies.

Literature Cited

Bever, A.J., M.A. Friedrichs, C.T. Friedrichs, M.E. Scully, and L.W. Lanerolle. 2013. "Combining Observations and Numerical Model Results to Improve Estimates of Hypoxic Volume Within the Chesapeake Bay, USA." *Journal of Geophysical Research: Oceans*, 118(10), pp.4924-4944. https:// doi.org/10.1002/jgrc.20331

Boesch, D.F., L.P. Atkinson, W.C. Boicourt, J.D. Boon, D.R. Cahoon, R.A. Dalrymple, T. Ezer, B.P. Horton, Z.P. Johnson, R.E. Kopp, and M. Li. 2013. "Updating Maryland's sea-level rise projections." https://digitalcommons.odu.edu/ccpo_pubs/154/

Boon, J.D., J.M. Brubaker, and D.R. Forrest. 2010. "Chesapeake Bay land subsidence and sea level change: An evaluation of past and present trends and future outlook." https://scholarworks.wm.edu/reports/706/

Boyer, J.N., R.R. Christian, and D.W. Stanley. 1993. "Patterns of phytoplankton primary productivity in the Neuse River estuary, North Carolina, USA." *Marine ecology progress series. Oldendorf*, 97(3), pp.287-297. https://www.int-res.com/articles/meps/97/m097p287.pdf

Brawley, J.W., M.J. Brush, J.N. Kremer, and S.W. Nixon. 2003. "Potential applications of an empirical phytoplankton production model to shallow water ecosystems." *Ecological modelling*, 160(1-2), pp.55-61. https://doi.org/10.1016/S0304-3800(02)00310-1

Cai, X., Y.J. Zhang, J. Shen, H. Wang, Z. Wang, Q. Qin and F. Ye. 2020. "A Numerical Study of Hypoxia in Chesapeake Bay Using an Unstructured Grid Model: Validation and Sensitivity to Bathymetry Representation." *Journal of the American Water Resources Association* 1–24. https://doi.org/10.1111/1752-1688.12887.

Carton, J.A. and B.S. Giese. 2008. “A reanalysis of ocean climate using Simple Ocean Data Assimilation (SODA).” *Monthly weather review*, 136(8), pp.2999-3017. https://doi.org/10.1175/2007MWR1978.1

Cerco, C.F. and T.M. Cole. 1994. “CE-QUAL-ICM: a three-dimensional eutrophication model, version 1.0. User’s Guide.” *US Army Corps of Engineers Waterways Experiments Station, Vicksburgh, MS*.

Cerco, C.F. and S.P. Seitzinger. 1997. “Measured and modeled effects of benthic algae on eutrophication in Indian River-Rehoboth Bay, Delaware.” *Estuaries*, 20(1), pp.231-248. https://doi.org/10.2307/1352733

Chapra, S.C. 1997. “Surface Water-Quality Modeling, McGraw-Hill Series in Water Resources and Environmental Engineering.”

Chassignet, E.P., H.E. Hurlburt, O.M. Smedstad, G.R. Halliwell, P.J. Hogan, A.J. Wallcraft, R. Baraille, and R. Bleck. 2007. “The HYCOM (hybrid coordinate ocean model) data assimilative system.” *Journal of Marine Systems*, 65(1-4), pp.60-83. https://doi.org/10.1016/j.jmarsys.2005.09.016

Cloern, J.E. 1987. “Turbidity as a control on phytoplankton biomass and productivity in estuaries.” *Continental shelf research*, 7(11-12), pp.1367-1381. https://doi.org/10.1016/0278-4343(87)90042-2

Cloern, J.E., S.Q. Foster, and A.E. Kleckner. 2014. “Phytoplankton primary production in the world's estuarine-coastal ecosystems.” *Biogeosciences*, 11(9), p.2477. https://doi.org/10.5194/bg-11-2477-2014

Dettmann, E.H. 2001. “Effect of water residence time on annual export and denitrification of nitrogen in estuaries: a model analysis.” *Estuaries*, 24(4), pp.481-490. https://doi.org/10.2307/1353250

Diaz, R.J. and R. Rosenberg. 1995. “Marine benthic hypoxia: a review of its ecological effects and the behavioural responses of benthic macrofauna.” *Oceanography and Marine biology: an Annual Review*, 33, pp.245-03.

Di Toro, D.M. and J.J. Fitzpatrick. 1993. “*Chesapeake Bay sediment flux model. Final report* (No. AD-A-267189/9/XAB).” Hydroqual, Inc., Mahwah, NJ (United States).

Dodds, W.K., B.J. Biggs, and R.L. Lowe. 1999. “Photosynthesis-irradiance patterns in benthic microalgae: variations as a function of assemblage thickness and community structure.” *Journal of phycology*, 35(1), pp.42-53. https://doi.org/10.1046/j.1529-8817.1999.3510042.x

Du, J. and J. Shen. 2015. “Decoupling the influence of biological and physical processes on the dissolved oxygen in Chesapeake Bay.” *Journal of Geophysical Research: Oceans*, 120(1), pp.78-93. https://doi.org/10.1002/2014JC010422

Hagy, J.D., W.R. Boynton, C.W. Keefe, and K.V. Wood. 2004. “Hypoxia in Chesapeake Bay, 1950–2001: long-term change in relation to nutrient loading and river flow.” *Estuaries*, 27(4), pp.634-658. https://doi.org/10.1007/BF02907650

Hansen, D.V. and M. Rattray Jr. 1966. “Gravitational circulation in straits and estuaries.” https://digital.lib.washington.edu/researchworks/bitstream/handle/1773/16068/M66-76.pdf?sequence=1

Hilton, T.W., R.G. Najjar, L. Zhong, and M. Li. 2008. “Is there a signal of sea-level rise in Chesapeake Bay salinity?” *Journal of Geophysical Research: Oceans*, 113(C9). https://doi.org/10.1029/2007JC004247

Hong, B. and J. Shen. 2012. “Responses of estuarine salinity and transport processes to potential future sea-level rise in Chesapeake Bay.” *Estuarine, Coastal and Shelf Science*, 104, pp.33-45. https://doi.org/10.1016/j.ecss.2012.03.014

Irby, I.D., M.A. Friedrichs, F. Da, and K.E. Hinson. 2018. “The competing impacts of climate change and nutrient reductions on dissolved oxygen in Chesapeake Bay.” *Biogeosciences*, 15(9), pp.2649-2668. https://doi.org/10.5194/bg-15-2649-2018

Kemp, W.M., P. Sampou, J. Caffrey, M. Mayer, K. Henriksen, and W.R. Boynton. 1990. “Ammonium recycling versus denitrification in Chesapeake Bay sediments.” *Limnology and Oceanography*, 35(7), pp.1545-1563. https://doi.org/10.4319/lo.1990.35.7.1545

Kemp, W.M., P.A. Sampou, J. Garber, J. Tuttle, and W.R. Boynton. 1992. “Seasonal Depletion of Oxygen from Bottom Waters of Chesapeake Bay: Roles of Benthic and Planktonic Respiration and Physical Exchange Processes.” *Marine Ecology Progress Series*, pp.137-152. www.jstor.org/stable/24829928

MacCready, P. and W.R. Geyer. 2009. “Advances in estuarine physics.” *Annual Review of Marine Science*, Vol. 2: 35-58. https://doi.org/10.1146/annurev-marine-120308-081015

Mallin, M.A., H.W. Paerl, and J. Rudek. 1991. “Seasonal phytoplankton composition, productivity and biomass in the Neuse River estuary, North Carolina.” *Estuarine, Coastal and Shelf Science*, 32(6), pp.609-623. https://doi.org/10.1016/0272-7714(91)90078-P

Mesinger, F., G. DiMego, E. Kalnay, K. Mitchell, P.C. Shafran, W. Ebisuzaki, D. Jović, J. Woollen, E. Rogers, E.H. Berbery, and M.B. Ek. 2006. "North American Regional Reanalysis." *Bulletin of the American Meteorological Society*, *87*(3), pp.343-360. https://doi.org/10.1175/BAMS-87-3-343

Monsen, N.E., J.E. Cloern, L.V. Lucas, and S.G. Monismith. 2002. "A comment on the use of flushing time, residence time, and age as transport time scales." *Limnology and oceanography*, 47(5), pp.1545-1553. https://doi.org/10.4319/lo.2002.47.5.1545

Murphy, R.R., W.M. Kemp, and W.P. Ball. 2011. "Long-term Trends in Chesapeake Bay Seasonal Hypoxia, Stratification, and Nutrient Loading." *Estuaries and Coasts*, *34*(6), pp.1293-1309. doi: 10.1007/s12237-011-9413-7

Najjar, R.G., C.R. Pyke, M.B. Adams, D. Breitburg, C. Hershner, M. Kemp, R. Howarth, M.R. Mulholland, M. Paolisso, D. Secor, and K. Sellner. 2010. "Potential climate-change impacts on Chesapeake Bay." *Estuarine, Coastal and Shelf Science*, 86(1), pp.1-20. https://doi.org/10.1016/j.ecss.2009.09.026

Newcombe, C.L. and W.A. Horne.1938. Oxygen-poor Waters of the Chesapeake Bay. *Science*, *88*(2273), pp.80-81. doi: 10.1126/science.88.2273.80

Ni, W., M. Li, A. Ross, and R.G. Najjar. 2017. "Downscaling climate projections for Chesapeake Bay hypoxia in the mid-21st century." 24th Biennial CERF Conference. CERF.

Nixon, S.W., J.W. Ammerman, L.P. Atkinson, V.M. Berounsky, G. Billen, W.C. Boicourt, W.R. Boynton, T.M. Church, D.M. Ditoro, R. Elmgren, and J.H. Garber. 1996. "The Fate of

Nitrogen and Phosphorus at the Land-Sea Margin of the North Atlantic Ocean." *Biogeochemistry*, *35*(1), pp.141-180. https://doi.org/10.1007/BF02179826

Pinckney, J. and R.G. Zingmark. 1993. "Photophysiological responses of intertidal benthic microalgal communities to in situ light environments: methodological considerations." *Limnology and oceanography*, 38(7), pp.1373-1383. https://doi.org/10.4319/lo.1993.38.7.1373

Qin, Q. and J. Shen. 2017. "The contribution of local and transport processes to phytoplankton biomass variability over different timescales in the Upper James River, Virginia." *Estuarine, Coastal and Shelf Science*, *196*, pp.123-133. https://doi.org/10.1016/j.ecss.2017.06.037

Scully, M.E. 2010. "Wind modulation of dissolved oxygen in Chesapeake Bay." *Estuaries and Coasts*, 33(5), pp.1164-1175. https://doi.org/10.1007/s12237-010-9319-9

Scully, M.E. 2013. "Physical controls on hypoxia in Chesapeake Bay: A numerical modeling study." *Journal of Geophysical Research: Oceans*, 118(3), pp.1239-1256. https://doi.org/10.1002/jgrc.20138

Seliger, H.H., J.A. Boggs, and W.H. Biggley. 1985. "Catastrophic Anoxia in the Chesapeake Bay in 1984." *Science*, *228*(4695), pp.70-73. doi: 10.1126/science.228.4695.70

Shen, J. and L. Haas. 2004. "Calculating Age and Residence Time in the Tidal York River Using Three-Dimensional Model Experiments." *Estuarine, Coastal and Shelf Science*, *61*(3), pp.449-461. https://doi.org/10.1016/j.ecss.2004.06.010

Shen, J., B. Hong, and A.Y. Kuo. 2013. "Using timescales to interpret dissolved oxygen distributions in the bottom waters of Chesapeake Bay." *Limnology and Oceanography*, 58(6), pp.2237-2248. https://doi.org/10.4319/lo.2013.58.6.2237

Shenk, G.W. and L.C. Linker. 2013. "Development and Application of the 2010 Chesapeake Bay Watershed Total Maximum Daily Load Model." *JAWRA Journal of the American Water Resources Association*, *49*(5), pp.1042-1056. https://doi.org/10.1111/jawr.12109

Smith, E.M. and W.M. Kemp. 1995. "Seasonal and regional variations in plankton community production and respiration for Chesapeake Bay." *Marine ecology progress series. Oldendorf*, 116(1), pp.217-231. http://www.int-res.com/articles/meps/116/m116p217.pdf

St-Laurent, P., M.A.M. Friedrichs, M. Li, and W. Ni. 2019. "Impacts of sea level rise on hypoxia in Chesapeake Bay: A model intercomparison." Report to Virginia Tech and Chesapeake Bay Program, October 2019, 34 pp. https://scholarworks.wm.edu/reports/2310/

Taft, J.L., W.R. Taylor, E.O. Hartwig, and R. Loftus. 1980. "Seasonal Oxygen Depletion in Chesapeake Bay." *Estuaries*, *3*(4), pp.242-247. http://www.jstor.com/stable/1352079

Wang, P., L. Linker, H. Wang, G. Bhatt, G. Yactayo, K. Hinson, and R. Tian. 2017. "Assessing water quality of Chesapeake Bay by the impact of sea level rise and warming." In IOP Conference Series: Earth and Environmental Science(Vol. 82, No. 1, p. 012001). https://iopscience.iop.org/article/10.1088/1755-1315/82/1/012001/meta

Vaquer-Sunyer, R. and C.M. Duarte. 2008. "Thresholds of hypoxia for marine biodiversity." *Proceedings of the National Academy of Sciences*, 105(40), pp.15452-15457. https://doi.org/10.1073/pnas.0803833105

Xiong, J., J. Shen, Q. Qin, and J. Du. 2021. “Water exchange and its relationships with external forcings and residence time in Chesapeake Bay.” *Journal of Marine Systems*, 215, p.103497. https://doi.org/10.1016/j.jmarsys.2020.103497

Zervas, C. 2001. “Sea level variations of the United States, 1854-1999 (Vol. 36)”. US Department of Commerce, National Oceanic and Atmospheric Administration, National Ocean Service.

Zhang, Y.J., E. Ateljevich, H.C. Yu,, C.H. Wu and C.S. Jason. 2015. “A New Vertical Coordinate System for a 3D Unstructured-Grid Model.” *Ocean Modelling*, *85*, pp.16-31. https://doi.org/10.1016/j.ocemod.2014.10.003

Zhang, Y.J., F. Ye,, E.V. Stanev and S. Grashorn. 2016. “Seamless Cross-Scale Modeling with SCHISM.” *Ocean Modelling*, *102*, pp.64-81. https://doi.org/10.1016/j.ocemod.2016.05.002

Figures for Chapter 3

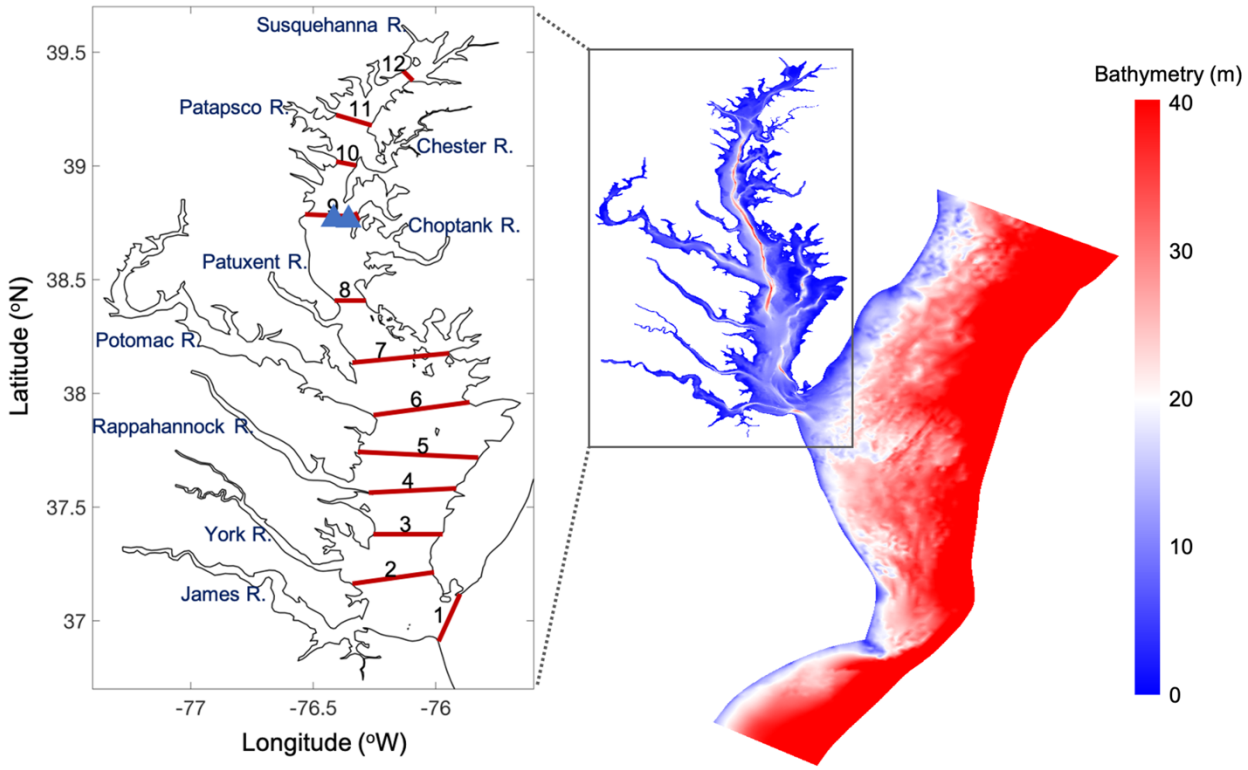

Fig. 3-1: Model domain for Chesapeake Bay and its tributaries, with the 12 cross channel sections (red lines). Two blue triangles denote the locations used for vertical profile analysis.

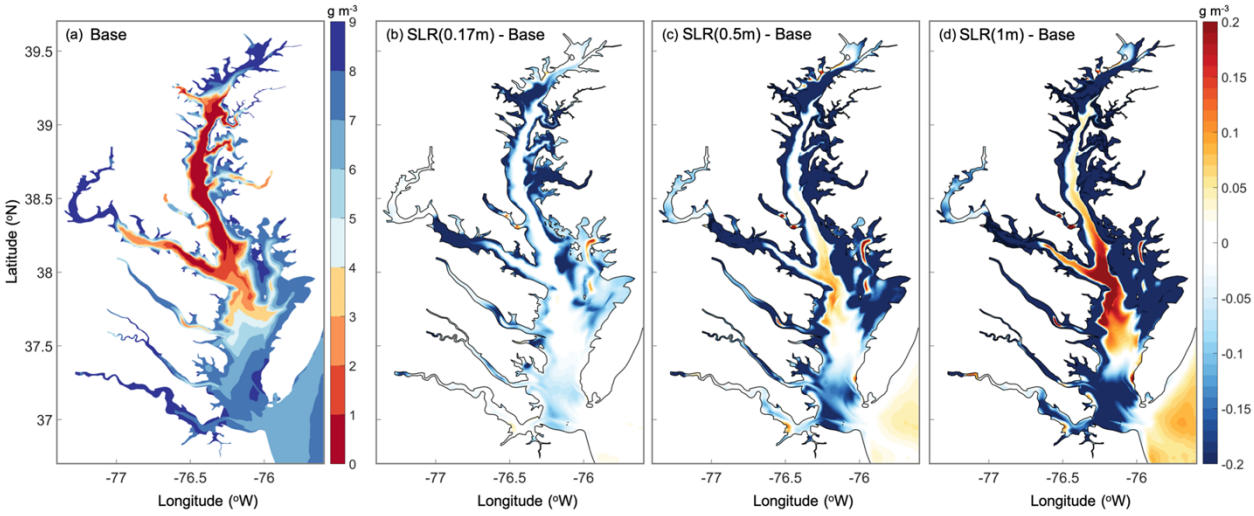

Fig. 3-2: (a) Five-year averaged bottom DO concentrations in Base Scenario, and (b, c, and d) absolute differences between SLR (0.17 m, 0.5 m, and 1 m) to Base Scenarios from June to August.

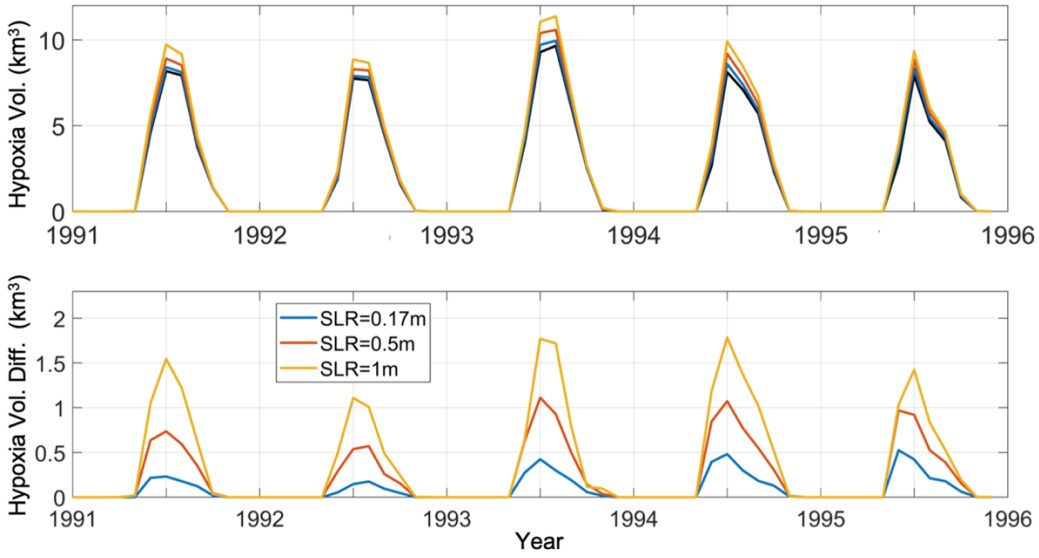

Fig. 3-3: Hypoxic volume and difference under SLR scenarios of 0.17 m, 0.5 m, and 1.0 m. The black line in the upper panel is from Base Scenario.

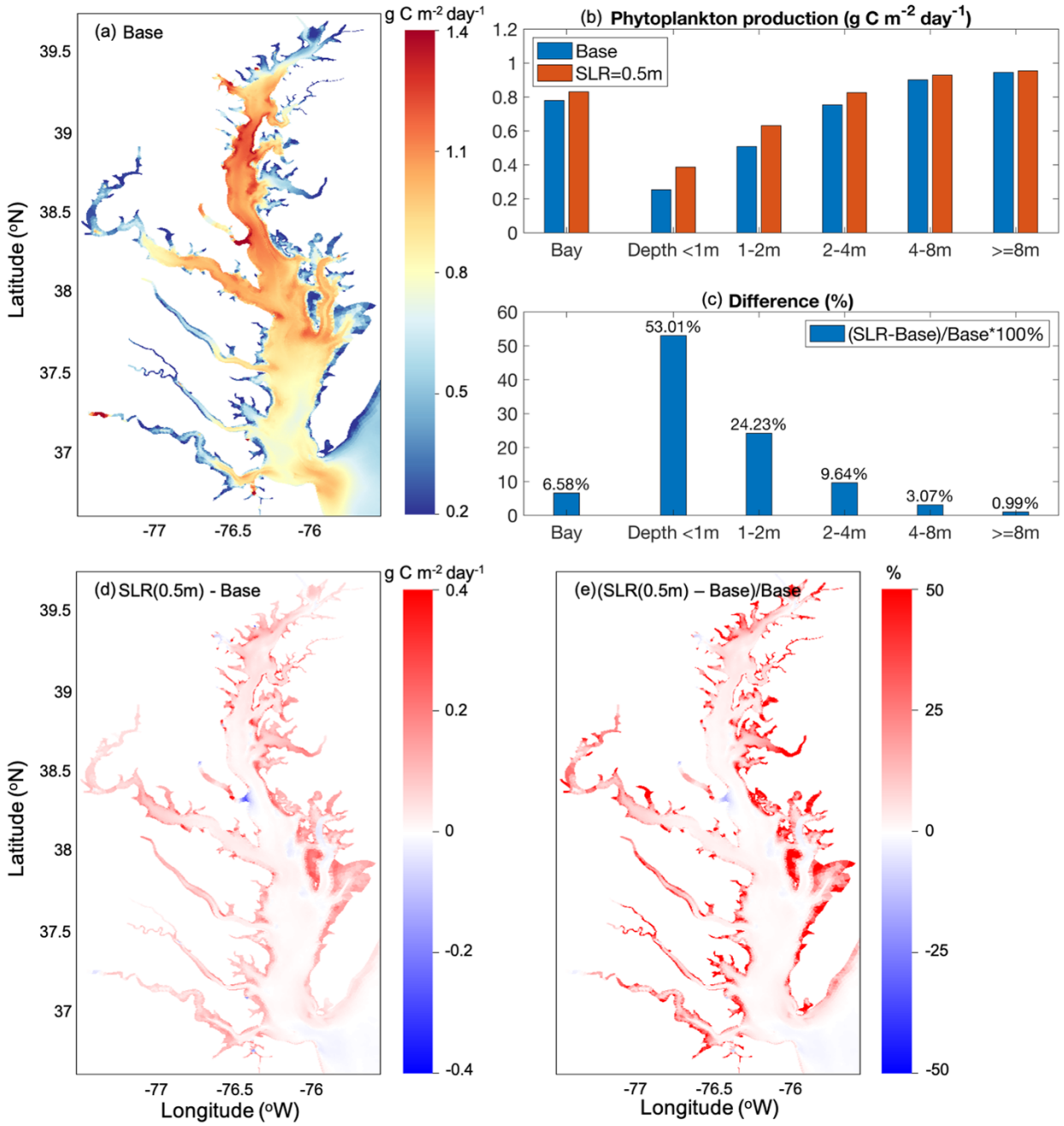

Fig. 3-4: Five-year averages of gross phytoplankton production (depth-integrated) from April to June: (a) horizontal distribution in Base Scenario, (b) averages in areas of different water depths for Base Scenario and SLR = 0.5 m, (c) relative difference between Base Scenario and SLR = 0.5 m at different water depths, and horizontal distribution of (d) absolute difference and (e) relative difference caused by SLR = 0.5 m on Base Scenario.

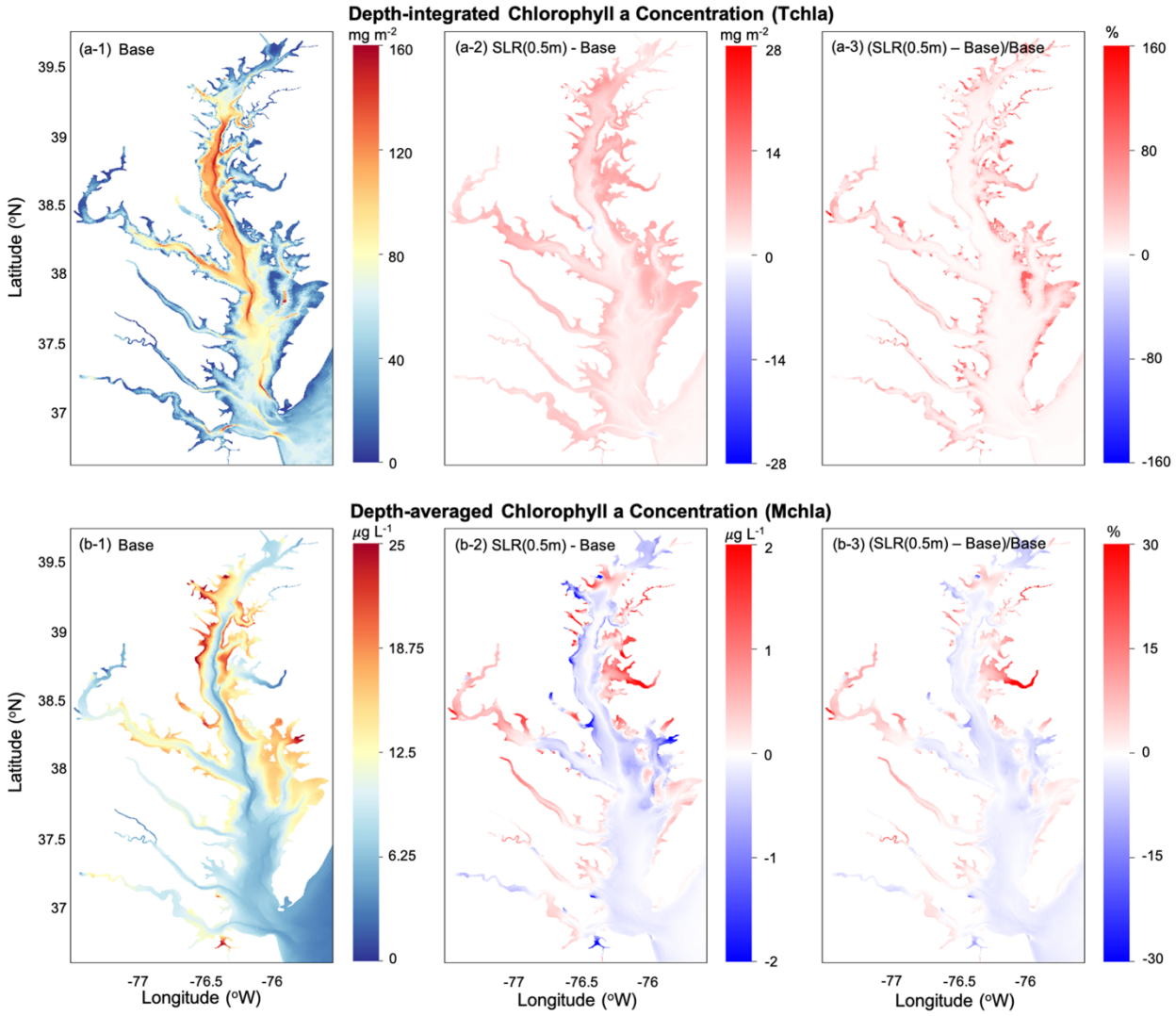

Fig. 3-5: Five-year averages of (a) depth-integrated and (b) depth-averaged chlorophyll-a concentration from April to June, respectively, for (a, b-1) Base Scenario, (a, b-2) absolute difference and (a, b-3) relative difference caused by SLR = 0.5 m on Base Scenario.

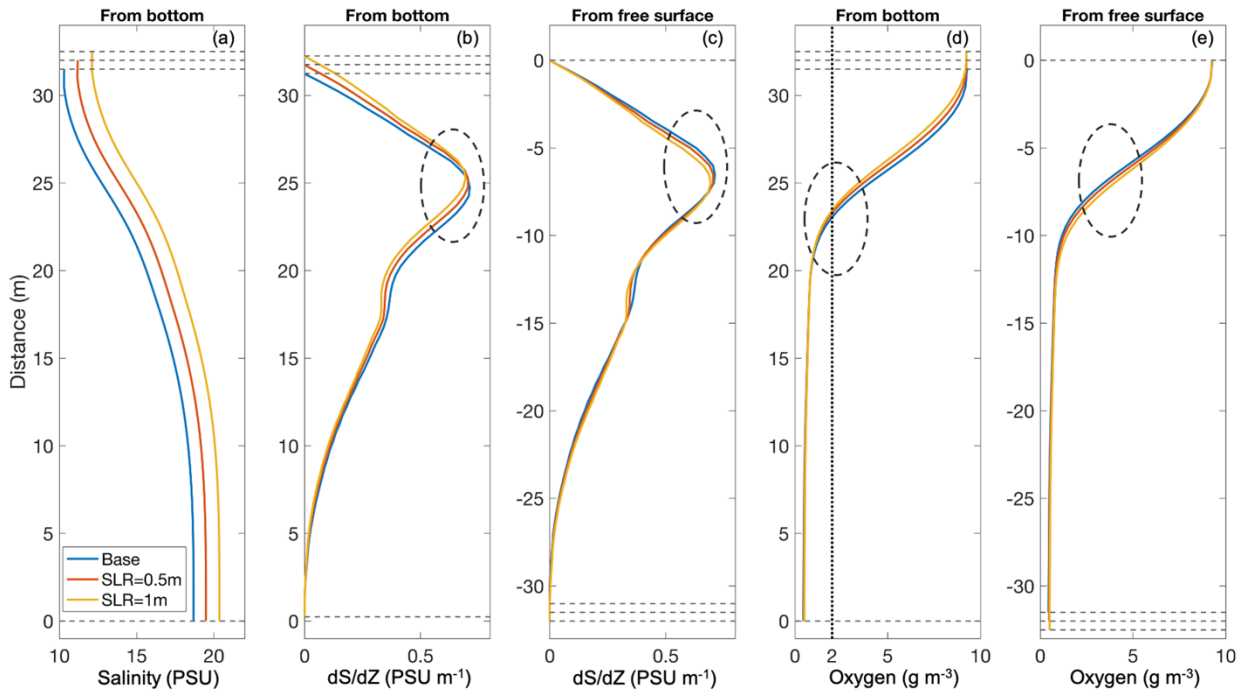

Fig. 3-6: Five-year averages of the vertical distribution of (a) salinity (b, c) dS/dz, and (e,f) DO at a deep location in the hypoxic zone (Fig. 3-1) from June to August. Profiles (a, b, and d) relative to the bottom and (c, e) relative to the water surface are provided.

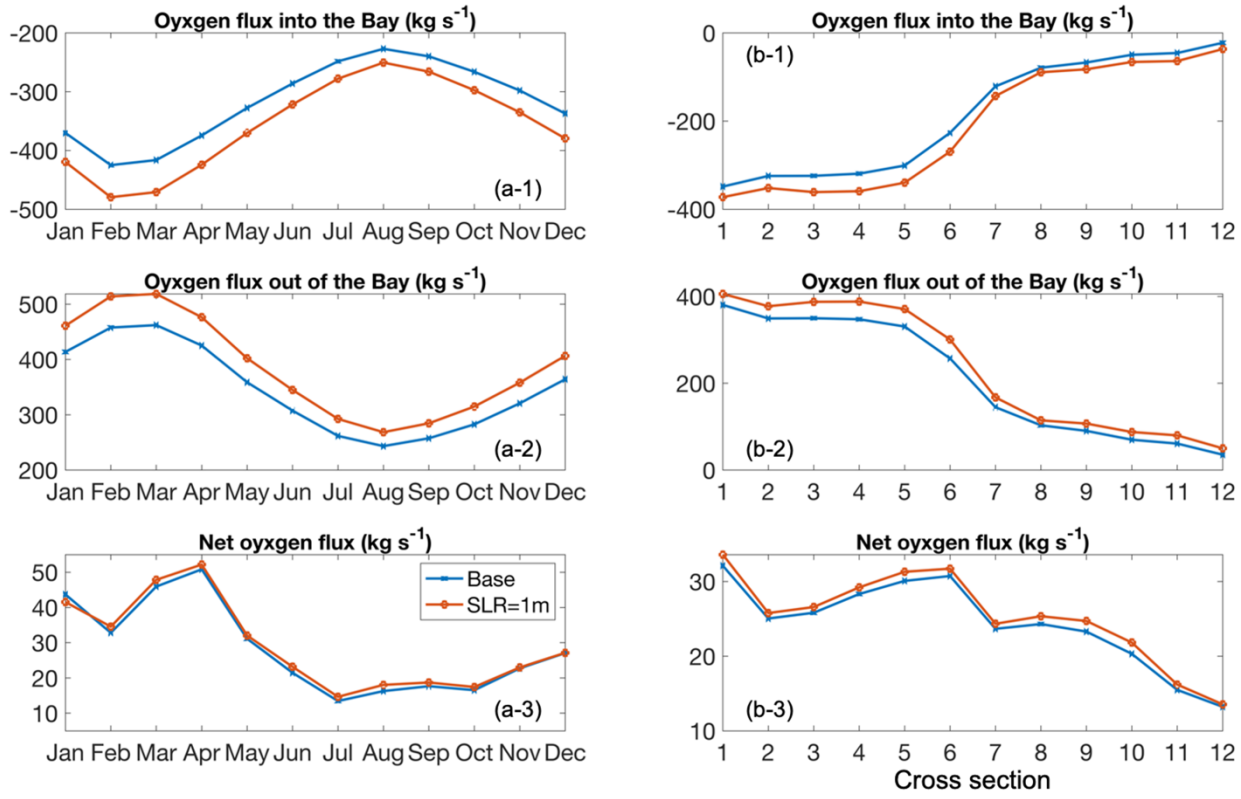

Fig. 3-7: (a) Five-year averages of oxygen flux for each month from 1991 to 1995 at cross-section 4 near Rappahannock Shoal (Fig. 3-1); (b) Five-year averages of annual oxygen flux from 1991 to 1995 at the 12 cross-sections Bay mouth to head. Panels (a, b-1) are influx, panels (a, b-2) are outflux, and panels (a, b-3) are the net oxygen flux. Negative values mean flux into the Bay while positive values refer to outflux.

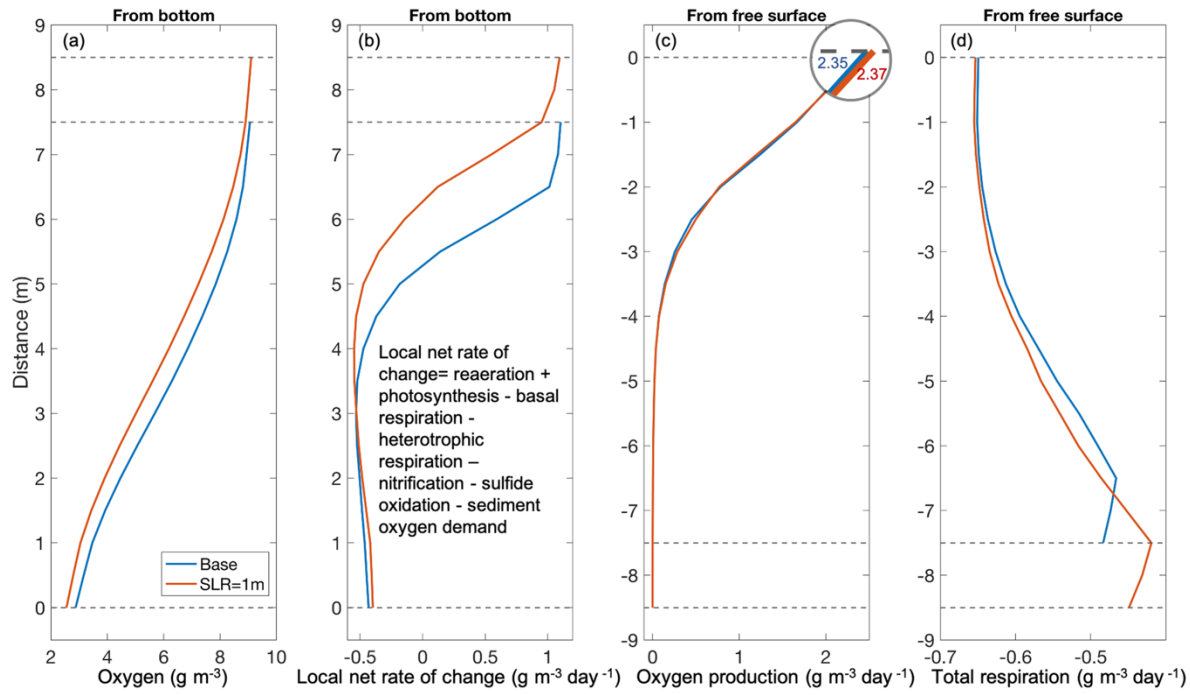

Fig. 3-8: (a) Five-year averages of the vertical distribution of DO at a shallow location in cross-section 9 (Fig. 3-1). (b) The local net rate of change resulting from the local processes controlling the DO budget, including reaeration, phytoplankton photosynthesis, basal respiration, heterotrophic respiration, nitrification, sulfide oxidation, and sediment oxygen demand. (c) The rate of local oxygen productions. (d) The rate of total local oxygen consumption, including basal respiration, heterotrophic respiration, nitrification, sulfide oxidation, and sediment oxygen demand. The averages are calculated for July.

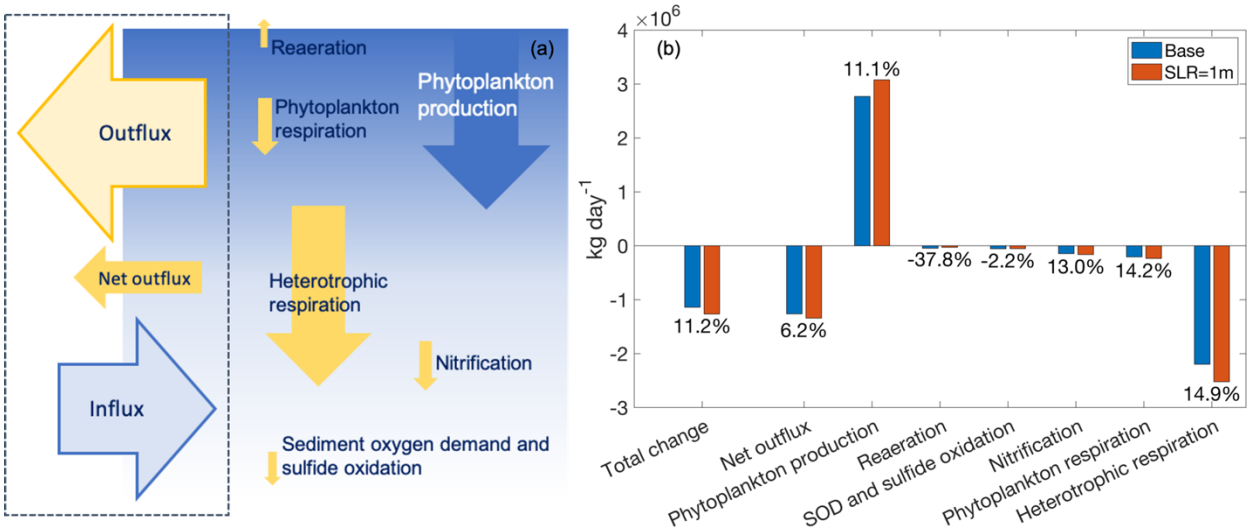

Fig. 3-9: Five-year averages of the contribution of each physical or biological process to the DO budget in the area between cross-sections 7 and 8 (Fig. 3-1) from June to August, for Base and SLR Scenarios. (a) Diagram of the contribution of each process to the DO budget, where the width of the arrow is generally proportional to the averaged contribution. Blue arrows indicate source terms of the DO budget and yellow arrows indicate sink terms of the DO budget. (b) Bar plots of each term in the DO budget, with the change percentages (SLR-Base)/Base labeled.

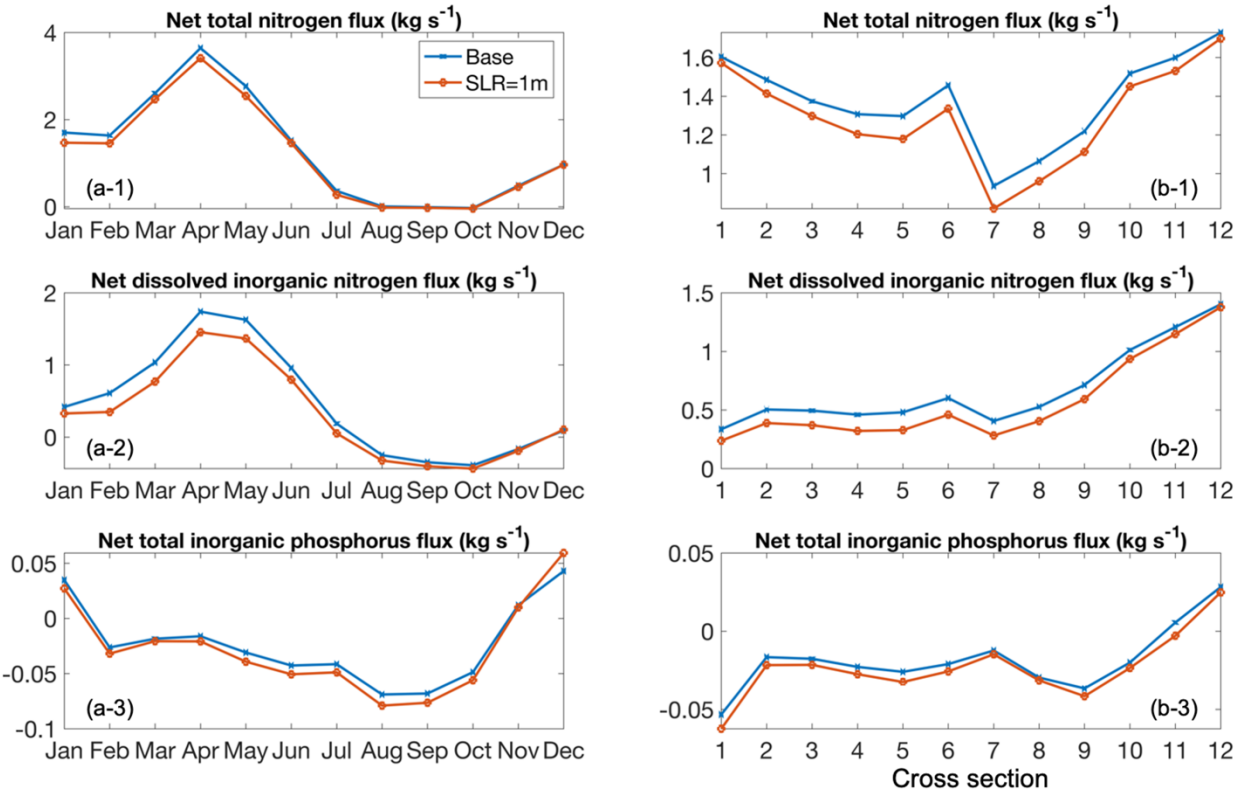

Fig. 3-10: (a) Five-year averages of net nutrient flux for each month from 1991 to 1995 at cross-section 4 near Rappahannock Shoal (Fig. 3-1); (b) Five-year averages of annual net nutrient flux from 1991 to 1995 at the 12 cross-sections Bay mouth to head. Panels (a, b-1) are total nitrogen, panels (a, b-2) are dissolved inorganic nitrogen (DIN) and panels (a, b-3) are total inorganic phosphorus. Negative values mean flux into the Bay while positive values refer to outflux.

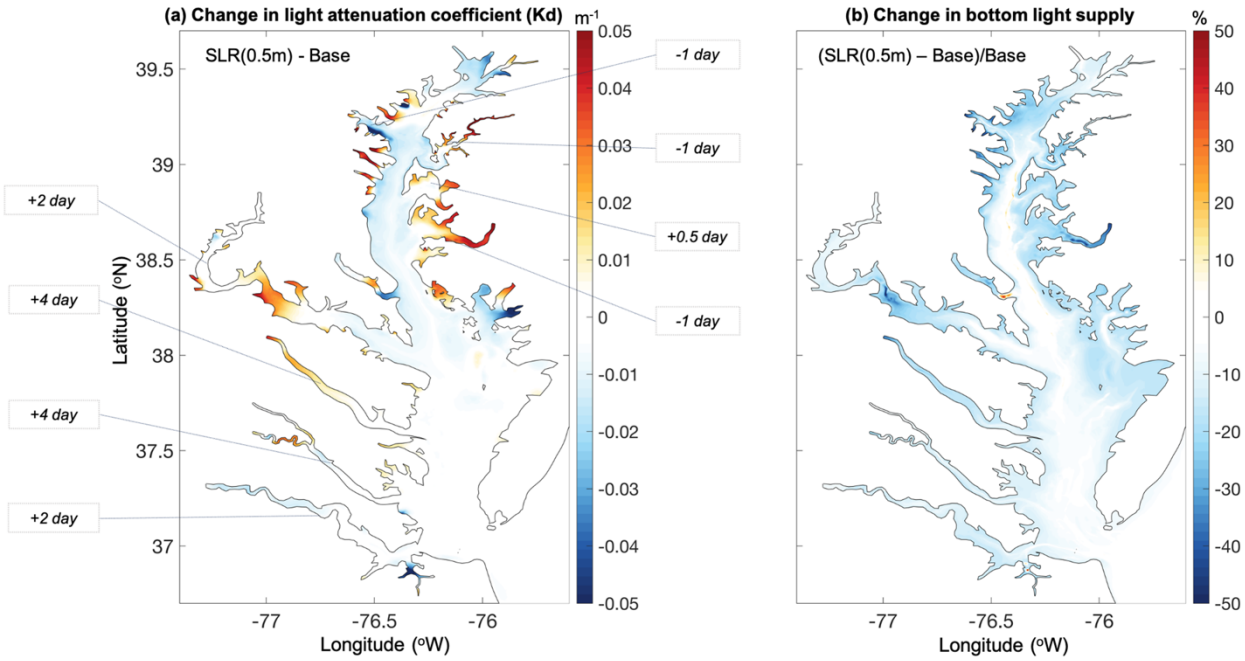

Fig. 3-11: (a) Difference of depth-averaged light attenuation coefficient ($\boldsymbol{K_d}$) caused by SLR of 0.5 m from April to June. Side labels in days indicate the estimated change of flushing time caused by an SLR of 0.5 m for each major tributary. (b) The relative difference of bottom light supply from April to June caused by SLR = 0.5 m on Base Scenario

Chapter 4

4. The roles of tidal marshes in the estuarine biochemical dynamics: a numerical modeling study

Abstract

Multiple observations suggest that the existence of tidal marsh can alter the oxygen and nutrient dynamics in adjacent water bodies, but accessing the impacts of large tidal marshes on an estuary is challenging. In this study, we use a modeling approach to investigate the roles of tidal marshes on the estuarine biochemical processes. The marsh model, which simulates the ecological functions of marshes at seasonal and annual time scales, is embedded inside an unstructured-grid three-dimensional hydrodynamic and eutrophication model (SCHISM-ICM). This modeling system simulates the growth and metabolism of the tidal marsh plants and links biological processes to nutrient dynamics in the water column and sediment. This model dynamically simulates both nutrient recycling and physical transport of the materials between marshes and open water through wetting-drying processes. This coupled model system is validated and applied to the York River Estuary successfully, where extensive tidal marshes exist. Model results suggest that tidal marshes influence the local diurnal DO cycle by exporting dissolved organic carbon and high sediment oxygen demand in the marsh system through the tidal exchange. The high deposition of organics and diurnal DO cycle enhance the sediment release of phosphorus. On the other hand, marshes tend to decrease dissolved inorganic nitrogen in the water column by settling particulate nutrients and enhancing the denitrification process. Furthermore, marshes also affect water column phytoplankton production by changing nutrient availability, but the phytoplankton dynamics in the York River Estuary are mainly controlled by flushing and light. The study demonstrates that tidal marshes have substantial impacts on the estuarine biochemical processes.

4.1 Introduction

Highly productive tidal marshes play a key role in the estuarine ecosystem by affecting the dynamics of carbon, nitrogen, phosphorus, and oxygen (Chmura, 2003; Bridgham et al., 2006). Sedimentation is greatly enhanced in the tidal marshes due to enhanced flow impedance locally and the tidal marshes tend to be traps of particulate material, therefore retaining a significant amount of carbon and other nutrients (Grant and Partick, 1970; Bowden et al., 1991; Ziegler et al., 1999; Sundareshwar et al., 2003); in addition, dissolved nutrients are also observed to be exported or filtered from the tidal marshes in some systems (Axelrad et al., 1976; Jordan et al., 1983; Chambers et al., 1992; Anderson et al., 1997). In some areas, the tidal marshes tend to export excess materials, including organic carbon and other nutrients, into adjacent waters and thus enhance estuarine productivity in these systems (Odum et al., 1984; Ridd et al, 1988; Wolanski et al., 2008; Tzortziou, et al, 2011; Alongi, 2020; Czapla et al., 2020). Diverse results of the exported or filtered dissolved organic carbon were observed at different estuaries (Neubauer and Anderson, 2003; Czapla et al., 2020; Bukaveckas, 2021). The remineralization of the abundant organic matter, which can be directly from the marshes or the increased local estuarine productivity, is suggested to cause excessive consumption of dissolved oxygen (DO) (Diaz and Rosenberg, 2001; Levin et al., 2009). The observed low-DO events (hypoxia when DO concentration is lower than 2 mg L^{-1}) near tidal marshes usually follow a diurnal pattern, with lower DO occurring at low tide (Swarth et al., 1993). Also, bottom fluxes of ammonium and phosphate can be enhanced due to the marsh-induced low-DO events or the low sediment redox potentials (Lai and Lam, 2008). Therefore, tidal marshes play an important role in modifying the estuarine biochemical dynamics, at variable time scales and in different systems. The complex dynamics and interaction of marsh and the estuarine water are difficult to fully analyze. Studies

with observation methods to investigate the role of tidal marshes usually focus on a limited number of small systems due to the difficulty in conducting the measurements and calculations. Numerical models, on the other hand, can investigate individual processes in isolation by doing unmeasurable scenarios. In addition, modeling studies can be applied at a larger spatial scale (e.g., the York River Estuary) to study the role of tidal marshes on the estuarine biochemical processes.

Current marsh models usually focus on the long-term process of marsh morphology and evolution on the decadal to centurial timescales (Morris, 2002; Fagherazzi et al., 2004; Kirwan and Murray, 2007; Marani et al., 2007; Townend et al., 2010; Alizad et al., 2016). These models usually account for the feedback between marsh biomass, platform elevation, and sedimentation, with no particular attention paid to biochemical processes away from the marshes (Morris et al., 2002; Fagherazzi et al., 2012; Alizad et al., 2016). On the other hand, another type of marsh model mainly focuses on the short-term biological functions of the marsh plants considering their impacts on the surrounding system on seasonal to annual timescales (Buzzelli et al., 1999; Cerco and Tian, 2021). However, this type of marsh model is mostly used as offline box models using additional source/sink terms to represent marsh function in the water quality variables' mass balance equation, for which the marsh growth, respiration, and nutrient recycles are not coupled into hydrodynamic-water quality models for system-wide simulations due to the challenges of fine resolution as required to account for the patchiness of the marsh. Ideally, the marsh habitat studies would require the model domain coverage to include the inter-tidal flooding zone as well as the surrounding environment, so the numerical model must be sufficiently robust to handle the inundation processes (Zhang et al., 2016).

In this study, we developed a marsh modeling approach for studying the role of the tidal marsh on estuarine biochemical processes. This marsh model is coupled with an unstructured-grid three-dimensional hydrodynamics and water quality model to simulate both physical and biogeochemical processes in an entire estuarine system, including the marsh wetlands and the surrounding waters. The marsh-induced form drag is included in the momentum equation and the marsh-induced turbulence is added as an additional source term in the turbulence closure equations (Zhang et al., 2020). This model explicitly simulates the interactions between marsh and estuarine biochemical processes, such as the nutrient release from the marsh metabolism and bottom sediment to the water column. By fully coupling hydrodynamic, water quality, and marsh modules, we can simultaneously simulate the multiple nonlinear interactions between the physiological processes of the marsh, physical processes, and biochemical processes in an estuary (the York River Estuary). This process-based model can be used to study the effects of tidal marshes on water quality on a relatively large regional scale (e.g., the York River Estuary and the Chesapeake Bay), to complement direct observations.

In the Methods section, we describe the study site, available data, model development, a benchmark for its development, model implementations, the design of sensitivity tests, and the analysis methods. In the Results section, we present the model skill assessments for its implementation in the York River Estuary, which includes the simulation of the physical environment, the major water quality properties, and the marsh biomass and productivity. In the Discussion section, we discuss the roles of the tidal freshwater marshes on the biochemical processes by focusing on the responses of estuarine nutrients and phytoplankton revealed by the sensitivity tests, especially a marsh removal scenario (NV0) that omits the ecological functions of the marsh. We will also discuss the uncertainty and limitations of the current model

framework and the direction of future studies. A short conclusion is presented in the Summary and conclusion section.

4.2 Methods

4.2.1 Study site and available data

The Pamunkey River and Mattaponi River are tidal rivers joined at West Point to form the York River (Fig. 4-1), which is one of the major tributaries in the lower Chesapeake Bay (the Bay thereafter). The mean discharge of the Pamunkey River and Mattaponi Rivers are 28.7 m^3 s^{-1} and 14.4 m^3 s^{-1}, respectively, but the total discharge into the York from these two rivers can be more than 107 m^3 s^{-1} during wet seasons (Shen and Haas, 2004). The York estuary is a microtidal estuary, whose mean tidal range increases from 0.7 m at the mouth to 0.85 m at the West Point and exceeds 1.0 m at the heads of the Pamunkey and Mattaponi Rivers according to the historical data (https://tidesandcurrents.noaa.gov/historic_tide_tables.html). The Pamunkey-Mattaponi-York system has a mean residence time of 104 days under the mean flow condition (Shen and Haas, 2004). The upper portion of the Pamunkey and Mattaponi Rivers are tidal fresh while the location of transition to freshwater varies with river discharge (Shen and Haas, 2004). Salinity at the West Point ranges from 0 to 20 PSU and varies with freshwater discharge (https://www.chesapeakebay.net/what/data). The annual temperature follows a seasonal trend with 25.7 ^oC at annual highs and 0.9 ^oC at annual lows (Brooks, 1983). The average precipitation is about 95.9 cm in this region, typically the highest in July and August (Brooks, 1983). Waves are usually considered to be insignificant in this region (Friedrichs, 2009).

The Pamunkey River has over 28.9 km^2 of tidal marshes and forested wetlands adjacent to the meandering channels, located within 72 kilometers from the West Point (Fig. 4-1; Perry,

1991; Mitchell et al., 2017). On the Mattaponi side, tidal marshes are found from the West Point to approximately 50 kilometers upstream, occupying an area of 21.7 km^2 (Fig. 4-1; Mitchell et al., 2017). These marshes as marked in Fig. 4-1c account for 97.27% of the total marsh coverage in the York River Estuary, excluding the extensive or embayed marshes in the sheltered sub-tributaries such as Morris Bay and Ware Creeks (Fig. 4-1a; Mitchell et al., 2017). Overall, there is a continuum of marsh types from tidal oligohaline marshes to non-tidal freshwater marshes along the Pamunkey and Mattaponi Rivers (Perry, 1991). Over the past 40 years, the total area of tidal freshwater and brackish marshes along the Pamunkey and Mattaponi Rivers has changed little (< 0.009%), although the brackish marshes have replaced some tidal freshwater species (Mitchell et al., 2017).

We utilize the database of water quality monitoring networks in the York River Estuary from the Chesapeake Bay Program (CBP; https://www.chesapeakebay.net/what/data), which has a wide coverage of variables — including nutrients, sediments, planktons, water temperature, salinity, and DO. The frequency of these measurements is once (winter) or twice (summer) each month. This database has full spatial coverage from the tidal freshwater region to the mouth of the York River (Fig. 4-1). In addition to this database, we also use some high-frequency (15-minute intervals) observations of salinity and elevation from Chesapeake Bay National Estuarine Research Reserve (CBNERR; http://cdmo.baruch.sc.edu) and Virginia Estuarine and Coastal Observing System (VECOS; http://vecos.vims.edu). The delineation of the marshes follows the USGS topography map (https://www.usgs.gov/core-science-systems/national-geospatial-program/us-topo-maps-america?qt-science_support_page_related_con=0#qt-science_support_page_related_con).

4.2.2 Model development

The fully coupled hydrodynamic-water quality-marsh model was developed within Semi-implicit Cross-scale Hydroscience Integrated System Model (SCHISM), an open-source community-supported modeling system (Zhang et al., 2016). The water quality Integrated Compartment Model (ICM; Cerce and Cole, 1994), which was developed by the U.S. Army Corps of Engineering Research and Development Center, was fully coupled with SCHISM (Cai et al., 2020). Besides the 21 water quality variables (e.g., phytoplankton, carbon, nitrogen, phosphorus, and oxygen), the benthic algae are also included in this model (Cerco and Seitzinger, 1997). We developed the marsh module in a similar approach as the SAV module (Cai, 2018) but modified and added specific processes of marsh plants. Three types of marshes (salt marsh, brackish marsh, and freshwater marsh) were added to the group of primary producers in the ecosystem model. The primary producers (e.g., phytoplankton and marsh plants) interact with each other through competition for light and nutrient supplies (Fig. 4-2). The marsh-induced drag force and turbulence were fully incorporated in the hydrodynamic model and the interaction between the marsh and hydrodynamics was dynamically simulated (Zhang et al., 2020).

The kinetic marsh model shares a similar structure as the submerged aquatic vegetation model (Cerco and Moore, 2001; Cai, 2018). The marsh plant is divided into three tissues that are modeled respectively – leaf, stem, and root. The leaf is the only tissue that is photosynthetic and transfers its production to other tissues. The growth of the leaf is controlled by multiple limiting factors – temperature, light supplies, salinity stress, and inundation pressure. Although nutrients affect the growth of the plants, the nutrient supply is assumed to be sufficient from the sediment to support the growth of the marsh, so the nutrients are not considered as a limiting factor in this

model. Inundation stress is suggested by the observations to include in the model design, where longer inundation duration and deeper flooding tend to reduce marsh growth (McHugh and Dighton, 2004; Janousek and Mayo, 2013; Watson et al., 2015). Metabolisms of leaf and stem, mostly defoliation, reduce the above-ground biomass. The plant height is calculated as a linear function of the above-ground biomass. The mathematic formulas of the biomass of the three tissues and the canopy height are:

$$\frac{d\,\boldsymbol{LF}}{dt} = Plf(T,I,S,F)\cdot(1-Fam)\cdot FPlf\cdot \boldsymbol{LF} - MTlf(T)\cdot BMlf(T)\cdot \boldsymbol{LF} \tag{4-1}$$

$$\frac{d\,\boldsymbol{ST}}{dt} = Plf(T,I,S,F)\cdot(1-Fam)\cdot FPst\cdot LF - MTst(T)\cdot BMst(T)\cdot \boldsymbol{ST} \tag{4-2}$$

$$\frac{d\,\boldsymbol{RT}}{dt} = Plf(T,I,S,F)\cdot(1-Fam)\cdot FPrt\cdot LF - BMrt(T)\cdot \boldsymbol{RT} \tag{4-3}$$

$$\boldsymbol{H} = \begin{cases} d\cdot(LF+ST)+e\,, & when\ (LF+ST)\le crit \\ a\cdot(LF+ST-crit)+d\cdot crit+e, & when\ (LF+ST)>crit \end{cases} \tag{4-4}$$

where $\boldsymbol{LF}$, $\boldsymbol{ST}$, and $\boldsymbol{RT}$ (g C m^{-2}) are biomasses of leaf, stem, and root of the marsh, respectively. Plf (day^{-1}) is the growth function of the leaf. This growth function is determined by temperature (T), light (I), salinity (S), and inundation stress (F). Fam is the fraction for active metabolism during photosynthesis. $FPlf$, $FPst$, and $FPrt$ are fractions of biomass transformations from leaf photosynthesis. $BMlf$, $BMst$, and $BMrt$ (day^{-1}) are basal metabolism rates of the leaf, stem, and root, respectively, which are functions of temperature. $MTlf$ and $MTst$ are seasonal mortalities of leaf and stem. $\boldsymbol{H}$ (m) is marsh canopy height, calculated from the above-ground biomass with the coefficients of $crit$, a, d, and e.

The growth rate of leaf Plf can be written as a product of temperature-driven maximum growth rate and three stress functions (salinity, light, and inundation):

$$Plf = Pm(T)\cdot f(S)\cdot f(I)\cdot f(F)/acdw \tag{4-5}$$

where Pm (g C g^{-1} DW day^{-1}) is the maximum growth rate, which is determined by the temperature. $f(S), f(I)$, and $f(F)$ are the limitation functions of salinity, light, and inundation stress, respectively. $acdw$ (g C g^{-1} DW) is the plant carbon to dry-weight ratio.

The maximum growth rate Pm is expressed as:

$$Pm(T) = pmbs \cdot e^{-KTg1 \cdot (T-Topt)^2}, when\ T \leq Topt \tag{4-6}$$

$$Pm(T) = pmbs \cdot e^{-KTg2 \cdot (T-Topt)^2}, when\ T > Topt \tag{4-7}$$

where $pmbs$ (g C g^{-1} DW day^{-1}) is the coefficient for the maximum growth rate function. $KTg1$ and $KTg2$ ($^oC^{-2}$) are the shape coefficients of temperature adjustment. T (^{o}C) is the local temperature and $Topt$ (^{o}C) is the optimal temperature for plant growth.

The limiting function of salinity $f(S)$ is expressed as:

$$f(S) = \frac{ST}{ST + (Salt - Saltopt)^2} \tag{4-8}$$

where ST is salinity stress coefficient (PSU^2), $Salt$ is water column salinity, and $Saltopt$ (PSU) is the optimal salinity for this species. The limitation function of inundation stress $f(F)$ is:

$$f(F) = \frac{rdephcan}{tinun + rdephcan} \tag{4-9}$$

$$rdephcan = \frac{\boldsymbol{H}}{tdep} \tag{4-10}$$

where $rdephcan$ is the ratio of canopy height to the total water column depth and $tdep$ (m) is the total water column depth. Parameter input $tinun$ is the inundation pressure coefficient. Once the ratio of canopy height to the total water column depth reach $tinun$, the inundation limitation is 0.5; and if the ratio further increases, there is less inundation stress (>0.5). The limiting functions of light $f(I)$ is:

$$f(I) = \frac{Iwc}{\sqrt{Iwc^2 + Ik^2}} \tag{4-11}$$

$$Ik = \frac{Pm(T)}{\alpha} \tag{4-12}$$

$$Iwc = \frac{Iatcnpy}{Ksh \cdot (LF+ST)} \cdot \left[1 - e^{-\left(Ksh \cdot (LF+ST)\right)}\right] \tag{4-13}$$

$$Iatcnpy = \begin{cases} Io \cdot e^{-Kw \cdot (tdep - H)}, & when\ H < tdep \\ Io, & when\ H \geq tdep \end{cases} \tag{4-14}$$

where Iwc (E m^{-2}) is irradiance utilized by plant growth, $Iatcnpy$ (E m^{-2}) is irradiance reaching canopy top, and Io (E m^{-2}) is irradiance reaching the water surface. Ik (E m^{-2}) is an adjusting function of leaf growth. Ksh (m^2 g^{-1}) is the leaf self-shading coefficient and Kw (m^{-1}) is the light attenuation coefficient.

The metabolism rates of the three tissues are functions of temperature:

$$BMlf = BMlfr \cdot e^{KTblf \cdot (T - Trlf)} \tag{4-15}$$

$$BMst = BMstr \cdot e^{KTbst \cdot (T - Trst)} \tag{4-16}$$

$$BMrt = BMrtr \cdot e^{KTbrt \cdot (T - Trrt)} \tag{4-17}$$

where $BMlf$, $BMst$, and $BMrt$ (day^{-1}) are basal metabolism rates of leaf, stem, and root, respectively. $BMlfr$, $BMstr$, and $BMrtr$ (day^{-1}) are basal metabolism rates of leaf, stem, and root, respectively, at reference temperatures $Trlf$, $Trst$, and $Trrt$ (°C). $KTblf$, $KTbst$, and $KTbrt$ (°C^{-1}) are the shape coefficients for the temperature functions of leaf, stem, and root, respectively.

A sigmoid function is used as the seasonal mortality coefficient to account for the natural decay of aboveground plants in the fall. These mortality coefficients are expressed as a function of temperature (Li et al., 2021):

$$MTlf = \frac{adlf}{1+e^{-bdlf\cdot(T-cdlf)-ddlf}} + 1 \quad (4\text{-}18)$$

$$MTst = \frac{adst}{1+e^{-bdst\cdot(T-cdst)-ddst}} + 1 \quad (4\text{-}19)$$

where $MTlf$ and $MTst$ are seasonal mortality coefficients of leaf and stem, respectively. The magnitude of $MTlf$ and $MTst$ are determined by the parameters $adlf$ and $adst$. The seasonal variability of $MTlf$ and $MTst$ is determined by $bdlf$, $cdlf$, $ddlf$, $bdst$, $cdst$, and $ddst$.

The growth of leaf takes up ammonia and phosphate from the sediment directly:

$$uptakeNH4 = -Anc \cdot Plf \cdot \boldsymbol{LF} \quad (4\text{-}20)$$

$$uptakePO4 = -Apc \cdot Plf \cdot \boldsymbol{LF} \quad (4\text{-}21)$$

where $uptakeNH4$ and $uptakePO4$ (g m^{-2} day^{-1}) are uptake of ammonia and phosphate from the sediment deeper layer to support plant growth, respectively. Anc (g N g^{-1} C) and Apc (g P g^{-1} C) are nitrogen and phosphorus to carbon ratios, respectively.

The metabolism of leaf and stem, mostly defoliation, settles organic matters to the bottom. In addition, the metabolism of the roots also releases particulate organic nutrients to the sediment. The PON and POP budget in the sediment is fueled by both sources and these sources are expressed as:

$$setPON = Anc \cdot [(Plf \cdot Fam + MTlf \cdot BMlf) \cdot \boldsymbol{LF} + MTst \cdot BMst \cdot \boldsymbol{ST} + BMrt \cdot \boldsymbol{RT}] \quad (4\text{-}22)$$

$$setPOP = Apc \cdot [(Plf \cdot Fam + MTlf \cdot BMlf) \cdot \boldsymbol{LF} + MTst \cdot BMst \cdot \boldsymbol{ST} + BMrt \cdot \boldsymbol{RT}] \quad (4\text{-}23)$$

$$\frac{dPON(1:3)}{dt} = setPON \cdot frnveg(1:3) \quad (4\text{-}24)$$

$$\frac{dPOP(1:3)}{dt} = setPOP \cdot frpveg(1:3) \quad (4\text{-}25)$$

where $setPON$ and $setPOP$ (g m^{-2} day^{-1}) are sources of particulate organic matter to the lower layer of the sediment, respectively. $frnveg$ and $frpveg$ are the fractions of these particulate nutrients going to three groups of labile, refractory, inert groups in the sediment budget of PON and POP. The dissolved organic nitrogen and phosphorus from hydrolysis in the pore water of the upper sediment layer is assumed to be relatively minor and neglected in this model.

When the plant is fully submerged, the production of oxygen by leaf photosynthesis is accounted as a source to the water column oxygen, but when the plant is above the water surface, we assume the oxygen produced by the marsh goes to the atmosphere directly. Once submerged, the contribution of the marsh is added as a source term to the water column DO in the vertical cells the marsh occupies:

$$\frac{dDO}{dt} = Aocr \cdot Plf \cdot \boldsymbol{LF/H} \tag{4-26}$$

where DO (g m^{-3}) is oxygen concentration in the vertical layers of the water column where marsh occupies and $Aocr$ (g O_2 g^{-1} C) is oxygen to carbon ratio. On the other hand, the defoliation settles onto the sediment, part of them is assumed to be hydrolyzed in the pore water of the upper sediment layer and consume the available oxygen diffused from the bottom layer of the water column. In addition, the metabolism of roots also consumes oxygen. Both processes contribute to the sediment oxygen demand:

$$sedDO = -Aocr \cdot \left\{FrtDO \cdot BMrt \cdot \boldsymbol{RT} + FDO \cdot \frac{DO_0}{khr+DO_0} \cdot [(Plf \cdot Fam + MTlf \cdot BMlf) \cdot \boldsymbol{LF} + MTst \cdot BMst \cdot \boldsymbol{ST}]\right\} \tag{4-27}$$

where $sedDO$ (g m^{-2} day^{-1}) is sediment oxygen demand driven by the marshes. $FrtDO$ is the fraction of DO consumption in root metabolism. FDO is the fraction of the organic carbon hydrolyzed in the pore water of the upper sediment layer. khr (g m^{-3}) is the coefficient of DOC

oxidation in the upper sediment layer. DO_0 (g m^{-3}) is oxygen concentration in the bottom layer of water column. The remaining DOC in the pore water diffused into the water column:

$$sedDOC = FDO \cdot \frac{khr}{khr+DO_0} \cdot [(Plf \cdot Fam + MTlf \cdot BMlf) \cdot \boldsymbol{LF} + MTst \cdot BMst \cdot \boldsymbol{ST}] \quad (4\text{-}28)$$

where $sedDOC$ (g m^{-2} day^{-1}) is the DOC flux from the upper sediment layer to the water column. The rest of the organic carbon goes into the lower sediment layer as particulate matter:

$$setPOC = (1 - FDO) \cdot [(Plf \cdot Fam + MTlf \cdot BMlf) \cdot \boldsymbol{LF} + MTst \cdot BMst \cdot \boldsymbol{ST}] + (1 - FrtDO) \cdot BMrt \cdot \boldsymbol{RT} \quad (4\text{-}29)$$

$$\frac{dPOC(1:3)}{dt} = setPOC \cdot frcveg(1:3) \quad (4\text{-}30)$$

where $setPOC$ (g m^{-2} day^{-1}) is a source of particulate organic carbon to the lower layer of the sediment. $frcveg(1:3)$ are the fractions of these particulate carbon going to three groups of labile, refractory, inert groups in the sediment budget of POC.

4.2.3 Model implementation and sensitivity tests

The marsh kinetic process that responds to the changes in environmental conditions is demonstrated in Fig. 4-3. Marsh reaches maximum growth when the temperature reaches the optimal value for this species (Fig. 4-3a). Higher radiation reaching the marsh canopy alleviates light limitation on marsh growth, while self-shading (included in the model) limits the growth if the marsh reaches a high biomass (Fig. 4-3b). The three groups of the marsh (salt marsh, brackish marsh, and freshwater marsh) have different optimal salinity for their growth. For example, the freshwater marsh receives no salinity stress on its growth when the local salinity is close to 0 PSU, so the value of f(S) is close to 1 (Fig. 4-3c). When the marsh is submerged, marsh growth decreases as inundation-depth increases; when the marsh emerges, the water depth

places a minor limitation on marsh growth (Fig. 4-3d). The parameter sets used in this study are listed in Table 1.

To investigate the role of marsh on the adjacent waterbody, we implemented the coupled hydrodynamic, water quality, and marsh model for the York River Estuary. The model grid generally follows the one used in the water quality study by Cai et al. (2020) with local refinements in the York River Estuary (Fig. 4-4). The grid covers the whole Bay to accurately simulate the exchanges between the York River and the Bay. This grid contains 47,477 nodes and 73,433 elements. Outside the Bay, the grid resolution varies from 2.4 km for the continental shelf to 550 m at the Bay mouth. Inside the York River estuary, the along-channel grid resolution increases from 300 m to 100 m from the mouth to the Pamunkey and Mattaponi Rivers. The cross-channel resolution increases from 200 m to less than 100 m upstream. The resolution is about 50 m in the area with extensive marshes (e.g., Sweet Hall Marsh). A hybrid shaved vertical grid system LSC^2 (Localized Sigma Coordinates with Shaved Cells) is applied in this domain. There are up to 52 vertical layers in the deeper ocean and at least one layer in the shallow regions nearshore.

The model simulation period is from 2010 to 2014 with a single non-split time step of 150 sec. The open boundary is forced by interpolated elevations from two tidal gauges at Lewes, DE and Beaufort, NC. The temperature at the ocean boundary is nudged to HYCOM. The salinity is relaxed near the ocean boundary toward the World Ocean Atlas monthly climatological data. Hydrologic and nutrient loadings are from the outputs from Phase 6 Watershed Model of the Chesapeake Bay Assessment Tool (CAST) (Shenk and Linker, 2013). The North American Regional Reanalysis provides the atmospheric forcing (Mesinger et al.,

2006). The model was spun up to equilibrate the water quality variables before simulating the target period of 2010 to 2014.

In addition to the calibrated setup (Base Scenario), we also conducted seven sensitivity tests to examine the responses of marsh and adjacent estuarine waters with different parameters or processes (Table 4-2). NV0 treats the marsh plants as plastic cylinders without any contributions to biochemical processes, i.e., they only affect the local physical environments; in doing so, we can isolate the ecological contributions from the tidal marshes to the entire system. Tests 2nd to 7th alter the parameters that are related to (1) marsh growth, (2) metabolism, and (3) uptake/release of nutrients, in the form of optimal temperature for marsh production ($Topt$), coefficients for maximum growth rate function ($Pmbs$), reference metabolism rates at reference temperatures ($bmlf$, $bmst$, and $bmrt$), and marsh nitrogen or phosphorus to carbon ratios (Anc and Apc), respectively. All the sensitivity tests use the identical physical setup as the Base Scenario.

4.2.4 Analysis methods

4.2.4.1 Model skill assessments

To assess the model skill, model simulations of various water quality state variables are compared with CBP observations in the York, Pamunkey, and Mattaponi Rivers. RMSE (root mean square error), CC (correlation coefficient), and RE (relative error) of model simulations against observations in both water surface and bottom are calculated to evaluate the model performance. In addition to the use of statistics, we also use times series comparisons at selected stations in Pamunkey River, West Point, and lower York River to assess the model skills. In addition, we compare the mean modeled tidal range along the York River channel against the

observations to ensure the tidal flooding in the marshes is correctly simulated in terms of frequency and duration. The mean tidal range is estimated as the differences between modeled high tide and low tide over a tidal cycle averaged over the entire simulation period (the model output frequency is every 30 min).

4.2.4.2 Marsh biomass and productivity

For the simulation of marsh biomass, due to the lack of continuous, in-situ measurement of tidal freshwater marsh biomass in the York River Estuary (e.g., Sweet Hall Marsh), we compared the modeled marsh biomass with a few historical observations (Perry and Hershner, 1999; Davies, 2004) as qualitative evaluation. Marsh net productivity is calculated by:

$$\mathrm{MPP} = \sum_{m=1,2,3}(Plf_m \cdot (1 - Fam_m) - MTlf_m \cdot BMlf_m) \cdot \boldsymbol{LF_m} - MTst_m \cdot BMst_m \cdot \boldsymbol{ST_m} - BMrt_m \cdot \boldsymbol{RT_m} \quad (4\text{-}31)$$

where m is the index of the three tidal marsh groups (salt marsh, brackish marsh, and freshwater marsh).

4.2.4.3 Phytoplankton production

Local phytoplankton production in each grid cell is computed by integrating the local phytoplankton production in the water column:

$$\mathrm{GPP} = \sum_{i=1}^{n}(\mathrm{C1}_i \cdot \mathrm{G1}_i + \mathrm{C2}_i \cdot \mathrm{G2}_i + \mathrm{C3}_i \cdot \mathrm{G3}_i) \cdot \mathrm{dep}_i \quad (4\text{-}32)$$

where GPP is areal gross primary production of phytoplankton (g C m^{-2} day^{-1}), n is the number of vertical layers in each element, i is the vertical layer index, $\mathrm{C1}, \mathrm{C2}, \mathrm{C3}$ are carbon-based phytoplankton biomass of three groups (diatoms, green algae, and cyanobacteria) over each layer, respectively (g C m^{-3}), $\mathrm{G1}, \mathrm{G2}, \mathrm{G3}$ are growth rates of the three phytoplankton groups (day^{-}

^{1}), respectively, and dep is layer thickness (m). The calculated spatially varying GPP is averaged with the weight of element area for the entire York River Estuary in each scenario and sensitivity test.

4.2.4.4 Material fluxes

Annual-averaged net material fluxes were calculated along the 11 transects from the upstream to the downstream to study the role of the marshes (Fig. 4-1bc). Net fluxes of dissolved organic carbon (DOC) and inorganic nutrients (DIN and PO_4^{3-}) were analyzed in the Base Scenario and all the sensitivity tests. The net flux is the result of outflux (marked as positive) minus influx (marked as negative), both of which are calculated as the sectionally integrated product of the flow velocity normal to the transect and the concentrations of materials:

$$\text{net flux} = \text{outflux} - \text{influx} = \int_{\text{A}} (u_n \cdot \text{Var})\text{dA} \tag{4-33}$$

where u_n is the normal velocity (m s^{-1}), Var is the concentration of DOC or other nutrients, A is the vertical area of the transect (m^2).

4.3 Model assessments

4.3.1 Physical environments

CBP and VECOS stations along the channel of the York River are used to evaluate the model skills of salinity (Fig. 4-5). In Fig. 4-5a, the four-year averaged observed salinities are represented by colored circles with light grey crosses inside. The model skill of mean salinity is satisfactory as evidenced by the fact that most of the circles completely disappear into the background. The model captures the saltwater intrusion events well in terms of occurrence,

duration, and salinity magnitude (Fig. 4-5b). The error in salinity is less than 0.8 PSU at Station TF4.2 (White House). In addition, the model captures well the stratification in the lower York River (Fig. 4-5f-h).

In the York River Estuary, the high-frequency data of total water depth at two VECOS stations and the historic tidal range from the NOAA tides tables are used to evaluate the model skills for tidal range (Fig. 4-6). The modeled tidal range agrees with the historic observations along the York River and captures its along-channel variability (Fig. 4-6a). The model tends to over-estimate the tidal range at the York River mouth while under-estimate at the upper end of the Pamunkey and Mattaponi. The largest difference of the tidal range is 7.98 cm at the station of Northbury, in the Pamunkey River. Considering the historical data were measured a long time ago and changes in bathymetry in the York River can be expected. Harmonic analysis shows that the major constituents are well modeled in terms of phases and amplitudes (Fig. 4-6bc). The model results slightly over-estimate the M2 amplitudes by 1.36 cm at Station Sweet Hall and 2.31 cm at Station White House. Overall, the model performance on tidal simulation is satisfactory.

4.3.2 Water quality simulations

Overall, the model captures the seasonal cycles and interannual variability of chlorophyll-a, DO, DIN, and PO_4^{3-} (Fig. 4-7). Model skill statistics for these variables are presented in Table 4-3 and summarized in target diagrams (Fig. 4-7de). The model successfully simulates the chlorophyll-a concentrations in the Pamunkey and York River, but the model slightly under-predicted the peak chlorophyll-a concentrations at West Point. DO is reasonably predicted with high CC (larger than 0.82), small RE (mostly less than 25%), and low normalized RMSE for all

the York stations (Table 4-3). The simulated DIN generally follows the observed pattern of high spring concentrations and low summer/fall concentrations, although it is underestimated by the model sometimes in the fall. Phosphate is also well simulated by this model and shows the typical seasonal pattern that the concentration is low in spring and high in summer and fall.

4.3.3 Tidal marshes

Overall, the model results of marsh biomass and productivity show a qualitatively reasonable seasonal pattern (Fig. 4-8a-c). The high biomass is around 600 g C m^{-2}, which is in the same range as the measured range from 490 to 800 g C m^{-2} (Perry and Hershner, 1999; Davies 2004). In Sweet Hall Marsh, marsh biomass tends to be relatively low at marsh edges where the inundation stress is high and tends to increase towards landward locations where the inundation stress is reduced (Fig. 4-8d). The group of freshwater marsh, which prefers low salinity, has lower biomass towards the West Point where higher salinity occurs (Fig. 4-8c), which is generally consistent with the spatial pattern of the observed local community structure (Mitchell et al., 2017).

We also tested the responses of marsh biomass to different parameter sets (Fig. 4-9). Because marsh growth mainly depends on light and temperature, while salinity and tidal range do not change much in the sensitivity tests, the simulated marsh biomass is mainly sensitive to model kinetic parameters (e.g., $Topt$, $Pmbs$, $bmlf$, $bmst$, and $bmrt$). An increase of 50% on both growth rate and metabolism rate causes a 29.52% reduction in the mean biomass, while a 25% decrease of the two rates increases the mean biomass by 24.97%. An increase or decrease of 5 ^{o}C in the optimal temperature of the leaf growth decreases or increases the mean biomass by

6.26% and 3.55%, respectively. On the other hand, changes of carbon to nitrogen or phosphorus ratio (Anc and Apc) have little impact on the marsh biomass (e.g., variations are <0.24%).

4.4 Discussion

4.4.1 Impacts of marsh on oxygen dynamics and organic carbon

DO under saturation level has been observed in the water body adjacent to the marshes. In the Pamunkey River, the loss of DO due to marsh is estimated to be about 1.12 to 2.77 g m^{-2} day^{-1} (Cerco and Noel, 2019). To test the effects of marsh on DO, we compared model simulations of the Base Scenario (with marsh) and NV0 (without marsh). If the marshes are biologically deactivated, the spatial pattern of the annually averaged bottom DO in NV0 (red line in Fig. 4-10b) is closer to saturation for the shallow water of the upstream as expected. However, the Base Scenario (blue line in Fig. 4-10b) shows that the existence of a highly productive marsh, which drives more heterotrophic respiration, tends to decrease the bottom oxygen concentrations along with a higher level of DOC in the system (Fig. 4-10bc). Compared with NV0, the existence of the marshes not only lowers the overall bottom DO level but also enhances the diurnal swing of DO adjacent to the marshes (Fig. 4-11b). During low tide, the DO concentration sometimes drops to below 2 g m^{-3}, accompanied by the export of high DOC and oxygen demand (e.g., sulfide) from the anaerobic marsh sediments (Fig. 4-11ab-3).

The highly productive marshes tend to be significant sources of organic carbon to the York River Estuary. Marshes were added in the model from Horseshoe in upstream Pamunkey River to the West Point; marshes generally contribute to about 60-70% of the annual net flux of DOC at the West Point (Fig. 4-12a). As a result, the overall DOC concentration decreases significantly in the York River Estuary in the sensitivity test NV0, especially in the Pamunkey

River (about 80%) where extensive marshes exist (Fig. 4-10c). In other sensitivity tests, the changes in both the DOC concentration and DOC net fluxes are relatively minor (Fig. 4-13a for the net fluxes at West Point, fluxes at other interfaces, and concentrations are not shown). The major reason for the minor changes in the marsh biomass is that marsh biomass does not change much in these sensitivity tests except for GM1 and GM2 (Fig. 4-9). For example, in NP1, and NP2, the marsh biomass changes by less than 0.24%, and the DOC net fluxes change by less than 0.4%. Although marsh biomass changes up to about 30% in GM1 and GM2, the changes in net DOC outfluxes are less than 4% due to a compensating effect from carbon settling and release in the lower layer. Compared with NV0, the surface chlorophyll-a concentration is also higher in the Base Scenario because of marsh presence. Although the higher chlorophyll-a concentration ($< 2\ \mu g\ L^{-1}$) also contributes to the higher level of DOC ($< 0.12\ g\ m^{-3}$), this contribution is much less than the change in DOC (about $3\ g\ m^{-3}$; Fig. 4-10c). Thus, the model suggests that the dominant contributor to DOC changes is not phytoplankton but tidal marshes. Qin and Shen (2019) show that ecosystem gross primary production (GPP) is several times larger than the pelagic GPP in the Pamunkey River, suggesting a high contribution from the tidal marshes, which is consistent with this model estimations. There are limited observations of DOC concentrations available, and synthesis of observed DOC fluxes on an estuary scale is still lacking. According to the limited DOC observations in the York River Estuary, the DOC concentrations range from 3 to $6\ g\ m^{-3}$, which agrees with our model results. However, different directions of DOC fluxes between the marshes and the adjacent water in the York River marshes have been observed at different sites and times (Czapla et al., 2020; Neubauer and Anderson 2003; Bukaveckas 2021). These observations suggest that marshes may either be a source or a sink to DOC on the local scale.

In addition, this model performs well in the calibration against DO measurement in the adjacent channel, suggesting the model functions correctly to simulate the low DO. Our model configuration suggests that a large portion of DO is consumed by the DOC in the wetland. This is consistent with existing marsh models in the literature that simply adds a DO sink term for considering marsh respiration and assigns the respiration rate with observed values in the Pamunkey River and other marshes (Cerco and Noel, 2019).

4.4.2 Impacts of marsh on nitrogen and phosphorus

Overall, tidal marshes tend to be a modifier of the nutrients (Fig. 4-10d-f). In this modeling study, the marsh functions as a sink of nutrients directly through settling organics from fallen leaves or other tissues and particulates transported to the marshes. The sediment mineralization processes can enhance denitrification to release nitrogen gas. Given the larger form drag from the marsh plants, tidal marshes trap the particulate nutrients quickly and trap them into the sediment layer. This helps to reduce nutrient loading into the open water. However, diel DO variations occur in the tidal marshes and adjacent channels. The low-DO events in these diel cycles enhance bottom phosphate release. For example, when bottom DO concentration drops below 2 g m^{-3} at low tide (Fig. 4-11b), a pulse of the bottom release of phosphate occurs (Fig. 4-11d), which largely increases the phosphate concentration (Fig. 4-11c). As a result, the phosphate concentration is lower in the sensitivity test NV0 than the Base Scenario (Fig. 4-10d) and the net phosphate flux from the upstream decreases significantly in NV0 (Fig. 4-12c). On the other hand, the diel bottom DO in the Base Scenarios prompts more denitrification, while there is more DIN retained in the system in the sensitivity test NV0 (Fig. 4-10ef). The existence of marsh

helps to reduce the net DIN fluxes into the York River at the West Point by about 10% (Fig. 4-12b).

Changes in marsh growth rate, metabolism rate, and optimal growth temperature have little impact on the net fluxes of inorganic nutrients from the upstream to the lower stream at the West Point (e.g., < 6%, Fig. 4-13bc-2). Increasing the carbon to nitrogen or phosphorus ratio by 100% decreases the DIN fluxes by 0.6% and the PO_4^{3-} fluxes by 27.2%, respectively. On the other hand, decreasing these ratios by 50% decreases the flux of PO_4^{3-} by 5.4%. The change of PO_4^{3-} and DIN outfluxes are generally proportional to each other with a significant negative linear regression relationship (Fig. 4-10e). For example, in the sensitivity tests such as GM1, the change of DIN outfluxes is negative while the changes of TOC and PO_4^{3-} fluxes are positive because the lower DO along with higher DOC prompts more denitrification to remove DIN from the system.

4.4.3 Impacts of marsh on chlorophyll-a and phytoplankton productions

The impacts of tidal marshes on the ecosystem, including the phytoplankton dynamics, are a combination of physical and biological impacts. The existence of marsh takes up space and adds the form drag in the system, so if the tidal marshes were physically removed, the dynamic environment would be drastically altered. In this study, the physical functions of tidal marshes are kept identical, and only biological impacts of marshes are investigated from the scenarios and sensitivity tests. The major biological impact from the marsh to the adjacent water is on nutrient availability. The chlorophyll-a in the upstream above the West Point tends to slightly decrease in the sensitivity test NV0 compared to the Base Scenario (Fig. 4-10a). Along with the decreased chlorophyll-a in NV0, phytoplankton production (PP) in the York River Estuary decreases by

2.4% (Fig. 4-13d). Change of the PP is positively correlated to the changes of PO_4^{3-} net fluxes from the upstream through the West Point (Fig. 4-13g). Although the change of PP has a significant linear relationship with the change of DIN, the correlation is negative (Fig. 4-13f). Therefore, PP is more limited by the availability of phosphate than DIN. However, the change of PP (2.4%) is much smaller in magnitude than the change of phosphate (67.9%), because the phytoplankton dynamic in the York River Estuary is mostly dominated by flushing and light limitations (Sin et al., 1999).

4.4.4 Uncertainties, limitations and future study

In this study, we focused on the development and implementation of a new marsh model. This marsh model is embedded into a 3D hydrodynamic water quality model and used to simulate the impacts of the marsh on estuarine biochemical processes in the York River Estuary. This model is developed based on current understanding and available data with a few assumptions. For example, low-DO events are observed with the existence of tidal marshes, but the mechanism is not fully understood. The low-DO events may be caused by the increased heterotrophic respiration which is driven by the DOC fluxes from the marshes. Or the low-DO events may be caused by the oxygen demand from the sediment of the tidal marshes (e.g., diffused sulfide). The material that is exported from the tidal marshes has been observed to be dominated by organic carbon or inorganic carbon at different times or locations (Czapla et al., 2020; Chen et al., 2022). Currently, the marsh model in this study allows both the export of organic carbon and the low sediment redox potentials that requires oxygen demand to fit the observations. However, there might be certain knowledge gaps and a lack of sufficient observations in the marsh-relevant processes that need to be further explored. In addition, a few

simplifications were applied to the model implementations. For example, we did not include the simulations of the submerged aquatic vegetations (SAV) in this study because of its much smaller footprints than the tidal marshes in this system, especially in the upstream (Moore, 2009). Also, the uncertainty of the bathymetry data confounds the habitats of tidal marshes or SAV. In addition, this model does not include the small sub-tributaries of the York River Estuary, thus missing about 35% of the tidal marshes in the whole York River watershed, most of which are embayed in the sub-tributaries that requires to be highly resolved and requires more computational resource. Due to the lack of observational data on marsh biomass and other fluxes between different interfaces, our model might need further calibration even though the results are sensible. Sedimentation and the evolution of marsh platforms were not included because of the relatively short (seasonal and annual) time scale, but its effect on biochemical processes can be distinct at a longer time scale. Overall, our study here provides a successful implementation of the marsh model to study the role of tidal marshes on the estuarine biochemical processes.

4.5 Summary and conclusion

We developed a new marsh model inside the framework of a 3D unstructured-grid hydrodynamic water quality model (SCHISM-ICM-Marsh) to study the roles of tidal marshes on the estuarine biochemical processes in the York River Estuary. This model showed a good performance in simulating the physiological processes of tidal marshes, the wetting-drying physical processes, and the interplay among water quality properties such as chlorophyll-a, DO, and other nutrients. The model results demonstrated that the tidal marshes drive the local diurnal swings of water column oxygen by exporting dissolved organic carbon that drives the oxygen demand with the tidal flow. The oxygen concentration temporarily dropped below hypoxia in

summer on a daily scale. High transport of organic matter from the tidal marshes enhanced the heterotrophic respiration in the estuary. In addition, tidal marshes tended to be a modifier of the nutrients. Tidal marshes played an important role in the settling of particulate matter. The low-DO events in the tidal marshes and adjacent channel further increased the bottom phosphate release and denitrification, which enhanced phosphorus releases from the sediment but increased the removal of nitrogen from the system. In addition, estuarine phytoplankton production and other biochemical processes were also impacted by the tidal marshes, but phytoplankton production is mainly limited by transport processes and light. Overall, the upstream marshes were found to exert a substantial influence on biochemical processes in the estuary.

Literature Cited

Alizad, K., Hagen, S.C., Morris, J.T., Bacopoulos, P., Bilskie, M.V., Weishampel, J.F. and Medeiros, S.C., 2016. A coupled, two-dimensional hydrodynamic-marsh model with biological feedback. *Ecological Modelling*, *327*, pp.29-43.

Alongi, D.M., 2020. Coastal ecosystem processes. CRC press.

Anderson, I.C., Tobias, C.R., Neikirk, B.B. and Wetzel, R.L., 1997. Development of a process-based nitrogen mass balance model for a Virginia (USA) Spartina alterniflora salt marsh: implications for net DIN flux. *Marine Ecology Progress Series*, *159*, pp.13-27.

Axelrad, D.M., Moore, K.A. and Bender, M.E., 1976. Nitrogen phosphorus and carbon flux in Chesapeake Bay marshes.

Bowden, W.B., Vörösmarty, C.J., Morris, J.T., Peterson, B.J., Hobbie, J.E., Steudler, P.A. and Moore III, B., 1991. Transport and processing of nitrogen in a tidal freshwater wetland. *Water Resources Research*, 27(3), pp.389-408.

Bridgham, S.D., Megonigal, J.P., Keller, J.K., Bliss, N.B. and Trettin, C., 2006. The carbon balance of North American wetlands. *Wetlands*, 26(4), pp.889-916.

Brooks, T.J., 1983. Pamunkey River slack water data report: temperature, salinity, dissolved oxygen, 1970-1980.

Bukaveckas, P., 2021. Carbon dynamics at the river-estuarine transition: a comparison among tributaries of Chesapeake Bay. *Biogeosciences Discussions*, pp.1-42.

Buzzelli, C.P., Wetzel, R.L. and Meyers, M.B., 1999. A linked physical and biological framework to assess biogeochemical dynamics in a shallow estuarine ecosystem. *Estuarine, Coastal and Shelf Science*, 49(6), pp.829-851.

Cai, X., 2018. Impact of submerged aquatic vegetation on water quality in cache slough complex, Sacramento-San Joaquin delta: a numerical modeling study.

Cai, X., Zhang, Y.J., Shen, J., Wang, H., Wang, Z., Qin, Q. and Ye, F., 2020. A numerical study of hypoxia in Chesapeake Bay using an unstructured grid model: Validation and sensitivity to bathymetry representation. *JAWRA Journal of the American Water Resources Association*.

Cerco, C.F. and Cole, T.M., 1994. Three-dimensional eutrophication model of Chesapeake Bay. Volume 1: Main report. Final report (No. AD-A-280760/0/XAB; WES/TR/EL-94-4). *Army Engineer Waterways Experiment Station*, Vicksburg, MS (United States). Environmental Lab.

Cerco, C.F. and Moore, K., 2001. System-wide submerged aquatic vegetation model for Chesapeake Bay. *Estuaries*, *24*(4), pp.522-534.

Cerco, C. and Noel, M., 2017. The 2017 Chesapeake Bay water quality and sediment transport model. *US Army Engineer Waterways Experiment Station*, Vicksburg MS. https://www. chesapeakebay. net/documents/2017_WQSTM_Documentation_DRAFT_5-10-17. pd*f*.

Cerco, C.F. and Seitzinger, S.P., 1997. Measured and modeled effects of benthic algae on eutrophication in Indian River-Rehoboth Bay, Delaware. *Estuaries*, *20*(1), pp.231-248.

Cerco, C.F. and Tian, R., 2021. Impact of Wetlands Loss and Migration, Induced by Climate Change, on Chesapeake Bay DO Standards. *JAWRA Journal of the American Water Resources Association*.

Chambers, R.M., Harvey, J.W. and Odum, W.E., 1992. Ammonium and phosphate dynamics in a Virginia salt marsh. *Estuaries*, 15(3), pp.349-359.

Chen, X., Santos, I.R., Hu, D., Zhan, L., Zhang, Y., Zhao, Z., Hu, S. and Li, L., 2022. Pore-water exchange flushes blue carbon from intertidal saltmarsh sediments into the sea. *Limnology and Oceanography Letters*.

Chmura, G.L., Anisfeld, S.C., Cahoon, D.R. and Lynch, J.C., 2003. Global carbon sequestration in tidal, saline wetland soils. *Global biogeochemical cycles*, 17(4).

Davies, S.B., 2004. Vegetation dynamics of a tidal freshwater marsh: Long-term and inter-annual variability and their relationship to salinity.

Czapla, K.M., Anderson, I.C. and Currin, C.A., 2020. Net ecosystem carbon balance in a North Carolina, USA, salt marsh. *Journal of Geophysical Research: Biogeosciences*, *125*(10), p.e2019JG005509.

Diaz, R.J. and Rosenberg, R., 2001. Overview of anthropogenically-induced hypoxic effects on marine benthic fauna. *Coastal hypoxia: consequences for living resources and ecosystems*, *58*, pp.129-145.

Fagherazzi, S., Kirwan, M.L., Mudd, S.M., Guntenspergen, G.R., Temmerman, S., D'Alpaos, A., Van De Koppel, J., Rybczyk, J.M., Reyes, E., Craft, C. and Clough, J., 2012. Numerical models of salt marsh evolution: Ecological, geomorphic, and climatic factors. *Reviews of Geophysics*, 50(1).

Fagherazzi, S., Marani, M. and Blum, L.K., 2004. The ecogeomorphology of tidal marshes. American Geophysical Union.

Friedrichs, C.T., 2009. York River physical oceanography and sediment transport. *Journal of Coastal Research*, 2009(10057), pp.17-22.

Grant, R.R. and Patrick, R., 1970. Tinicum Marsh as a water purifier. Two Studies of Tinicum Marsh. The Conservation Foundation, Washington, DC, pp.105-123.

Janousek, C.N. and Mayo, C., 2013. Plant responses to increased inundation and salt exposure: interactive effects on tidal marsh productivity. *Plant ecology*, *214*(7), pp.917-928.

Jordan, T.E., Correll, D.L. and Whigham, D.F., 1983. Nutrient flux in the Rhode River: tidal exchange of nutrients by brackish marshes. *Estuarine, Coastal and Shelf Science*, 17(6), pp.651-667.

Kirwan, M.L. and Murray, A.B., 2007. An integrated biologic and physical model of tidal marsh evolution. *In Proceedings of the National Academy of Science* (Vol. 104, pp. 6118-6122).

Lai, D.Y.F. and Lam, K.C., 2008. Phosphorus retention and release by sediments in the eutrophic Mai Po Marshes, Hong Kong. *Marine Pollution Bulletin*, 57(6-12), pp.349-356.

Levin, L.A., Ekau, W., Gooday, A.J., Jorissen, F., Middelburg, J.J., Naqvi, S.W.A., Neira, C., Rabalais, N.N. and Zhang, J., 2009. Effects of natural and human-induced hypoxia on coastal benthos. *Biogeosciences*, *6*(10), pp.2063-2098.

Li, Y., Yuan, L., Cao, H.B., Tang, C.D., Wang, X.Y., Tian, B., Dou, S.T., Zhang, L.Q. and Shen, J., 2021. A dynamic biomass model of emergent aquatic vegetation under different water levels and salinity. *Ecological Modelling*, 440, p.109398.

Marani, M., D'Alpaos, A., Lanzoni, S., Carniello, L. and Rinaldo, A., 2007. Biologically-controlled multiple equilibria of tidal landforms and the fate of the Venice lagoon. *Geophysical Research Letters*, 34(11).

McHugh, J.M. and Dighton, J., 2004. Influence of mycorrhizal inoculation, inundation period, salinity, and phosphorus availability on the growth of two salt marsh grasses, Spartina

alterniflora Lois. and Spartina cynosuroides (L.) Roth., in nursery systems. *Restoration Ecology*, *12*(4), pp.533-545.

Mesinger, F., DiMego, G., Kalnay, E., Mitchell, K., Shafran, P.C., Ebisuzaki, W., Jović, D., Woollen, J., Rogers, E., Berbery, E.H. and Ek, M.B., 2006. North American regional reanalysis. *Bulletin of the American Meteorological Society*, *87*(3), pp.343-360.

Mitchell, M., Herman, J., Bilkovic, D.M. and Hershner, C., 2017. Marsh persistence under sea-level rise is controlled by multiple, geologically variable stressors. *Ecosystem Health and Sustainability*, 3(10), p.1379888.

Moore, K.A., 2009. Submerged aquatic vegetation of the York River. *Journal of Coastal Research*, (10057), pp.50-58.

Morris, J.T., Sundareshwar, P.V., Nietch, C.T., Kjerfve, B. and Cahoon, D.R., 2002. Responses of coastal wetlands to rising sea level. *Ecology*, 83(10), pp.2869-2877.

Neubauer, S.C. and Anderson, I.C., 2003. Transport of dissolved inorganic carbon from a tidal freshwater marsh to the York River estuary. *Limnology and Oceanography*, *48*(1), pp.299-307.

Neubauer, S.C., Miller, W.D. and Anderson, I.C., 2000. Carbon cycling in a tidal freshwater marsh ecosystem: a carbon gas flux study. *Marine Ecology Progress Series*, 199, pp.13-30.

Odum, W.E., Smith III, T.J., Hoover, J.K. and McIvor, C.C., 1984. The ecology of tidal freshwater marshes of the United States east coast: a community profile. US Fish Wildl. Serv. FWS/OBS-83/17.

Qin, Q. and Shen, J., 2019. Pelagic contribution to gross primary production dynamics in shallow areas of York River, VA, USA. *Limnology and Oceanography*, *64*(4), pp.1484-1499.

Perry III, J.E., 1991. Analysis of vegetation patterns in a tidal freshwater marsh.

Perry, J.E. and Hershner, C.H., 1999. Temporal changes in the vegetation pattern in a tidal freshwater marsh. *Wetlands*, 19(1), pp.90-99.

Ridd, P., Sandstrom, M.W. and Wolanski, E., 1988. Outwelling from tropical tidal salt flats. *Estuarine, Coastal and Shelf Science*, 26(3), pp.243-253.

Shen, J. and Haas, L., 2004. Calculating age and residence time in the tidal York River using three-dimensional model experiments. *Estuarine, Coastal and Shelf Science*, *61*(3), pp.449-461.

Shenk, G.W. and Linker, L.C., 2013. Development and application of the 2010 Chesapeake Bay watershed total maximum daily load model. *JAWRA Journal of the American Water Resources Association*, 49(5), pp.1042-1056.

Sin, Y., Wetzel, R.L. and Anderson, I.C., 1999. Spatial and temporal characteristics of nutrient and phytoplankton dynamics in the York River estuary, Virginia: analyses of long-term data. *Estuaries*, *22*(2), pp.260-275.

Swarth, C. and Peters, D., 1993. *Water Quality & Nutrient Dynamics of Jug Bay on the Patuxent River, 1987-1992*. Anne Arundel County, Department of Recreation and Parks, Jug Bay Wetlands Sanctuary.

Sundareshwar, P.V., Morris, J.T., Koepfler, E.K. and Fornwalt, B., 2003. Phosphorus limitation of coastal ecosystem processes. *Science*, 299(5606), pp.563-565.

Townend, I., Fletcher, C., Knappen, M. and Rossington, K., 2011. A review of salt marsh dynamics. *Water and Environment Journal*, 25(4), pp.477-488.

Tzortziou, M., Neale, P.J., Megonigal, J.P., Pow, C.L. and Butterworth, M., 2011. Spatial gradients in dissolved carbon due to tidal marsh outwelling into a Chesapeake Bay estuary. *Marine Ecology Progress Series*, *426*, pp.41-56.

Watson, E.B., Andrews, H.M., Fischer, A., Cencer, M., Coiro, L., Kelley, S. and Wigand, C., 2015. Growth and photosynthesis responses of two co-occurring marsh grasses to inundation and varied nutrients. *Botany*, *93*(10), pp.671-683.

Wolanski, E., Chicharo, L. and Chicharo, M.A., 2008. Estuarine ecohydrology. *Encyclopedia of Ecology*, 2, pp.1413-1422.

Zhang, Y.J., Ye, F., Stanev, E.V. and Grashorn, S., 2016. Seamless cross-scale modeling with SCHISM. *Ocean Modelling*, 102, pp.64-81.

Zhang, Y.J., Gerdts, N., Ateljevich, E. and Nam, K., 2020. Simulating vegetation effects on flows in 3D using an unstructured grid model: model development and validation. *Ocean Dynamics*, 70(2), pp.213-230.

Ziegler, S., Velinsky, D.J., Swarth, C.W. and Fogel, M.L., 1999. Sediment-water exchange of dissolved inorganic nitrogen in a freshwater tidal wetland. Technical report of the Jug Bay Wetlands Sanctuary. Anne Arundel County Parks, Lothian, Maryland.

Tables for Chapter 4

Table 4-1: Key parameters of the marsh module

Parameter	Definition	Value	Unit
Fam	fraction of production devoted to active metabolism	0.2	$[-]$
$FPlf$	fraction of production routed to leaf biomass	0.6	$[-]$
$FPst$	fraction of production routed to stem biomass	0.3	$[-]$
$FPrt$	fraction of production routed to root biomass	0.1	$[-]$
a	coefficients to transfer marsh biomass to canopy height	-0.0002	$m^3\ g^{-1}$
d	coefficients to transfer marsh biomass to canopy height	0.0036	$m^3\ g^{-1}$
e	coefficients to transfer marsh biomass to canopy height	0.054	m
$crit$	coefficients to transfer marsh biomass to canopy height	300	$g\ m^{-2}$
$Acdw$	plant carbon-to-dry-weight ratio	0.38	$g\ C\ g^{-1}\ DW$
$Pmbs$	coefficient for maximum growth rate function	0.4	$g\ C\ g^{-1}\ DW\ day^{-1}$
$Topt$	optimal temperature for marsh production	27	℃
$KTg1$	effect of temperature below $Topt$ on production	0.003	$℃^{-2}$
$KTg2$	effect of temperature above $Topt$ on production	0.005	$℃^{-2}$
ST	salinity choice and stress coefficient	35	PSU^2
$Saltopt$	optimal salinity of this species	20, 12, 0	PSU
$tinun$	inundation pressure coefficient	0.2	$[-]$
α	initial slope of production versus irradiance curve	0.005	$g\ C\ g^{-1}\ DW \cdot (E\ m^{-2})^{-1}$
Ksh	light attenuation by marsh	0.045	$m^2\ g^{-1}\ C$
$bmlf$	reference metabolism rate of leaf at reference temperature	0.01	day^{-1}
$bmst$	reference metabolism rate of stem at reference temperature	0.01	day^{-1}
$bmrt$	reference metabolism rate of root at reference temperature	0.01	day^{-1}
Tr	reference temperature for leaf, stem, and root metabolism	20	℃
KTb	effect of temperature on leaf, stem, and root metabolism	0.08	$℃^{-1}$
ad	coefficients to calculate the seasonal mortality of leaf and stem	4	$[-]$
bd	coefficients to calculate the seasonal mortality of leaf and stem	-4	$℃^{-1}$
cd	coefficients to calculate the seasonal mortality of leaf and stem	17	℃
dd	coefficients to calculate the seasonal mortality of leaf and stem	12.8	$[-]$
Anc	marsh nitrogen to carbon ratio	0.01	$g\ N\ g^{-1}\ C$
Apc	marsh phosphorus to carbon ratio	0.003	$g\ P\ g^{-1}\ C$
$Aocr$	mass ratio of oxygen to carbon produced in photosynthesis	2.67	$g\ DO\ g^{-1}\ C$
FDO	fraction of leaf and stem hydrolyzed in the upper layer of the sediment	0.3	$[-]$
$FrtDO$	fraction of root metabolism as oxygen consumption	0.8	$[-]$
krh	coefficient of DOC oxidation in the upper sediment layer	1	$g\ m^{-3}$

Table 4-2: List of the sensitivity tests.

Sensitivity test abbreviation	Sensitivity test name	Changed parameters
NV0	Marsh biological functions disabled (i.e., with only physical effects)	
GM1	High growth rate and metabolism rate	$Pmbs = 0.6$ g C g^{-1} DW day^{-1} $bmlf = bmst = bmrt = 0.015$ day^{-1}
GM2	Low growth rate and metabolism rate	$Pmbs = 0.3$ g C g^{-1} DW day^{-1} $bmlf = bmst = bmrt = 0.0075$ day^{-1}
TG1	High optimal temperature for leaf growth	$Topt = 32$ ℃
TG2	Low optimal temperature for leaf growth	$Topt = 22$ ℃
NP1	High nitrogen/phosphorus-to-carbon ratio	$Anc = 0.02$; $Apc = 0.006$
NP2	Low nitrogen/phosphorus-to-carbon ratio	$Anc = 0.005$; $Apc = 0.0015$

Table 4-3: Skill assessment (RMSE, correlation coefficient (CC), and relative error (RE)) for model-data comparisons of certain water quality station variables from 2010 to 2014. Model outputs are interpolated onto the corresponding observation times (insufficient number of observations is denoted by "/").

Region	Station	Index	Layer	Chl-a	DO	DIN	PO_4^{3+}
Pamunkey	TF4.2	RMSE	S	7.79	2.43	0.14	0.03
	TF4.2	RMSE	B	/	2.52	0.14	0.02
	TF4.2	CC	S	0.24	0.85	0.76	-0.31
	TF4.2	CC	B	/	0.84	0.74	-0.30
	TF4.2	RE (%)	S	4.42	3.66	17.78	39.35
	TF4.2	RE (%)	B	/	7.78	18.37	45.49
	RET4.1	RMSE	S	7.71	1.48	0.14	0.04
	RET4.1	RMSE	B	/	1.61	0.14	0.04
	RET4.1	CC	S	0.20	0.94	0.61	0.35
	RET4.1	CC	B	/	0.93	0.62	0.38
	RET4.1	RE (%)	S	23.64	14.58	43.06	53.00
	RET4.1	RE (%)	B	/	16.31	45.21	51.60
Mattaponi	TF4.4	RMSE	S	5.01	3.20	0.14	0.05
	TF4.4	RMSE	B	/	3.28	0.13	0.04
	TF4.4	CC	S	0.21	0.82	0.35	0.12
	TF4.4	CC	B	/	0.82	0.35	0.12
	TF4.4	RE (%)	S	52.56	17.95	7.05	21.16
	TF4.4	RE (%)	B	/	21.41	1.56	28.08
	RET4.2	RMSE	S	7.83	1.72	0.12	0.03
	RET4.2	RMSE	B	/	1.60	0.12	0.03
	RET4.2	CC	S	0.23	0.89	0.63	0.54
	RET4.2	CC	B	/	0.89	0.56	0.51
	RET4.2	RE (%)	S	19.33	1.35	16.42	33.69
	RET4.2	RE (%)	B	/	1.32	19.27	35.42
York	RET4.3	RMSE	S	25.12	1.87	0.11	0.03
	RET4.3	RMSE	B	/	2.44	0.12	0.03
	RET4.3	CC	S	-0.07	0.91	0.66	0.74
	RET4.3	CC	B	/	0.87	0.45	0.75
	RET4.3	RE (%)	S	51.80	19.41	55.24	39.60
	RET4.3	RE (%)	B	/	26.98	57.96	36.00
	LE4.1	RMSE	S	14.07	1.91	0.10	0.03
	LE4.1	RMSE	B	/	2.69	0.10	0.04
	LE4.1	CC	S	-0.16	0.92	0.21	0.71
	LE4.1	CC	B	/	0.87	-0.17	0.73
	LE4.1	RE (%)	S	32.70	20.06	52.80	30.23
	LE4.1	RE (%)	B	/	32.48	52.76	35.52
	LE4.2	RMSE	S	4.15	1.75	0.09	0.03
	LE4.2	RMSE	B	/	1.75	0.08	0.03
	LE4.2	CC	S	0.29	0.92	-0.11	0.64
	LE4.2	CC	B	/	0.91	0.02	0.60
	LE4.2	RE (%)	S	3.34	17.91	45.84	19.30
	LE4.2	RE (%)	B	/	19.65	14.21	16.35

Figures for Chapter 4

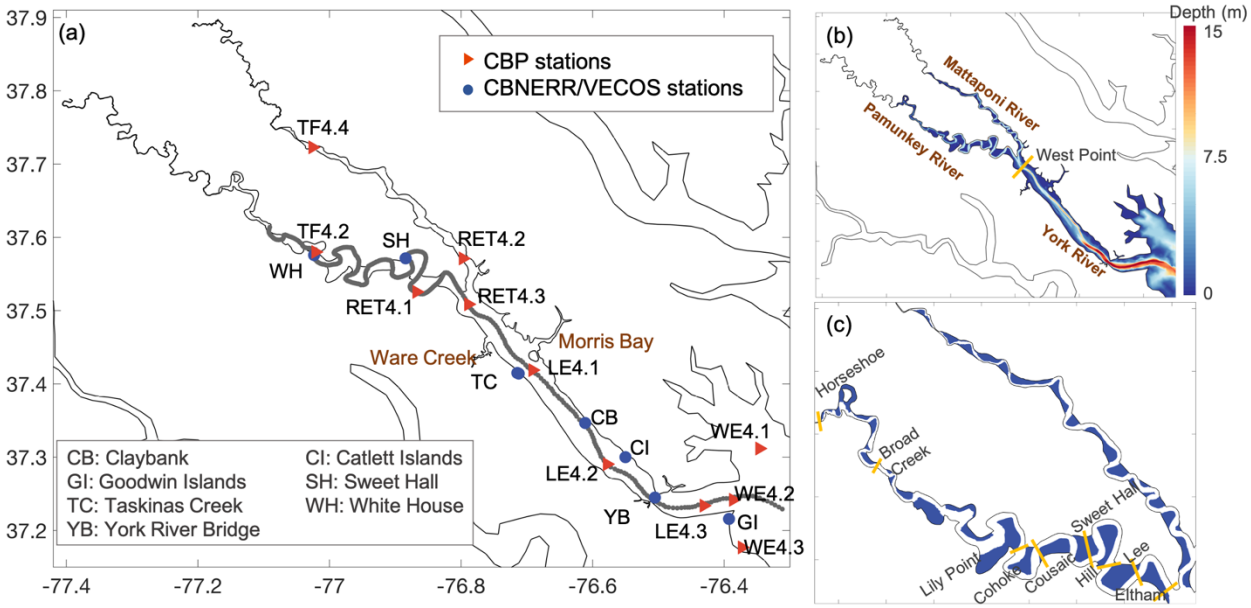

Fig. 4-1: (a) The York River Estuary. The red triangles denote the Chesapeake Bay Program (CBP) stations, and the blue circles denote the stations from Chesapeake Bay National Estuarine Research Reserve (CBNERR) and Virginia Estuarine and Coastal Observing System (VECOS). The grey line denotes the along-channel transect used in this study. (b) Bathymetry of the study area. (c). Extensive and fringing marshes in the Pamunkey-Mattaponi River System. The blue polygons denote the marshes along the Pamunkey River and the Mattaponi River based on the USGS topography map. Yellow lines in panels (b) and (c) denote the interface to calculate the material exchange in this study.

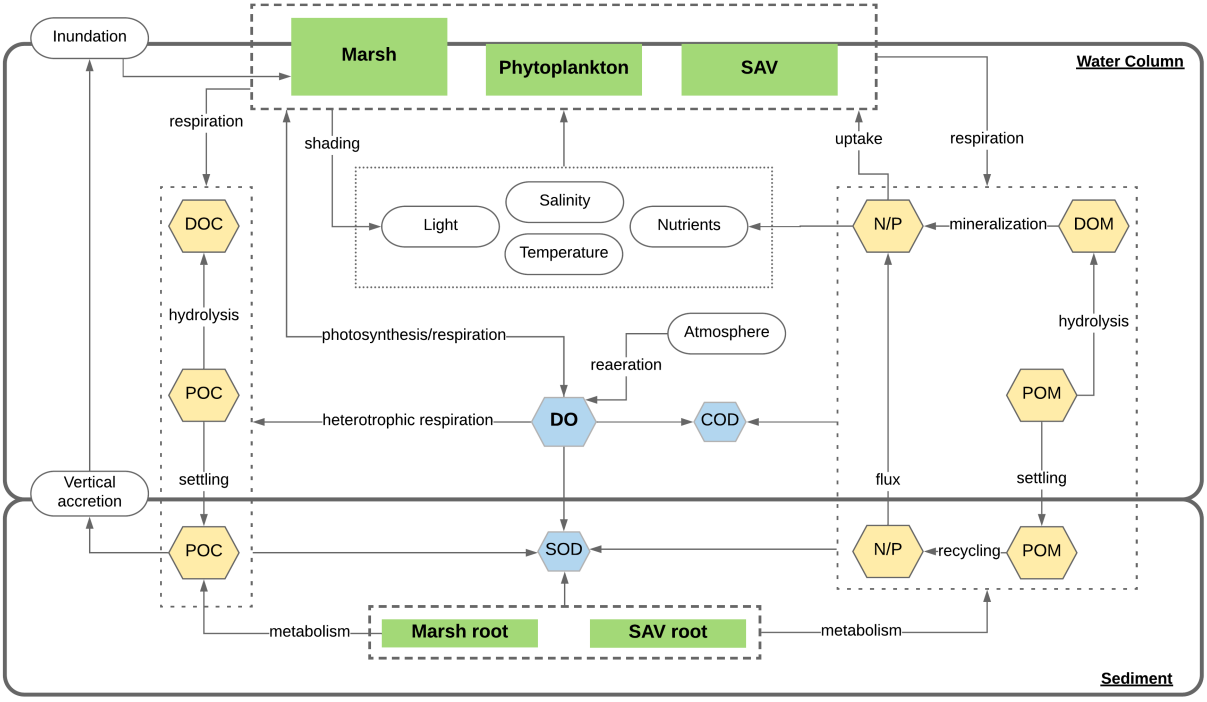

Fig. 4-2: Coupled ICM-Marsh model diagram.

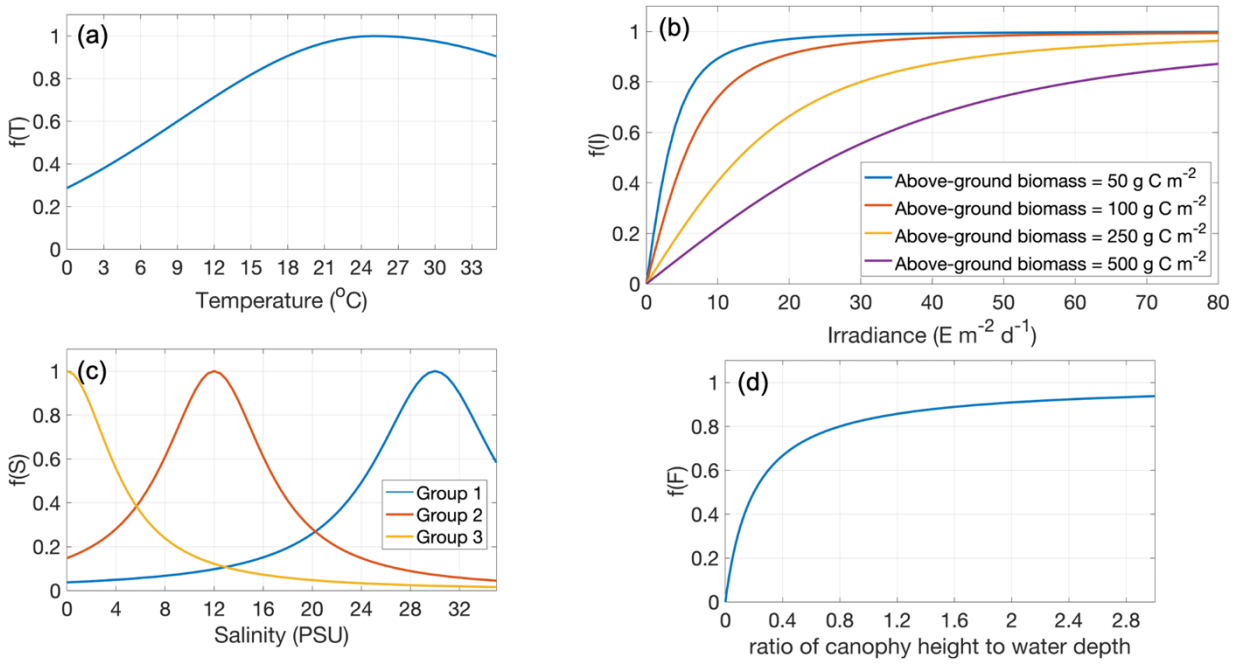

Fig. 4-3: (a) Effects of temperature on marsh production, where f(T) = 1 when the temperature reaches the optimal value. (b) Marsh production versus irradiance curve accounting self-shading. (c) Impacts of salinity on marsh production. (d) Inundation stress.

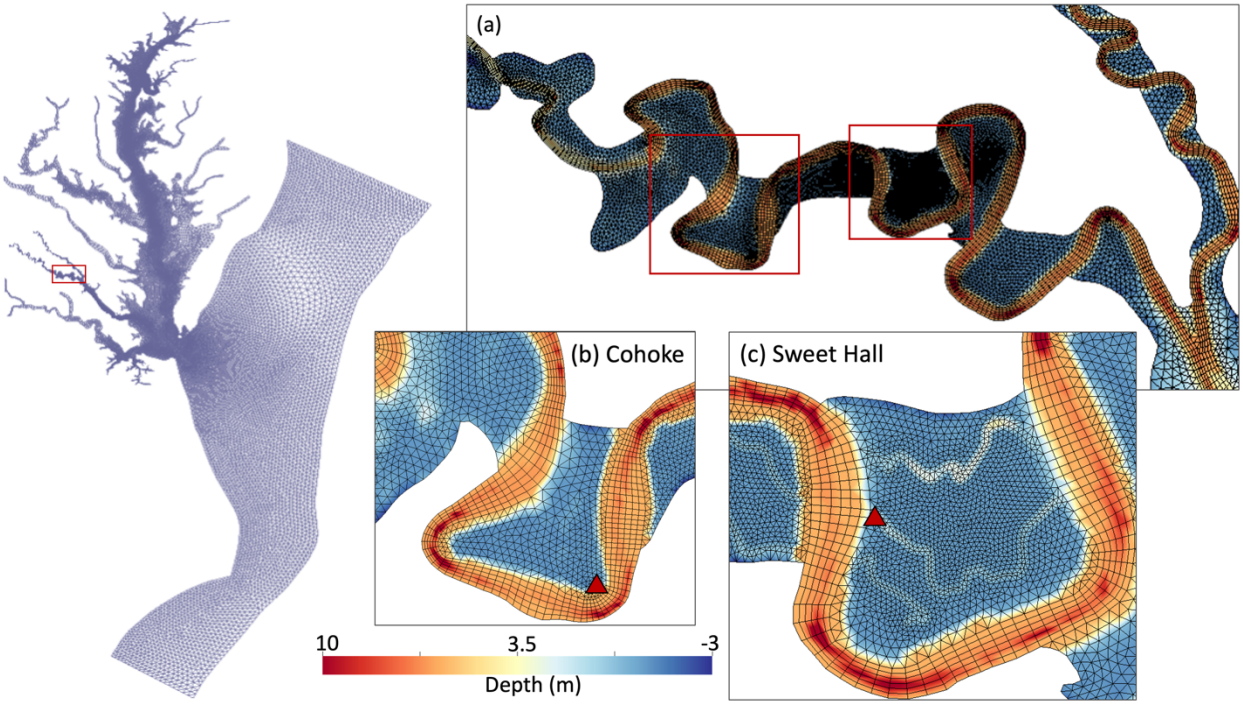

Fig. 4-4: The SCHISM model domain with zooms on (a) the confluence section of the Pamunkey River and the Mattaponi River, (b) the Cohoke Marsh, and (c) the Sweet Hall Marsh. Red triangles in panels (b) and (c) denote the sampling points of diurnal processes in this study.

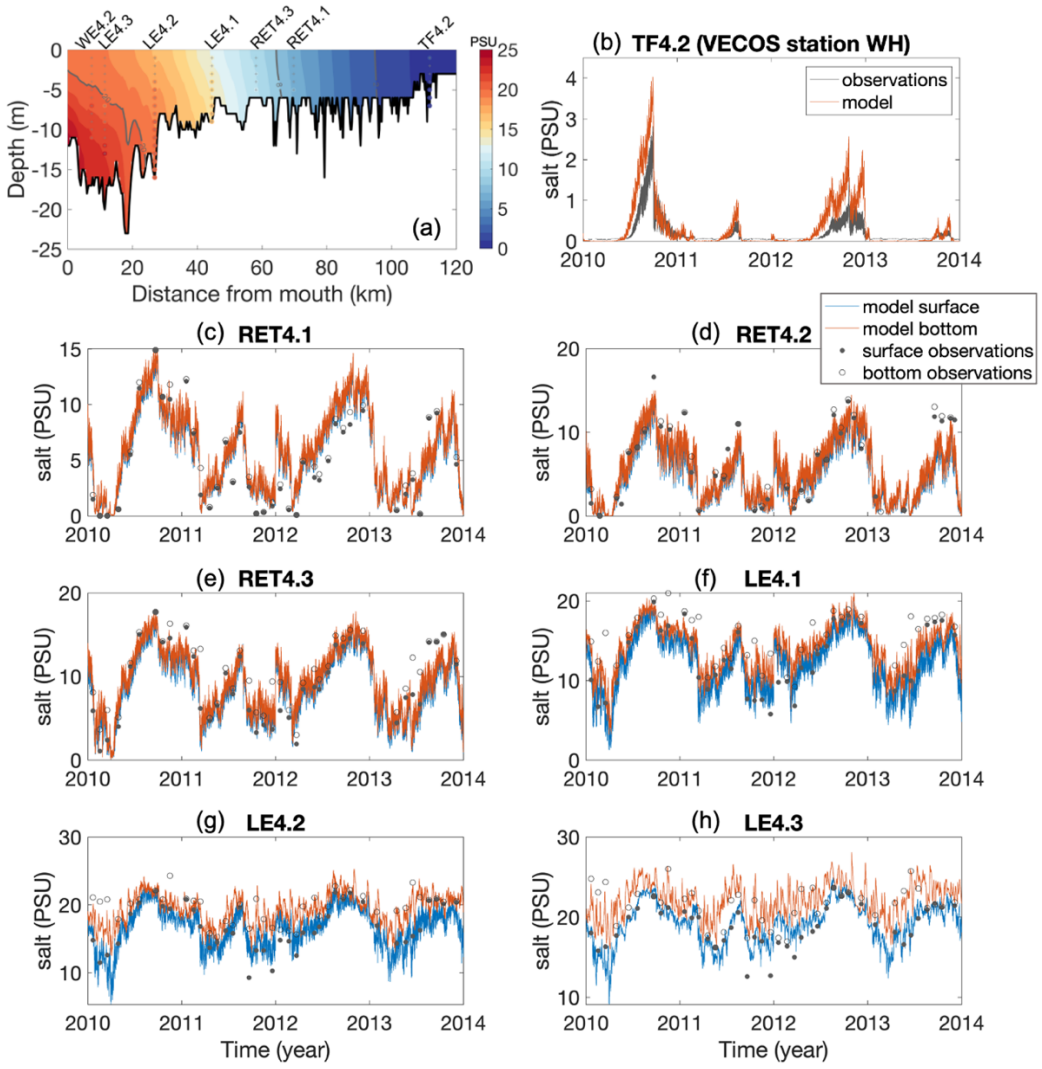

Fig. 4-5: (a) Four-year averages of salinity along the York-Pamunkey River channel as shown in Fig.1. The colored contours represent model results; the colored circles with gray "+" represent the observations from the Chesapeake Bay Program (CBP). (b-h) Time series of observed and modeled salinity at York River Estuary stations from upper stream to the mouth. (b) In station TF 4.2, the grey line denotes the high frequent observations from Virginia Estuarine and Coastal Observing System (VECOS) and the red line represents the modeled bottom salinity. (c-h) In the remaining stations, grey dots and circles denote CBP observations. Blue lines represent the surface modeled salinity and red lines represent the bottom salinity.

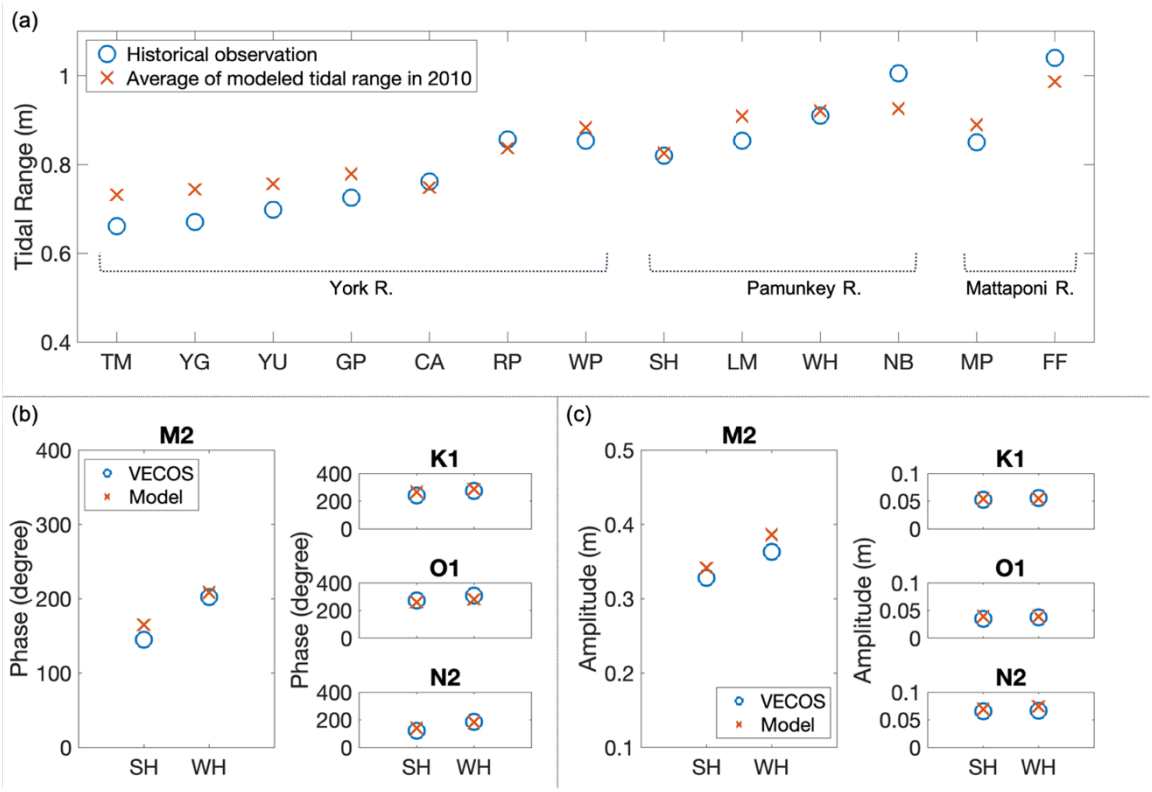

Fig. 4-6: (a) Comparison between the average of modeled tidal range in 2010 and historical observations in the York River Estuary. Historical observations are from NOAA tide tables and Virginia Estuarine and Coastal Observing System (VECOS). (b) and (c): Tidal harmonics for 4 major constituents at two VECOS stations with available observations in 2010 listed in Fig. 4-1a.

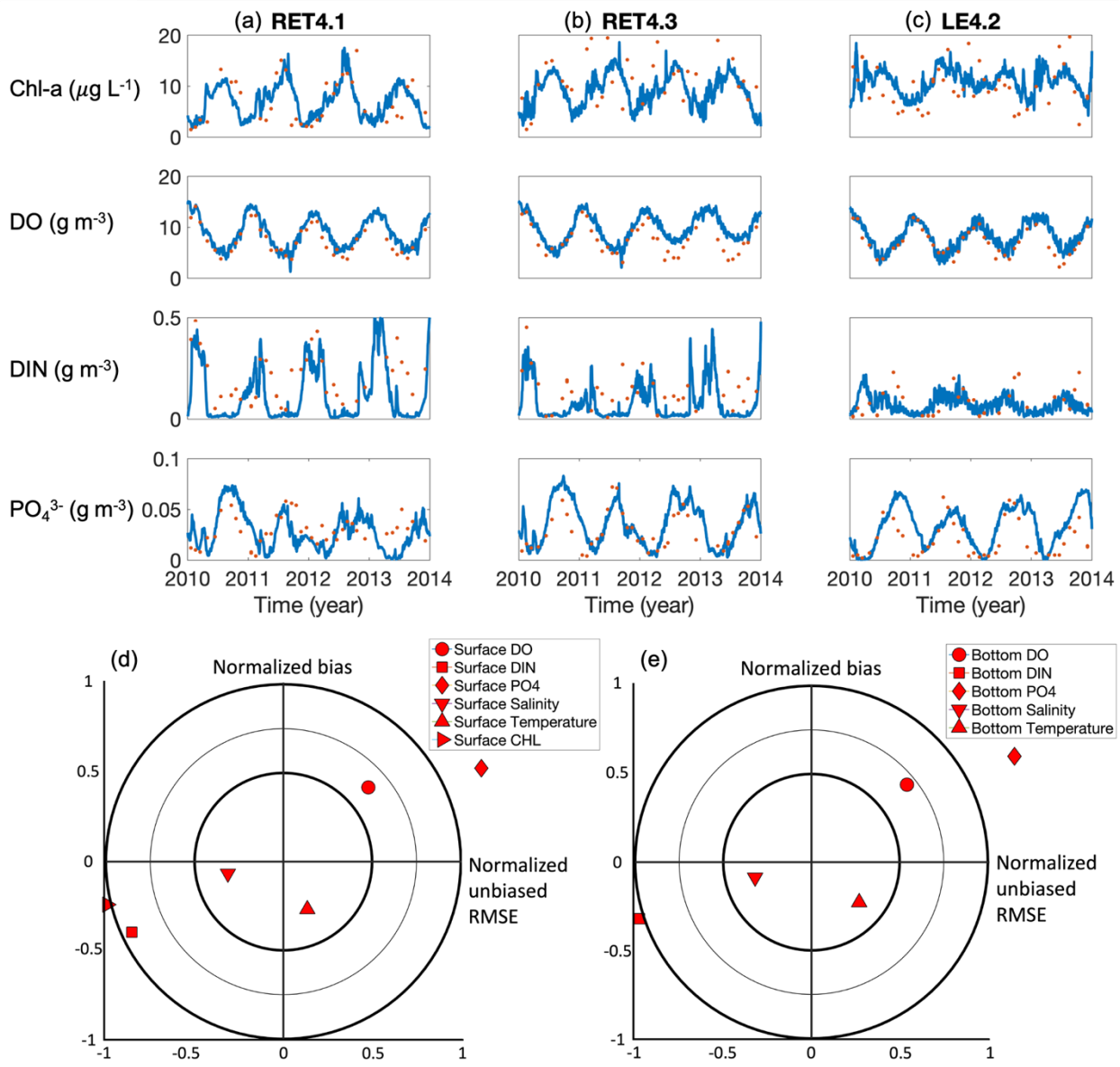

Fig. 4-7: (a-c) Comparisons of model-simulated (blue lines) and observed (red dots) water properties at three stations along the channel of the Pamunkey to the York River, including surface chlorophyll-a, bottom DO, DIN, and PO43-. (d,e) Target diagram for DO, DIN, phosphate, salinity, temperature, and surface chlorophyll-a at all CBP stations with sufficient observations (RET4.1, RET4.2, RET4.3, LE4.2, and LE4.2). Station locations are denoted in Fig. 4-1a.

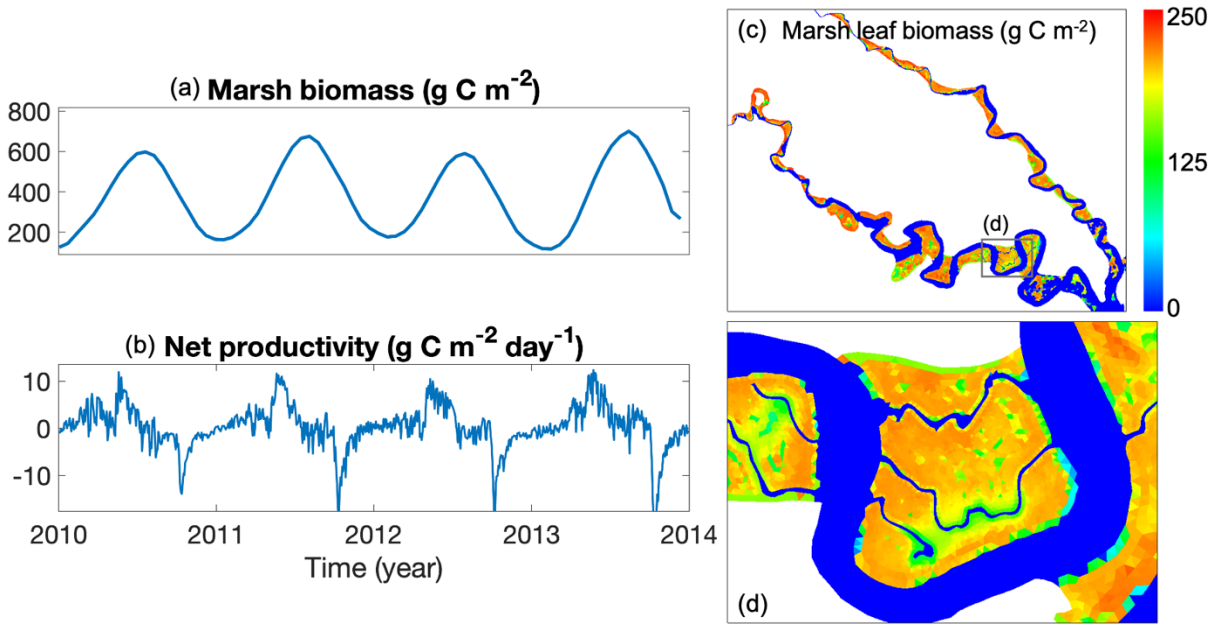

Fig. 4-8: (a,b) Spatial averages of marsh biomass (including leaf, stem, and root) and net marsh productivity in Sweet Hall Marsh. (c) Spatial distribution of tidal freshwater marsh leaf biomass in the York River Estuary in summer, and (d) Zoom-in of the Sweet Hall Marsh.

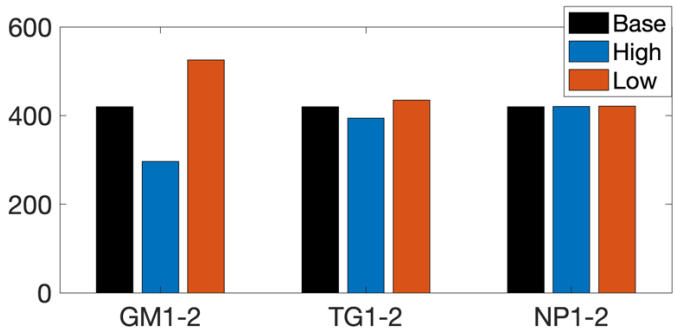

Fig. 4-9: Response of annually-averaged tidal freshwater marsh biomass (g C m-2) in the Sweet Hall Marsh to sensitivity tests listed in Table 4-2 (GM1,2, TG1,2, and NP1,2). “High” denotes the changed parameters are larger than the Base Scenario and “Low” indicates the modified parameters are smaller than original values.

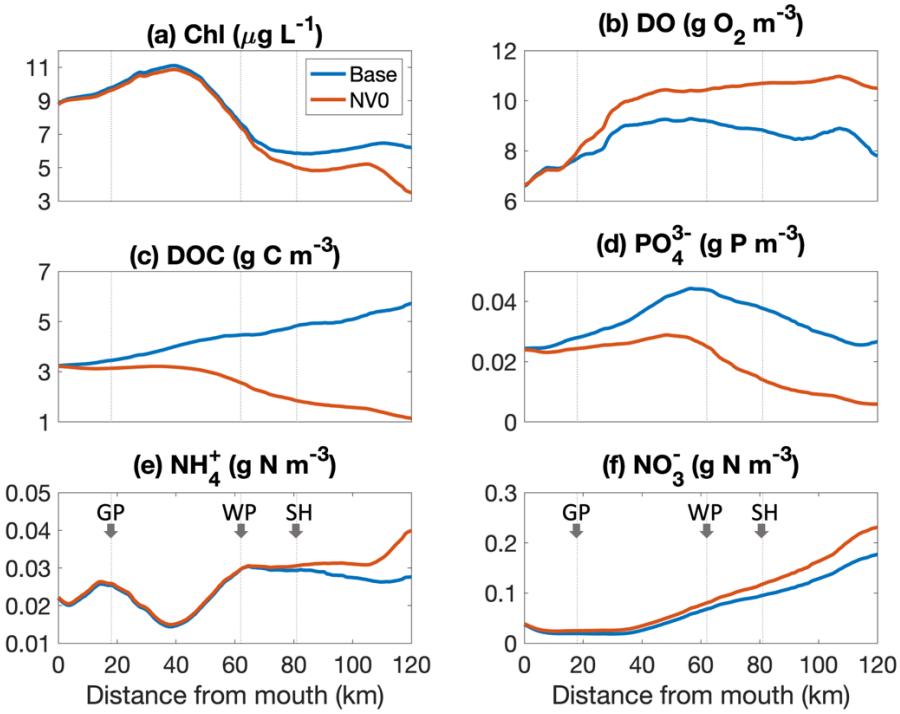

Fig. 4-10: Comparisons of Base Scenario and selected sensitivity tests (NV0) on the annual mean values of bottom DO and other surface water properties, including chlorophyll-a, ammonia, nitrate and nitrite, phosphate, and dissolved organic carbon, along the channel of the Pamunkey and the York Rivers. The along-channel transect is denoted in Fig. 4-1a. Locations of Gloucester Point, West Point, and Sweet Hall are denoted in panels (e) and (f) along with grey dotted lines.

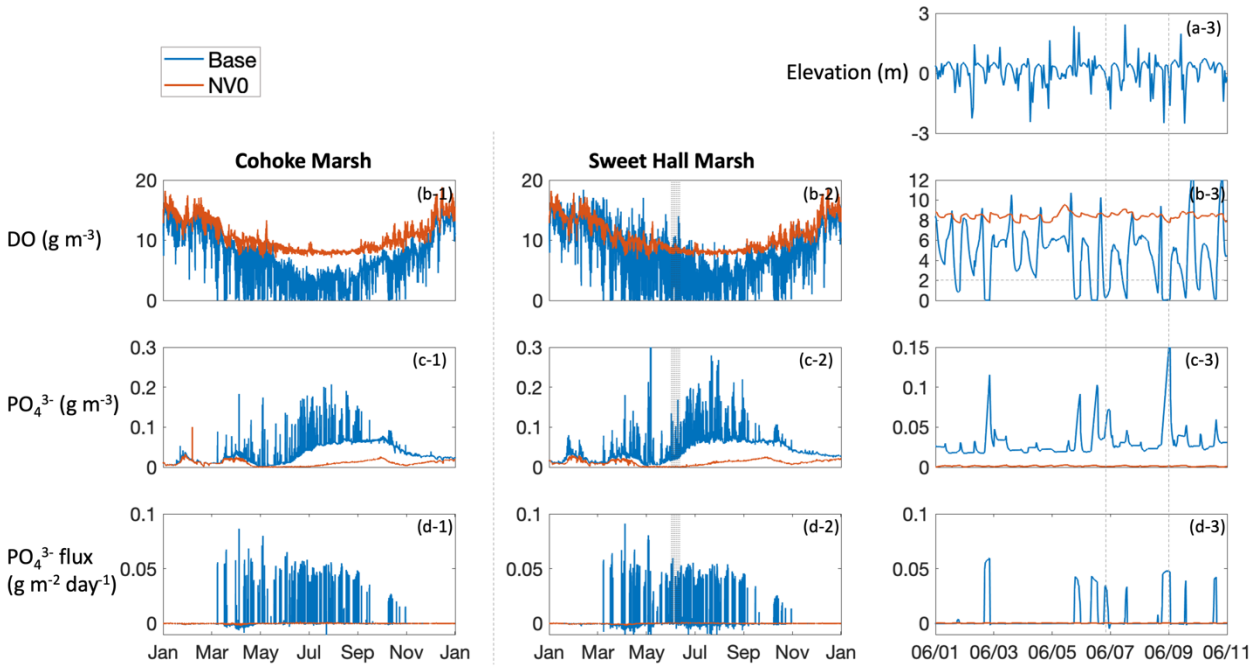

Fig. 4-11: Simulated water properties (a) elevation, (b) dissolved oxygen, (c) phosphate, and (d) sediment phosphate flux at two marsh stations (1) Cohoke and (2) Sweet Hall in Base and NV0 (marsh removal) scenarios. The two marsh stations are denoted in Fig. 4-4bc. (abcd-3) Zoom-in of a 10-day window in summer denoted with grey shade in (2) Sweet Hall Marsh. The grey dotted horizontal line in (b-3) denotes a dissolved oxygen concentration of 2 g m-3. Grey dotted vertical lines in (3) denote two moments of low tide.

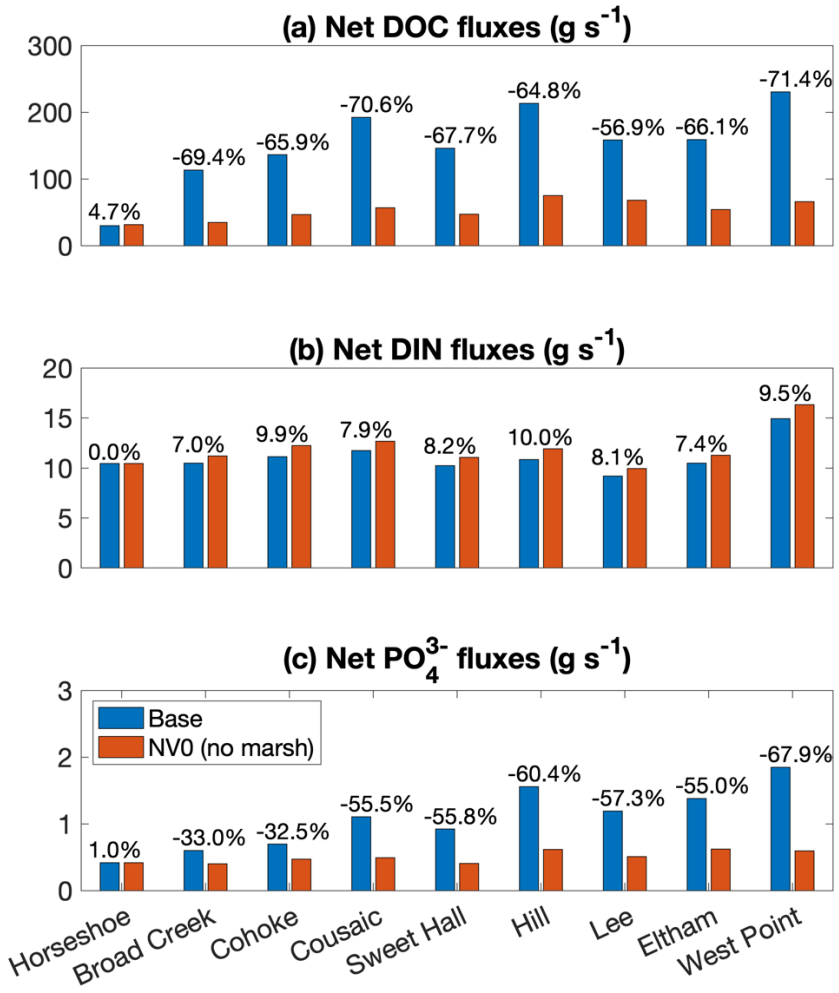

Fig. 4-12: Net fluxes of (a) dissolved organic carbon, (b) dissolved inorganic nitrogen, and (c) total inorganic phosphate from the upper stream of Pamunkey River to the downstream in the Base Scenario and sensitivity test NV0. Locations of these cross-sections are denoted in Fig. 4-1bc. Percentage denoted in each panel equals to (NV0-Base)/Base×100%. In these cross-sections, the influx (negative) refers to the direction from the river mouth to the upper streams and the outflux (positive) refers to the direction from upper stream to downstream.

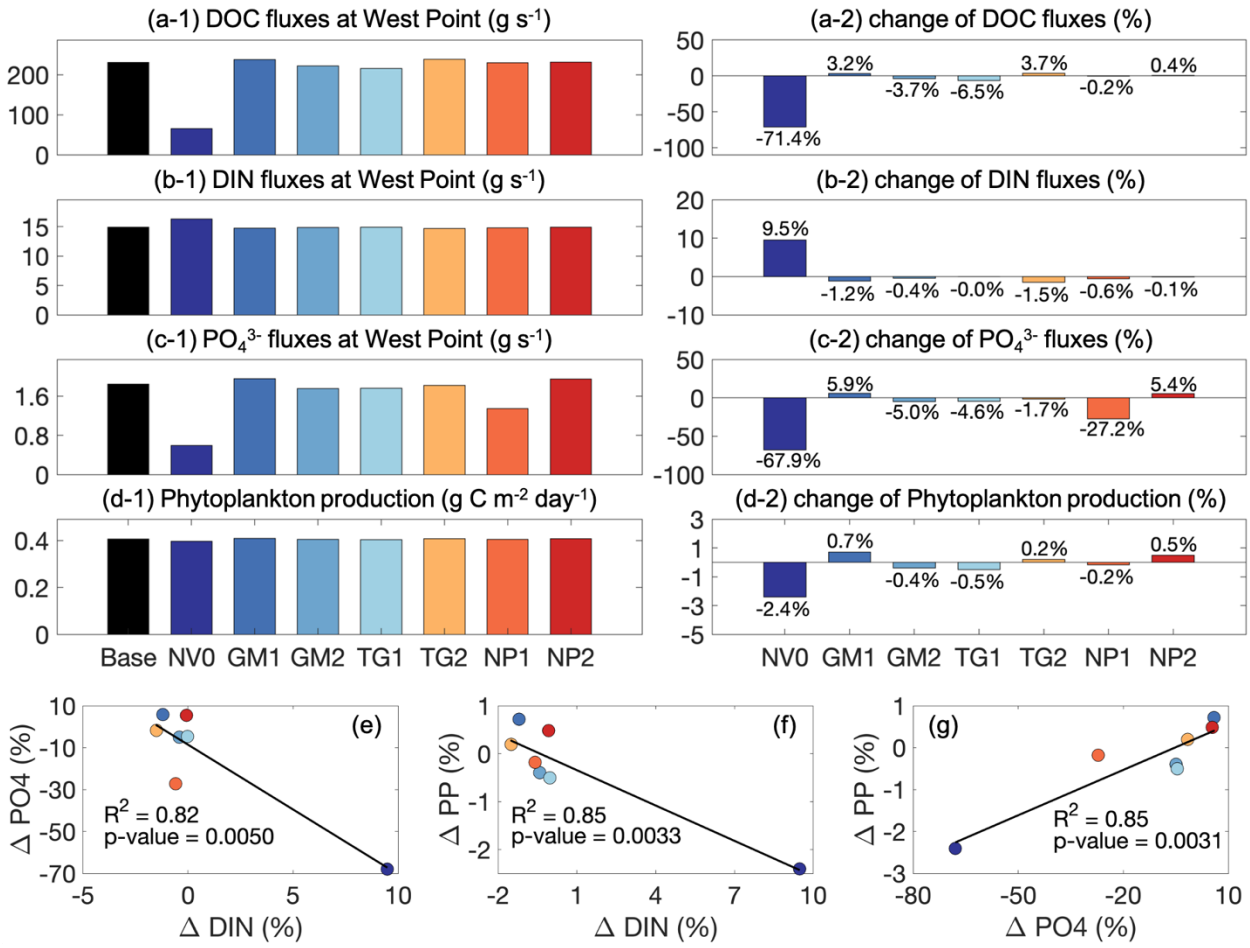

Fig. 4-13: (a-c) Net nutrient fluxes from the West Point to the York River and (d) spatially averaged phytoplankton production in the York River Estuary in Base Scenario and sensitivity tests. (e-g) Linear regressions between the changes of DIN fluxes, PO43- fluxes, and the estuary phytoplankton production as shown in (b-d). The colors of the points in (e-g) correspond to those in (ab) for each sensitivity test.

Chapter 5

5. Impacts of sea-level rise on the tidal marshes and estuarine biochemical processes

Abstract

We use numerical tools to investigate the impacts of Sea-level Rise (SLR) on the biochemical processes in the York River Estuary with extensive tidal marshes. A fully-coupled hydrodynamic-water quality-marsh model is utilized in this study, which accounts for the spatial-temporal variations of the physical-biochemical interactions between tidal marshes and surrounding waters. An idealized SLR scenario is conducted based on the calibrated Base Scenario, in which the marsh platform is assumed to have sufficient vertical accretion to keep up with the SLR. Results show that SLR increases the tidal range and flooding duration, which tends to enhance the exchanges of materials between the tidal marshes and the surrounding waters. With an increase in light utilization and the area of shallow water habitats under SLR, phytoplankton production mostly increases in the shallow water regions of the York River. Therefore, the organic carbon in the open water is fueled by the shallow waters and the enhanced transport of organic carbon from the marsh under SLR. The response of the DO budget in the York River Estuary is controlled primarily by the combination of the water column respiration, net metabolism of the benthic layer, reaeration, phytoplankton production, and enhanced stratification under SLR. Net DO flux out of York River increases at the York River mouth. Diel DO variation, especially in the marshes in the upper estuary, encourages more phosphorus release from the sediment. The changes in dissolved nitrogen under SLR are relatively minor.

5.1 Introduction

Sea-level rise (SLR) is well known to affect both physical (e.g., tidal range, salinity, and estuarine circulation) and biochemical processes (e.g., phytoplankton production, and nutrient dynamics) in estuaries. The response of the estuarine biochemical processes to SLR can be considered as a combination of changes in both the physical and biochemical processes. The impact of SLR on the tidal marshes can affect the estuarine circulation and water quality. With SLR, tidal marshes experience an evolution over succession, dominated by the rise of the platform through vertical accretion or the drowning of mudflats from erosion (Craft et al., 2009; Boon, 2012). SLR also affects the ecological functions of tidal marshes, which in turn affects the oxygen and nutrient dynamics in estuaries (Axelrad et al., 1976; Jordan et al., 1983; Chambers et al., 1992; Chmura, 2003; Bridgham et al., 2006). For example, different responses of the tidal range to SLR are a major factor for the material exchange between marshes and open water. In previous studies, the response of tidal ranges to SLR was predicted to be nonlinear under multiple settings of estuaries (Flick et al., 2003; Hall et al., 2013; Pelling et al., 2013; Holleman and Stacey, 2014; Lee et al., 2017; Ross et al., 2017; Du el al., 2018). Cai et al. (2022) emphasized the role of marsh evolution that led to different responses of tidal range to the SLR in tidal wetlands. If the tidal marsh accretion can keep up with the SLR, the tidal range is projected to increase. The increased tidal range will further strengthen the exchanges between the marsh and the mainstem estuary. Increased flux of saltwater from the oceanside is another major consequence of rapid relative SLR in an estuary (Bates et al., 2008; Boon, 2012; Hong et al., 2020). As a result, there is observable evolution from freshwater marsh to brackish marsh in the community structure in response to the enhanced saltwater intrusion (Neubauer and Craft, 2009;

Sutter, 2014). These shifts in community structures may affect the ecological functions of tidal marshes due to the distinct roles played by each marsh plant group.

Besides the impacts on the tidal marshes, SLR also affects local nutrient dynamics directly. For example, increased salinity under the enhanced saltwater intrusion is favorable for the bottom release of phosphorus that is bound to iron (Fe), which tends to have enhanced dissolution under higher salinity (Jordan et al., 2008). Salinization also tends to alter the microbial community composition or inhibit microbial activities, which inhibits nitrification and the coupled nitrification-denitrification (Rysgaard et al., 1999; Santoro, 2010). Also, ammonium absorption in sediments is found to markedly decrease with increased salinities (Rysgaard et al., 1999). The above two processes lead to enhanced bottom ammonium flux. Furthermore, SLR is predicted to change the benthic-pelagic coupling and increase the water column phytoplankton production (PP) by changing the local bathymetry and light utilization in shallow shoals (Cai et al., 2021). Along with the potential changes in the nutrient exchange between the tidal marshes and the adjacent channel, as well as the sediment nutrient release, the local PP could be altered. In short, the feedback loop between SLR and marsh is complex and nonlinear in nature, resulting in large uncertainties in future predictions and thus warrants careful research using a variety of tools.

Considering the nonlinear responses of physical and biochemical processes to SLR, numerical modeling may be the best approach to understand the impacts of SLR on the aquatic system, as it can be built to account for various ecological functions. Many numerical studies have investigated the impacts of SLR on some estuarine biochemical processes (e.g., hypoxia), but few of them have included the tidal marshes explicitly in the model (Wang et al., 2017; Irby et al., 2018; St-Laurent et al., 2019; Ni et al., 2020; Cai et al., 2021). For a few models that did

consider the contributions of marsh to nutrient burial and exports (e.g., Cerco and Tian, 2021), the process was often simplified, because the tidal marshes were not explicitly represented in the estuarine model grid and the tidal flooding and inundations under SLR were not simulated. In addition, the loss rates of the nutrients and DO for marshes under SLR were unknown and sometimes were assumed to be the same as the current situations. In this study, a high-resolution three-dimensional unstructured-grid (UG) hydrodynamic-water quality-marsh model is used to investigate the impacts of SLR on biochemical processes in the York River Estuary, a typical microtidal estuary in the lower Chesapeake Bay where extensive tidal marshes exist. The inclusion of a dynamic marsh module helps to investigate the responses of the tidal marshes to SLR and the consequent impacts on the estuarine biochemical processes with sufficient spatial and temporal variations. This paper is organized as follows: descriptions of the modeling tool, scenario, and analysis methods are presented in Section 5.2. Responses of the estuarine biochemical processes, including the tidal marsh, nutrients, phytoplankton productions, and oxygen dynamics, are presented in Section 5.3. Section 5.4 presents the discussions on the physical drivers contributing to the responses of the estuarine biochemical processes, with specific analysis of the oxygen dynamics in different sections of the York River Estuary. Section 5.5 summarizes the entire study and proposes a conceptual model for the impact of SLR on the York River Estuary.

5.2 Methods

5.2.1 SCHISM-ICM-Marsh Model

We use a fully coupled hydrodynamic, water quality, and marsh model (SCHISM-ICM-Marsh) for this study (Cerco and Cole, 1994; Zhang et al., 2016; Cai et al, 2020; Cai et al., in

preparation). SCHISM-ICM-Marsh solves the physical and biochemical processes simultaneously and accounts for the interactions between the marsh and the aquatic system. It is designed for simulations on seasonal and annual time scales. A distinctive advantage of SCHISM is its semi-implicit time-stepping scheme, implemented in a hybrid finite-element and finite-volume framework, to solve Navier-Stokes equations. All terms that place stringent stability constraints, including the vegetation drag terms are treated implicitly, so the model time step is not restricted by the Courant-Friedrichs-Lewy condition or the vegetation terms in this numerical scheme. This numerical scheme ensures high efficiency because not only high resolution is required to resolve the patchy marshes, but also the 'nearly submerged' marsh leaves and the resultant strong shears would otherwise impose a severe stability constraint (Zhang et al. 2020). There are 21 water quality state variables in ICM, including dissolved oxygen, three algal assemblages, three groups of carbon, five groups of nitrogen, and four groups of phosphorus. Three marsh assemblages, comprised of tidal freshwater marsh, brackish marsh, and salt marsh, are included in the coupled marsh model. Each marsh species consists of three components – leave, stem, and root. SCHISM simulates the transport of the 21 water quality state variables, while the coupled ICM-Marsh simulates the local kinetic processes of the 21 state variables and the three marsh plants. In addition, benthic algae are included in the water quality model to account for their productivity and interactions with the carbon, oxygen, nitrogen, and phosphorus pools (Cerco and Seitzinger, 1997).

5.2.2 Study area

The lower York River Estuary starts from the confluence of Pamunkey River and Mattaponi Rivers at West Point. It is the 5th biggest tributary in Chesapeake Bay. The length of

the York River is about 50 km from West Point to Goodwin Island. In the Pamunkey and Mattaponi Rivers, the tidal portion extends about 90 km and 70 km from the West Point, respectively (Brooks, 1983; US Geological Survey, 2002, http://water.usgs.gov). The average width of the York River is 3.8 km while the meandering Pamunkey River and Mattaponi Rivers are several hundreds of meters wide (Nichols and Kim, 1991). The York River downstream of West Point has an average water depth of 4.9 m, and the channel depth is up to 20 m at Gloucester Point (Cronin, 1971; Nichols et al., 1991). With the Pamunkey and Mattaponi Rivers and the tidal marshes included, the mean depth of the whole York River Estuary is smaller than the reported 4.9 m downstream of West Point. Therefore, a SLR of 1.5 m would increase the mean local depth by at least 30%, which may significantly alter many local processes.

In the York River Estuary, the annual high and low temperatures are ~35.7 ^{o}C and ~0.9 ^{o}C, respectively with a clear seasonal trend (Brooks, 1983). The average precipitation is about 95.9 cm. Waves are usually considered to be insignificant for this region (Friedrichs, 2009). The York River estuary is a micro-tidal estuary, whose mean tidal range increases from 0.7 m at the mouth to more than 1 m in upstream of the Pamunkey and Mattaponi Rivers (https://tidesandcurrents.noaa.gov/historic_tide_tables.html). The tidal range at the extensive tidal marshes is from about 0.75 m to about 1 m. The bottom salinity at the York River mouth can exceed 25 PSU, with a range of 0 to 20 PSU at the West Point dependent on the freshwater discharge (https://www.chesapeakebay.net/what/data). The upper portion of the Pamunkey and Mattaponi Rivers are mostly tidal fresh with a transition zone near the West Point (Shen and Haas, 2004). The mean freshwater discharge from the Pamunkey River and Mattaponi Rivers are 28.7 $m^3 s^{-1}$ and 14.4 $m^3 s^{-1}$, respectively; and the York River Estuary has a mean residence time of 104 days (Shen and Haas, 2004).

The river discharge in the York River Estuary has been recognized as a controlling factor that regulates the phytoplankton dynamics temporally and spatially by residence time, nutrient loading, light regime, and tidal mixing (Sin et al., 1999). Phytoplankton dynamics and productivity in the York River Estuary are mainly regulated by nutrient supply and light availability utilization (Sin et al., 2006). Limitations from dissolved inorganic nitrogen (DIN), phosphate, and light shift the governing role of regulation temporally and spatially (Sin et al., 1999; Sin et al., 2006). The agricultural land, urban areas, and forested lands dominate the nutrient loads to the York River Estuary with the total nitrogen (TN) loading on the order of 3.5×10^6 kg yr^{-1} and total phosphorus (TP) loading on the order of 3.4×10^5 kg yr^{-1} (Sprague et al., 2000; Dauer, 2005). Hypoxia (defined as dissolved oxygen (DO) concentration is lower than 2 mg L^{-1}) or under-saturation of DO by 50% has often been observed in the York River in summer (Kuo and Neilson, 1987). In addition to the observed hypoxia in the channel, diel variation in DO is also observed in temperate unstratified shallow waters and habitats (Reay, 2009).

Excluding the embayed tidal marshes in the sub-tributaries, there are in total about 50.6 km^2 of extensive tidal marshes in the York River Estuary, which takes up almost 97.27% of the total marsh coverage in the entire York River estuary (Mitchell et al., 2017). Although experiencing community shift from freshwater spices to brackish ones, the areal extent of marshes in the upper York River Estuary (Pamunkey and Mattaponi Rivers) was reported to have changed little (<0.009%) over the past decades (Sutter, 2014; Mitchell et al., 2017), so the marshes were believed to have sufficient vertical accretion with both abundant marsh productions and allochthonous sediments to keep up with the SLR (Neubauer and Craft, 2009; Mitchell et al., 2017).

5.2.3 Model implementation and scenarios

Base Scenario simulation uses the current mean sea level as a reference datum for model simulations, and the model has been developed and calibrated by Cai et al. (in preparation; chapter 4 in this dissertation) for the years 2010 to 2014 with a single non-split time step of 150 sec. The base simulation period for SLR scenarios is the year 2010, which is regarded as an average flow year. The ocean boundary extends offshore to the shelf break to minimize the influence of open ocean conditions on the interior of the Bay and the York River Estuary. This grid contains 47,477 nodes and 73,433 elements, and the nominal resolution in the extensive marshes in the York River Estuary (e.g., Sweet Hall Marsh) is about 50 m. In the rest part of the York River estuary, the along-channel resolution ranges from 300 m to 100 m from the mouth to the upstream, while the cross-channel resolution ranges from 200 m to less than 100 m to ensure that at least six rows of elements are used to accurately represent the channel. A hybrid vertical grid system LSC^2 (Localized Sigma Coordinates with Shaved Cells) with up to 52 vertical layers and one layer for the shallow wetlands is applied in this domain.

Interpolated elevations from two tidal gauges at Lewes, DE, and Beaufort, NC were used to force elevations at the ocean boundary. The boundary temperature is obtained from the hybrid coordinate ocean model (HYCOM, Chassignet, et al., 2007) and the boundary salinity is from World Ocean Atlas monthly climatological data. We obtained the daily runoff and nutrient loads from the watershed from the outputs of Phase 6 Watershed Model of Chesapeake Bay Assessment Tool (CAST; Shenk and Linker, 2013) and the atmospheric forcing and heat fluxes from the North American Regional Reanalysis (Mesinger et al., 2006). The marsh generation used the USGS topography map (https://www.usgs.gov/core-science-systems/national-

geospatial-program/us-topo-maps-america?qt-science_support_page_related_con=0#qt-science_support_page_related_con).

SLR scenarios of 1.5, 1.0, and 0.5 m were added to the sea surface height at the ocean boundary of the Base Scenario to the SLR scenario. The SLR scenario of 1.5 m was mainly used in this study to study the response of the biochemical processes, while the rest were used as sensitivity tests. The defined marsh wetlands also had an increase of 1.5, 1.0, and 0.5 m on the bottom elevation by assuming the vertical accretions of these marshes keep up with the SLR without changing the horizontal extension (Fig. 5-1d; Fig. 5-2ab; Cai et al., 2022). This idealized SLR-driven marsh evolution (keeping up with the SLR) avoids an explicit simulation of long-term marsh migration (which is beyond the seasonal and annual time scales simulated by the current model). We focused on the dynamic changes in the biochemical processes under this hypothetical scenario. The Base and SLR scenarios share identical oceanic, watershed, and atmospheric forcings except for the changes in the oceanside elevation and the bathymetry of tidal marshes. Other processes, such as river discharge, wind, solar radiation, and nutrient loadings, are kept the same for SLR scenarios in this study; by doing so, we can isolate and investigate the impacts only driven by SLR.

5.2.4 Analysis methods

5.2.4.1 Marsh productivity and phytoplankton production

In the model, marsh net productivity is calculated by:

$$\mathrm{MPP} = \sum_{m=1,2,3}(Plf_m \cdot (1 - Fam_m) - MTlf_m \cdot BMlf_m) \cdot \boldsymbol{LF_m} - MTst_m \cdot BMst_m \cdot ST_m - BMrt_m \cdot RT_m \quad (5\text{-}1)$$

where $m = 1,2,3$ is the index of the three tidal marsh groups (salt marsh, brackish marsh, and freshwater marsh). $\boldsymbol{LF}$, $\boldsymbol{ST}$, and $\boldsymbol{RT}$ (g C m^{-2}) are biomass of leaf, stem, and root of the vegetation, respectively. Plf (day^{-1}) is the growth function of the leaf. Fam is the fraction for active metabolism during photosynthesis. $BMlf$, $BMst$, and $BMrt$ (day^{-1}) are basal metabolism rates of the leaf, stem, and root, respectively. $MTlf$ and $MTst$ are seasonal mortalities of leaf and stem. Local areal PP is computed by integrating volumetric PP in the water column for each element:

$$\mathrm{GPP} = \sum_{i=1}^{n}(\mathrm{C1}_i \cdot \mathrm{G1}_i + \mathrm{C2}_i \cdot \mathrm{G2}_i + \mathrm{C3}_i \cdot \mathrm{G3}_i) \cdot \mathrm{dep}_i \tag{5-2}$$

where GPP is areal gross primary production of phytoplankton (g C m^{-2} day^{-1}), n is the number of vertical layers in each element, i is the vertical layer index, $\mathrm{C1}, \mathrm{C2}, \mathrm{C3}$ are carbon-based phytoplankton biomass of three groups (diatoms, green algae, and cyanobacteria) over each layer respectively (g C m^{-3}), $\mathrm{G1}, \mathrm{G2}, \mathrm{G3}$ are growth rates of the three phytoplankton groups (day^{-1}), and dep is layer thickness (m).

5.2.4.2 Material fluxes

Annual-averaged net material fluxes were calculated along the 11 interfaces from the upstream to the downstream (Fig. 5-1bd). Net fluxes of dissolved organic carbon (DOC), DO and inorganic nutrients were analyzed in the Base Scenario and the SLR scenario. The net flux is the result of outflux (seaward) minus influx (landward), both of which were calculated as the sectionally integrated products of the flow velocity across the interface and the concentrations of the studied material.

$$\text{net flux} = \text{outflux} - \text{influx} = \int_{\mathrm{A}} (u_n \cdot \mathrm{Var})\mathrm{dA} \tag{5-3}$$

where u_n is the cross-interface velocity (m s^{-1}), Var is the concentration of DOC or other nutrients, A is the vertical area of the interface (m^2). Positive values denote net outflux while negative values denote net influx. Averages of annual and monthly net fluxes were calculated at the selected interfaces.

5.2.4.3 Oxygen dynamics

Besides the calculations on oxygen fluxes at each interface denoted in Fig. 5-1bd, each of the major local kinetic processes that affect the oxygen dynamics were calculated in the 10 sections divided by the 11 interfaces. The major local kinetic processes analyzed include the sources of oxygen from vegetation and phytoplankton production, the sink or source from net metabolism of the benthic layer, the sink to water column respiration, reaeration, and sinks to nitrification. These rates at each section were vertically integrated and then horizontally averaged by the weight of each element area, and the sectionally-averaged values are averaged from June to August. The sum of these local changing terms and the net flux is the total changes of the oxygen budget in this section during the selected period.

5.3 Response of the estuarine biochemical processes to SLR

5.3.1 Tidal marshes

Overall, SLR causes a minor decrease in marsh biomass and productivity in most areas of the tidal marshes in the York River Estuary in this modeling study (Fig. 5-2c-e). The decrease in marsh biomass mostly happens in summer and fall (Fig. 5-2e). On the scale of all the marshes in the York River Estuary, the annual decreases of marsh biomass and productively are on the order of 20 g C m^{-2} and 0.04 g C m^{-2} day^{-1}, respectively. In other words, the annual decrease in total

marsh biomass is minor (5.18%) compared with the base value (Fig. 5-2e). Besides the minor change in biomass and productivity under SLR, the changes in the amount of local nutrient uptake and release from marsh photosynthesis and metabolism are also small, which is on the order of 3.6×10^{-3} g N m^{-2} day^{-1} and 1.1×10^{-4} g P m^{-2} day^{-1}, respectively. Thus, the changes in marsh biomass and productivity have a negligible impact on the material exchanges between the tidal marshes and channels under SLR.

The comparisons of the Base and SLR Scenarios on the three limiting factors (inundation stress, light limitation, and salinity stress) of marsh leaf growth suggest the predicted decreases in marsh biomass and productivity under SLR are dominated by the increased inundation stress (Fig. 5-3a). The change in the inundation stress is mainly driven by the change in tidal range and plant height. Some observations indicate that the plant height along with the marsh biomass can increase in response to the increased tidal range so that the inundation stress will not limit the growth of the marshes (Morris et al., 2002). For this study, the long-term response of marsh biomass to the change in the tidal range under SLR is not simulated by the model, so the parameters to determine the height based on the above-ground biomass are assumed unchanged. Therefore, the modeled inundation stress increases. It is possible that the marsh plant adapt to the changing environment to keep the inundation stress overall unchanged, though it is not simulated in this study with identical parameter sets. Given the identical solar radiation in the Base and SLR scenario, the change in light limitation is mainly driven by the change in water column attenuations and self-shading, which is dominated by plant height and biomass. Other conditions, such as the alleviation of salinity stress, help to increase salt marsh plant productivity, which results in a minor increase in annual marsh biomass and productivity in certain areas and periods (Fig. 5-3b). The model also suggests there is a shift in marsh species from tidal freshwater marsh

to the brackish marsh and brackish marsh to salt marsh responding to salinity gradient, even the total biomass does not change much.

5.3.2 Nitrogen and phosphorus

The model results show that the changes of inorganic nutrients have varying trends upstream and downstream. NH_4^+ and PO_4^{3-} concentrations mostly increase under SLR in the upstream above West Point where extensive marshes exist and slightly decrease in the downstream York River (Fig. 5-4ce). Meanwhile, the concentrations of NO_3^- decrease in most areas of the York River Estuary under SLR (Fig. 5-4d). The overall decrease in nutrients in the downstream York River indicates that more nutrients are taken up by phytoplankton to support the increased PP in the York River Estuary as suggested in Fig. 5-5. The increase in NH_4^+ concentration in the upstream can be up to about 0.004 g N m^{-3} and the decrease in the NO_3^- concentration is less than 0.02 g N m^{-3} (Fig. 5-4cd). An increase of NH_4^+ accompanied by a decrease of NO_3^- is mainly due to changes in PP and nutrient recycling. The decrease in NO_3^- concentration is also attributed to the overall lower DO level and frequent occurrence of temporal hypoxia in the estuary under SLR (Fig. 5-4ad and Fig. 5-10b). The lower DO level inhibits or slows down the nitrification process, while it favors the dissimilatory nitrate reduction to ammonium (DNRA) and denitrification. Both the increases of NH_4^+ and decrease of NO_3^- contribute to the response of DIN, which mostly decreases in the estuary but slightly increases in the lower part of Pamunkey River. The PO_4^{3-} concentration increases by about 0.03 g P m^{-3} (112.0%) at the open water above Lily Point (Fig. 5-1d). The increase of PO_4^{3-} in the upper estuary is highly related to the overall lower DO and the enhanced sediment fluxes.

5.3.3 Phytoplankton production

SLR increases the spatially averaged PP in the entire York River Estuary by 27.4% (Fig. 5-5). In the shallow waters, PP mostly increases by up to 0.6 g C m^{-2} day^{-1} (Fig. 5-5b) and the chlorophyll-a concentration also increases. The chlorophyll-a concentration in the Pamunkey River channel slightly increases by about 0.5 μg/L (8.5%), but slightly decreases by 0.6 μg/L (7.0%) in the York River channel where PP also decreases by 0.05 g C m^{-2} day^{-1} (Fig. 5-5b). The predicted trend of PP in shallow shoals under SLR is the same as that in the Bay shallow waters (Cai et al., 2021), where the increase in shallow water habitat area and light utilization by chlorophyll-a is suggested to be the governing factor leading to the increase in PP under SLR. Since the model accurately represents the shallow water without smoothing the bathymetry, the change of shallow water habitat area is better simulated. However, the nutrient limitation can be observed in the York River main channel (indicated by the lowered nutrient concentrations) also plays a role in slightly decreasing in chlorophyll-a concentration in the York River mainstem under SLR (Fig. 5-4ef and Fig. 5-5b).

5.3.4 Oxygen and dissolved organic carbon

DO is predicted to significantly decrease in the upstream adjacent to the extensive marshes while slightly increasing in the York River (Fig. 5-4a and Fig. 5-10b). The decrease of bottom DO is up to about 1.6 g O_2 m^{-3} (18.9%) in the Pamunkey River (Fig. 5-4a). Given the situation that the water is generally mixed in this region (Friedrichs, 2009), the increased DOC causes greater heterotrophic respiration and decreases the bottom DO concentrations in the meanders. The overall lower DO level, accompanied by more low-DO events, prompts more nutrient (i.e., NH_4^+ and PO_4^{3-}) release from the sediment, which in return increases the nutrient

availability (Fig. 5-4e). The slight increase in bottom DO in the York River channel is about 0.8 g O_2 m^{-3} (8.2%) (Fig. 5-4a). A detailed analysis of DO dynamics under SLR with consideration of physical transport is presented in the next section.

Under SLR, the DOC concentration has a clear increase over the upstream of the York River Estuary (Fig. 5-4b). In the Pamunkey River, the increase in DOC concertation is up to 3.5 g C m^{-3} (63.8%) compared with the original concentration in the Base Scenario. A significant fraction of the increase in DOC in the upper streams is directly related to the increases in chlorophyll-a and PP in the Pamunkey and Mattaponi channels (Fig. 5-5b), and the rest of DOC increase is affected by marshes. Despite the minor decrease in marsh biomass, therefore the slightly decreased detritus, the overall lower DO concentration slows down the oxidation of these marsh detritus, leaving more DOC in the bottom. These DOC are exchanged and transported during each tidal cycle and contribute to the total increase in DOC in the system. Downstream West Point, the increase in PP in the shallow shoals plays a significant role in increasing the DOC concentration, though the surface channel shows a slight decrease (Fig. 5-4b).

5.4 Contributions of the physical processes

5.4.1 Tidal range and flooding in the marshes

Under SLR, the tidal range generally increases towards upstream (Fig. 5-6a). The increased tidal range is consistent with the prediction by the conceptual model in Cai et al. (2022) and model prediction in the James River (Wang and Shen, 2020), which suggests that significant reductions in frictional dissipation play a dominant role. The increase in tidal range is more pronounced towards upstream from the mouth of the York River and gradually becomes 'linear' after passing Sweet Hall. The mean increase in tidal range in the York section is about

3.8 cm (4.9%) when SLR is 1.5 m, while it can be about 17.4 cm (20.4%) and 13.4 cm (14.8%) in the Pamunkey and Mattaponi sections, respectively. The increase in the tidal range under SLR is one of the significant factors contributing to the increased outfluxes from the tidal marshes to the open water. The mean depth of inundated area, including the marsh with vertical accretion, increases by 13.7% in the Pamunkey River under SLR (Cai et al., 2022). Tidal inundations prolong significantly over the marshes beside the increased tidal range. For example, in the randomly selected sampling stations in the Sweet Hall Marsh, the inundation period is increased by about 0.5 hours in a tidal cycle (Fig. 5-10a-2). The enhanced inundation in tidal marshes increases the material exchange between the water and marsh beds. More particulate matters settle down, while dissolved nutrients are released into the flooding water. As a result, despite the overall slightly decreased marsh biomass, tidal marshes contribute to the increased nutrient fluxes from the upstream to the downstream York River.

In this study, the SLR scenario is designed with idealized marsh vertical accretions, but marsh evolution can be somewhere in the case between fully keeping up with SLR and degrading to tidal flats, depending on the supplies of sediments or the shift in the local marsh community (Reed, 1990; Reed, 1995; Mitchell et al., 2017). Predictions from Cai et al. (2022) suggest that the tidal range may increase less than the ideal fully “keep-up” scenario or even decrease if the marsh vertical accretion is smaller than the SLR or if the waterfront marshes degrade to tidal flats in a significant area. If the tidal marsh platform reaches equilibrium at a certain middle stage, the outflux of material from the tidal marshes will likely have a less increase than our current prediction or even shows a decrease, and the outflux will also have a less or even reversed impact on the estuarine biochemical processes than our current predictions due to nonlinear integrations.

5.4.2 Saltwater intrusion and estuarine circulation

Besides the change in local tidal range driven by the SLR, the change in other physical processes can also significantly affect the estuarine biochemical processes in the York River Estuary, such as the enhanced saltwater intrusion. For example, under a SLR of 1.5 m, the annual average salinity increases from 9.5 to 12.7 PSU at West Point, and from 4.6 to 6.1 PSU at the Sweet Hall Marsh (Fig. 5-6b). The intrusion length is also prolonged by 5.95 km from the Cohoke Marsh to upstream (2 PSU; Fig. 5-6c). The intrusion length is on the same order of magnitude as the James River (Rice et al., 2012; Wang and Shen, 2020). The increase in local salinity in these marshes alters the composition of the tidal marsh community in the transition region from the brackish zone to the tidal freshwater zone. For example, the fraction of brackish marshes in the entire simulated marshes increases by 9.84% (Fig. 5-1d). In addition, salinity increase in these regions contributes to depressing the local nitrification while enhancing the bottom release of ammonium and phosphate to the underlying flooding water.

SLR increases the estuarine stratification in the York River Estuary, like the predications for Chesapeake Bay (Cai et al., 2021). As suggested by the calculated oxygen fluxes along the York Estuary in Fig. 5-7ab, the enhanced exchange flow increases both the seaward and landward fluxes of oxygen. However, the changes in local DO production and consumption modify the net outfluxes of oxygen from the York Estuary to the Bay. The net oxygen fluxes show an increasing trend towards the mouth of the York (Gloucester Point) (Fig. 5-7c). This trend still exists under SLR, but the net oxygen outflux increases by 19.3% at GP but decreases by up to 27.9% at interfaces above West Point (Fig. 5-7c). The increase in DO outfluxes at GP may be due to an overall increase in productivity including PP in the York River (Fig. 5-5).

5.5 DO dynamics in the York River Estuary

Overall, the responses of bottom DO to SLR are predicted to decrease in the upstream sections (Pamunkey and Mattaponi Rivers) and a slight increase in the downstream section (York River) in this modeling study (Fig. 5-4a). Multiple processes (e.g., heterotrophic respiration, PP, and estuarine stratification) contribute to this prediction, which needs a synthetic analysis of the underlying mechanisms. The total change and each oxygen-related process in summer have distinct patterns in the upstream sections between one or two marshes (e.g., from the Cohoke to the Cousaic Marsh; Fig. 5-1d) and the downstream York River sections (e.g., from the West Point to the Clay Bank; Fig. 5-1d) (Fig. 5-8). The marsh sections have a larger total change but much smaller net fluxes via transport, compared with the York River sections (Fig. 5-8). Although the marsh sections export oxygen on an annual cycle (Fig. 5-7c), they receive oxygen from downstream areas in the summer (Fig. 5-8ab). The oxygen source from PP is larger in the York River sections, though the inundated marsh occasionally produces oxygen to the marsh sections (Fig. 5-8). The net metabolism of the benthic layer, which includes the production and consumption of oxygen by benthic algae and the sediment oxygen demand (SOD), tends to be a sink of oxygen in the marsh sections but a source to the York River sections (Fig. 5-8). The water column respiration is the largest or second-largest sink term of oxygen in all these sections, while the increase in the water column respiration is much larger (about 60%) in the marsh sections than in the York River sections (about 20%) (Fig. 5-8). All those sections take oxygen from the atmosphere, and the marsh sections, which have stronger mixing, take more oxygen, and have larger increases in reaeration under SLR than the York River sections (Fig. 5-8). The oxygen sink to nitrification in the water column is generally neglectable (Fig. 5-

8). The increase in DOC in the upper steams results in more water column respiration that consumes oxygen in the marsh sections, and the lowered DO level prompts more DOC release from detritus on the benthic layer and marsh beds under SLR (Fig. 5-4a and Fig. 5-8). On the other hand, the enhanced PP, the overall positive net metabolism in the large shallow areas of the York River, and the strengthened gravitational circulation, promote the DO level downstream under SLR, which agrees with the modeling study in Cai et al. (2021) (Fig. 5-4a and Fig. 5-8).

5.6 Material transports along the York River Estuary

Under SLR, the net fluxes of DOC increase significantly from the upstream to the downstream locations, which can reach 53.1% in the West Point (Fig. 5-9); and the next fluxes increase by 18.8%, and 6.8% across the Clay Bank, and Gloucester Point, respectively in the downstream York River. The increase of net DOC fluxes is much smaller downstream than upstream Pamunkey River, where extensive marshes and shallow water habitats exist. The changes of net DOC fluxes are the results of changing estuarine circulation, pelagic PP, benthic algae, and marsh contributions. Besides the enhanced circulation, which tends to increase the outfluxes from the upper productive layer. The increase in DOC from pelagic PP contributes significantly to the whole budget and the net fluxes. On the other hand, the lower bottom DO (Fig. 5-10b) along with deeper water depth (Fig. 5-10a) and more consumption from the increased DOC from pelagic and benthic algae, slows down the oxidation of detritus of tidal marshes, which further released more DOC. The extended tidal flooding area and longer duration under SLR enhance the exchange of the material between the marsh and the open water. Although more particulate matter is trapped in the marsh, more DOC is released and transported to the adjacent channel.

Both DIN and PO_4^{3-} fluxes increase, but the increases are in different magnitudes. For example, DIN and PO_4^{3-} fluxes increase by13.3% and 56.8%, respectively at West Point. This is mainly due to the change in nutrient recycling and transformation. NH_4^+ is the major driver of increased DIN flux along the Pamunkey River since NO_3^- mostly decreases (Fig. 5-4cdf). The increase of net PO_4^{3-} fluxes from upstream to the downstream is larger than the DIN and particularly higher in the region adjacent to large tidal marshes (Fig. 5-9c). Both the lower DO and increasing salinity depresses the nitrification process, which in turn prompts the NH_4^+. The lower DO is also favorable to denitrification, which releases nitrogen gas and lowers the increase of DIN fluxes compared with the phosphate (Fig. 5-9 and Fig. 5-10d). The overall lower DO promotes more phosphate release from the sediment. Each low-DO event at low tide brings a pulse of phosphate and these dissolved nutrients are exported in phase with tidal fluctuation (Fig. 5-10c).

5.7 Summary and conceptual diagram of the impacts of SLR on the York River Estuary

We utilized a 3D unstructured-grid model (SCHISM-ICM-Marsh) to investigate the responses of the tidal marshes and the estuarine biochemical processes to SLR in the York River Estuary. The SLR scenarios are conducted with the assumption that the tidal marshes can keep up with the SLR. SLR affects the estuary through multiple biochemical processes interacting with each other directly or indirectly (Fig. 5-11). Although the increased tidal range under SLR slightly depresses the marsh biomass and productivity by increasing the inundation stress, the prolonged inundation over marsh beds enhances the material exchange. The material exchange between the tidal marshes and the adjacent channels interacts with the phytoplankton, nutrient, and oxygen dynamics in the estuary. Pelagic PP increases under SLR due to increased shallow

water habitat area and enhanced utilization of light supply. Therefore, larger PP leads to larger DOC and thus water column respirations. Bottom DO is generally at a lower level in the upstream channel and tidal marsh beds under SLR, which further increases the DOC release from the benthic algae and marsh detritus by slowing down the local oxidation during the increased inundation period. Prolonged low-DO events increase the phosphate release from the sediment. Decrease in DO level and increase in saltwater intrusion slows down the nitrification, therefore sediment ammonium release increases. In addition, lower DO levels prompt denitrification rates, which removes part of the nitrogen out of the estuary. Overall, the impacts on DIN are relatively minor compared with the others. On the other hand, bottom DO in the lower York River tends to slightly increase because of the increased pelagic PP and gravitational circulation. For the sake of simplicity, the current study only considers the impact of SLR and neglects other possible impacts such as the change in land use, the adaption of marsh plants to the changing environment, or the temperature change. Also, this study only focuses on the ideal case that the tidal marshes keep up with the SLR, without explicitly investigating the response of the estuary if there are geomorphological changes on the shoreline or the tidal marsh habitats.

Literature Cited

Axelrad, D.M., Moore, K.A. and Bender, M.E., 1976. Nitrogen phosphorus and carbon flux in Chesapeake Bay marshes.

Bates, B., Kundzewicz, Z. and Wu, S., 2008. *Climate change and water*. Intergovernmental Panel on Climate Change Secretariat.

Boon, J.D., 2012. Evidence of sea level acceleration at US and Canadian tide stations, Atlantic Coast, North America. *Journal of Coastal Research*, *28*(6), pp.1437-1445.

Bridgham, S.D., Megonigal, J.P., Keller, J.K., Bliss, N.B. and Trettin, C., 2006. The carbon balance of North American wetlands. *Wetlands*, *26*(4), pp.889-916.

Brooks, T.J., 1983. Pamunkey River slack water data report: temperature, salinity, dissolved oxygen, 1970-1980.

Cai, X., Zhang, Y.J., Shen, J., Wang, H., Wang, Z., Qin, Q. and Ye, F., 2020. A Numerical Study of Hypoxia in Chesapeake Bay Using an Unstructured Grid Model: Validation and Sensitivity to Bathymetry Representation. *JAWRA Journal of the American Water Resources Association*.

Cai, X., Shen, J., Zhang, Y.J., Qin, Q., Wang, Z. and Wang, H., 2021. Impacts of Sea-Level Rise on Hypoxia and Phytoplankton Production in Chesapeake Bay: Model Prediction and Assessment. *JAWRA Journal of the American Water Resources Association*.

Cai, X., Qin, Q., Shen, J. and Zhang, Y.J., 2022. Bifurcate responses of tidal range to sea-level rise in estuaries with marsh evolution. *Limnology and Oceanography Letters*.

Cerco, C.F. and Cole, T.M., 1994. CE-QUAL-ICM: a three-dimensional eutrophication model, version 1.0. User's Guide. *US Army Corps of Engineers Waterways Experiments Station, Vicksburgh, MS*.

Cerco, C.F. and Seitzinger, S.P., 1997. Measured and modeled effects of benthic algae on eutrophication in Indian River-Rehoboth Bay, Delaware. *Estuaries*, *20*(1), pp.231-248.

Cerco, C.F. and Tian, R., 2021. Impact of Wetlands Loss and Migration, Induced by Climate Change, on Chesapeake Bay DO Standards. *JAWRA Journal of the American Water Resources Association*.

Chambers, R.M., 1992. A flucturing water-level chamber for biogeochemical experiments in tidal marshes. *Estuaries*, *15*(1), pp.53-58.

Chassignet, E.P., Hurlburt, H.E., Smedstad, O.M., Halliwell, G.R., Hogan, P.J., Wallcraft, A.J., Baraille, R. and Bleck, R., 2007. The HYCOM (hybrid coordinate ocean model) data assimilative system. *Journal of Marine Systems*, *65*(1-4), pp.60-83.

Davies, S.B., 2004. Vegetation dynamics of a tidal freshwater marsh: Long-term and inter-annual variability and their relationship to salinity.

Chmura, G.L., Anisfeld, S.C., Cahoon, D.R. and Lynch, J.C., 2003. Global carbon sequestration in tidal, saline wetland soils. *Global biogeochemical cycles*, *17*(4).

Craft, C., Clough, J., Ehman, J., Joye, S., Park, R., Pennings, S., Guo, H. and Machmuller, M., 2009. Forecasting the effects of accelerated sea-level rise on tidal marsh ecosystem services. *Frontiers in Ecology and the Environment*, *7*(2), pp.73-78.

Cronin, W.B., 1971. Volumetric, areal, and tidal statistics of the Chesapeake Bay estuary and its tributaries. *Chesapeake Bay Institute, Special Report 20*, Johns Hopkins University, Washington, D.C., 135p

Dauer, D., Marshall, H., Donat, J., Lane, M., Morton, P., Doughten S. and Hoffman, F., 2005. Status and trends in water quality and living resources in the Virginia Chesapeake Bay: York River (1985-2004). Final Report. Virginia Department of environmental Quality, Richmond, VA., 63p.

Du, J., Shen, J., Zhang, Y.J., Ye, F., Liu, Z., Wang, Z., Wang, Y.P., Yu, X., Sisson, M. and Wang, H.V., 2018. Tidal response to sea-level rise in different types of estuaries: The importance of length, bathymetry, and geometry. *Geophysical Research Letters*, *45*(1), pp.227-235.

Flick, R.E., Murray, J.F. and Ewing, L.C., 2003. Trends in United States tidal datum statistics and tide range. *Journal of Waterway, Port, Coastal, and Ocean Engineering*, *129*(4), pp.155-164.

Friedrichs, C.T., 2009. York River physical oceanography and sediment transport. *Journal of Coastal Research*, *2009*(10057), pp.17-22.

Hall, G.F., Hill, D.F., Horton, B.P., Engelhart, S.E. and Peltier, W.R., 2013. A high-resolution study of tides in the Delaware Bay: Past conditions and future scenarios. *Geophysical Research Letters*, *40*(2), pp.338-342.

Holleman, R.C. and Stacey, M.T., 2014. Coupling of sea level rise, tidal amplification, and inundation. *Journal of Physical Oceanography*, *44*(5), pp.1439-1455.

Hong, B., Liu, Z., Shen, J., Wu, H., Gong, W., Xu, H. and Wang, D., 2020. Potential physical impacts of sea-level rise on the Pearl River Estuary, China. *Journal of Marine Systems*, *201*, p.103245.

Irby, I.D., Friedrichs, M.A., Da, F. and Hinson, K.E., 2018. The competing impacts of climate change and nutrient reductions on dissolved oxygen in Chesapeake Bay. *Biogeosciences*, *15*(9), pp.2649-2668.

Jordan, T.E., Correll, D.L. and Whigham, D.F., 1983. Nutrient flux in the Rhode River: tidal exchange of nutrients by brackish marshes. *Estuarine, Coastal and Shelf Science*, *17*(6), pp.651-667.

Jordan, T.E., Cornwell, J.C., Boynton, W.R. and Anderson, J.T., 2008. Changes in phosphorus biogeochemistry along an estuarine salinity gradient: The iron conveyer belt. *Limnology and Oceanography*, *53*(1), pp.172-184.

Kuo, A.Y. and Neilson, B.J., 1987. Hypoxia and salinity in Virginia estuaries. *Estuaries*, *10*(4), pp.277-283.

Lee, S.B., Li, M. and Zhang, F., 2017. Impact of sea level rise on tidal range in Chesapeake and Delaware Bays. *Journal of Geophysical Research: Oceans*, *122*(5), pp.3917-3938.

Mesinger, F., DiMego, G., Kalnay, E., Mitchell, K., Shafran, P.C., Ebisuzaki, W., Jović, D., Woollen, J., Rogers, E., Berbery, E.H. and Ek, M.B., 2006. North American regional reanalysis. *Bulletin of the American Meteorological Society*, *87*(3), pp.343-360.

Mitchell, M., Herman, J., Bilkovic, D.M. and Hershner, C., 2017. Marsh persistence under sea-level rise is controlled by multiple, geologically variable stressors. *Ecosystem Health and Sustainability*, *3*(10), p.1379888.

Neubauer, S.C. and Craft, C.B., 2009. Global change and tidal freshwater wetlands: scenarios and impacts. *Tidal freshwater wetlands*, pp.253-266.

Ni, W., Li, M. and Testa, J.M., 2020. Discerning effects of warming, sea level rise and nutrient management on long-term hypoxia trends in Chesapeake Bay. *Science of the Total Environment*, *737*, p.139717.

Nichols, M.M., Kim, S.C., and Brouwer, C.M., 1991. Sediment characterization of the Chesapeake Bay and its tributaries, Virginian Province. National estuarine inventory: supplement. NOAA Strategic Assessment Branch. 88p.

Pelling, H.E., Green, J.M. and Ward, S.L., 2013. Modelling tides and sea-level rise: To flood or not to flood. *Ocean Modelling*, *63*, pp.21-29.

Reay, W.G., 2009. Water quality within the York River estuary. *Journal of Coastal Research*, (10057), pp.23-39.

Reed, D.J., 1990. The impact of sea-level rise on coastal salt marshes. *Progress in Physical Geography*, *14*(4), pp.465-481.

Reed, D.J., 1995. The response of coastal marshes to sea-level rise: Survival or submergence?. *Earth Surface processes and landforms*, *20*(1), pp.39-48.

Rice, K., Hong, B., and Shen, J., 2012. Change of salinity in the James River due to sea level rise. *Journal of Environmental Management*, (111), 61-69

Ross, A.C., Najjar, R.G., Li, M., Lee, S.B., Zhang, F. and Liu, W., 2017. Fingerprints of sea level rise on changing tides in the Chesapeake and Delaware Bays. *Journal of Geophysical Research: Oceans*, *122*(10), pp.8102-8125.

Rysgaard, S., Thastum, P., Dalsgaard, T., Christensen, P.B. and Sloth, N.P., 1999. Effects of salinity on NH 4+ adsorption capacity, nitrification, and denitrification in Danish estuarine sediments. *Estuaries*, *22*(1), pp.21-30.

Santoro, A.E., 2010. Microbial nitrogen cycling at the saltwater–freshwater interface. *Hydrogeology Journal*, *18*(1), pp.187-202.

Shen, J. and Haas, L., 2004. Calculating age and residence time in the tidal York River using three-dimensional model experiments. *Estuarine, Coastal and Shelf Science*, *61*(3), pp.449-461.

Shenk, G.W. and Linker, L.C., 2013. Development and application of the 2010 Chesapeake Bay watershed total maximum daily load model. *JAWRA Journal of the American Water Resources Association*, *49*(5), pp.1042-1056.

Sin, Y., Wetzel, R.L. and Anderson, I.C., 1999. Spatial and temporal characteristics of nutrient and phytoplankton dynamics in the York River estuary, Virginia: analyses of long-term data. *Estuaries*, *22*(2), pp.260-275.

Sin, Y., Wetzel, R.L., Lee, B.G. and Kang, Y.H., 2006. Integrative ecosystem analyses of phytoplankton dynamics in the York River estuary (USA). *Hydrobiologia*, *571*(1), pp.93-108.

Sprague, L.A., 2000. *Factors affecting nutrient trends in major rivers of the Chesapeake Bay watershed* (No. 4218). US Department of the Interior, US Geological Survey.

St-Laurent, P., Friedrichs, M.A., Li, M. and Ni, W., 2019. Impacts of sea level rise on hypoxia in the Chesapeake Bay: A model intercomparison. *Report to Virginia Tech and Chesapeake Bay Program*.

Sutter, L.A., 2014. Effects of Saltwater Intrusion on Vegetation Dynamics and Nutrient Pools in Low-Salinity Tidal Marshes, Pamunkey River (Virginia, USA).

Wang, P., Linker, L., Wang, H., Bhatt, G., Yactayo, G., Hinson, K. and Tian, R., 2017, August. Assessing water quality of the Chesapeake Bay by the impact of sea level rise and warming. In *IOP Conference Series: Earth and Environmental Science* (Vol. 82, No. 1, p. 012001). IOP Publishing.

Wang, Y. and Shen, J., 2020. A Modeling Study on the Influence of Sea-Level Rise and Channel Deepening on Estuarine Circulation and Dissolved Oxygen Levels in the Tidal James River, Virginia, USA. *Journal of Marine Science and Engineering*, *8*(11), p.950.

Zhang, Y.J., Ye, F., Stanev, E.V. and Grashorn, S., 2016. Seamless cross-scale modeling with SCHISM. *Ocean Modelling*, *102*, pp.64-81.

Figures for Chapter 5

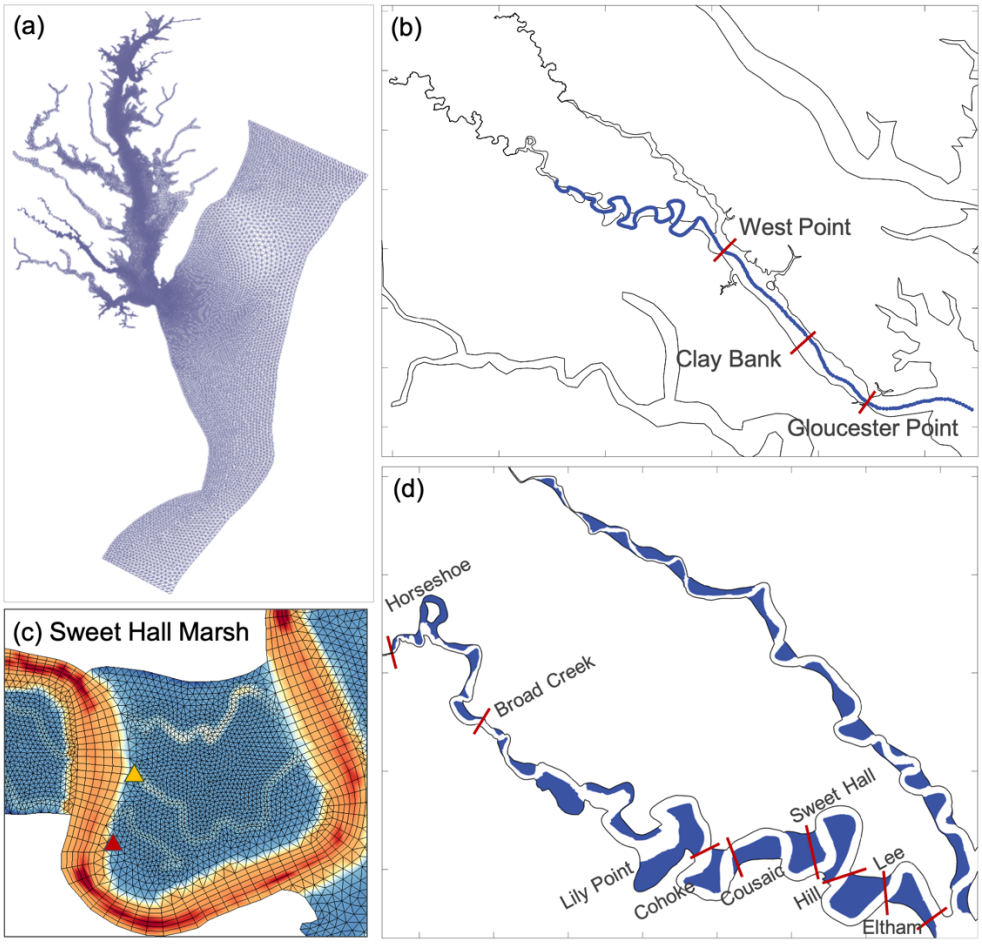

Fig. 5-1: (a) Model domain with local refinement in the York River Estuary. (b) The York River Estuary with a blue line that denotes the along-channel transect used in this study. (c) Sweet Hall Marsh. Red and yellow triangles denote the sampling points of diurnal processes in the marsh bed and creek, respectively. (d) Extensive and fringing marshes in the study area. The red lines in panels (c) and (d) denote the transects to calculate the material exchange in this study. Based on the USGS topography map, the blue polygons mark the marshes along the Pamunkey and Mattaponi Rivers.

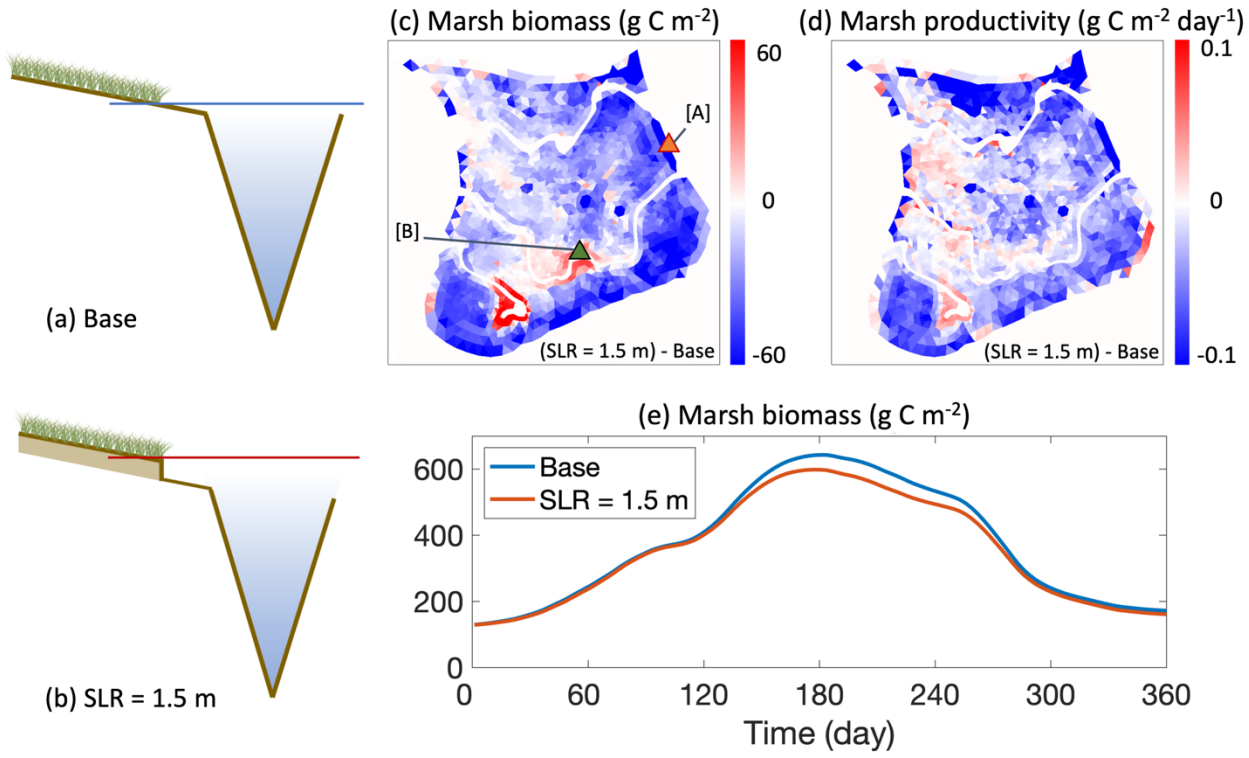

Fig. 5-2: (a, b) Diagrams of the Base and SLR scenarios, where marsh keeps up with the rising sea-level of 1.5 m. (c, d) Absolute difference ((SLR = 1.5 m) – Base) of annual averages of marsh biomass and net marsh productivity in Sweet Hall Marsh. Orange and green triangles in (c) denote the sampling points for analysis in Fig. 5-3. (e) Spatial averages of marsh biomass in the York River Estuary in Base and SLR = 1.5 m Scenario. The marsh area is denoted in Fig. 5-1.

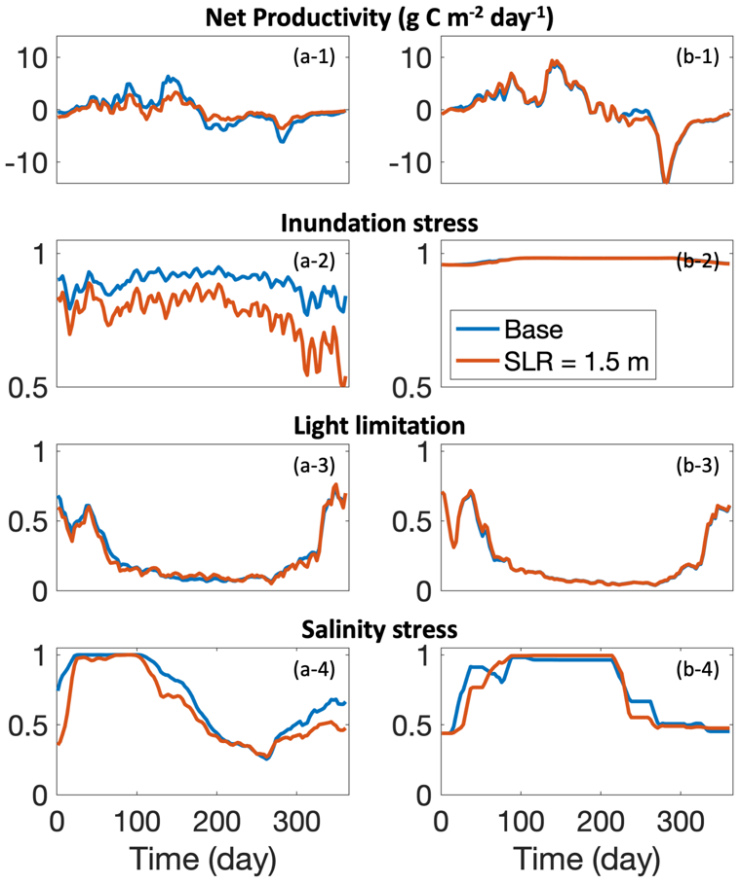

Fig. 5-3: Response of marsh net productivity, inundation stress, light limitation, and salinity stress to SLR in multiple sampling locations in the Sweet Hall Marsh. Sampling locations are denoted in Fig. 5-2c. The marsh biomass and productivity decrease at location (a) and increase at location (b).

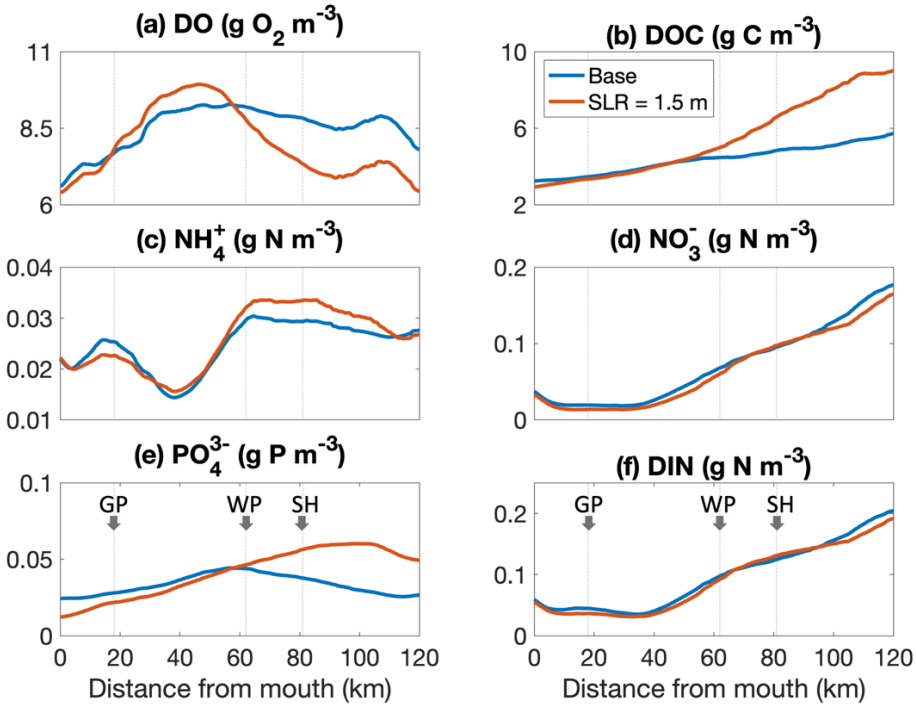

Fig. 5-4: Comparisons of Base Scenario and SLR scenario of 1.5 m of bottom dissolved oxygen and other surface water properties, including ammonia, nitrate, phosphate, and dissolved organic carbon, along the channel of Pamunkey and York Rivers. The along-channel transect is denoted in Fig. 5-1. Locations of Gloucester Point, West Point, and Sweet Hall are denoted in panel (e) along with grey dotted lines in all the panels.

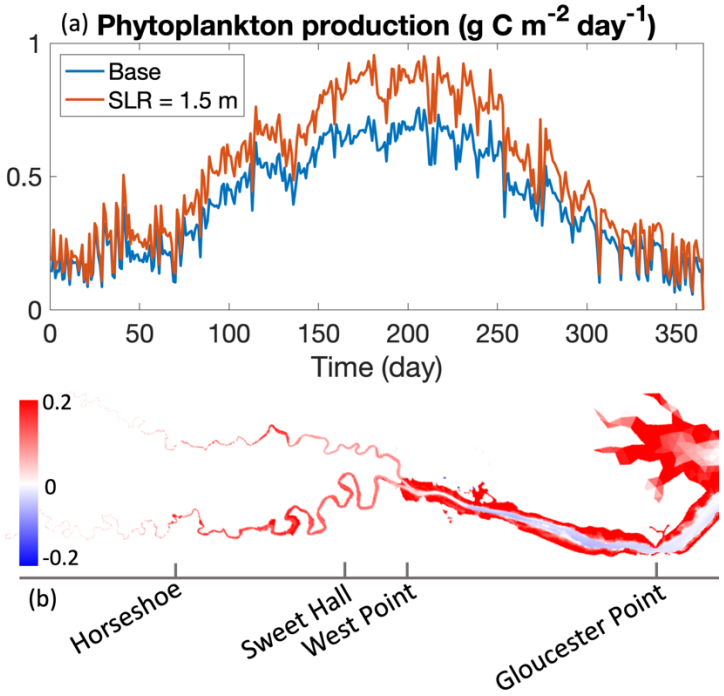

Fig. 5-5: (a) Spatially averaged daily phytoplankton production in the York River Estuary. (b) Difference of annual-averaged phytoplankton production between SLR = 1.5 m and Base Scenario (SLR-Base).

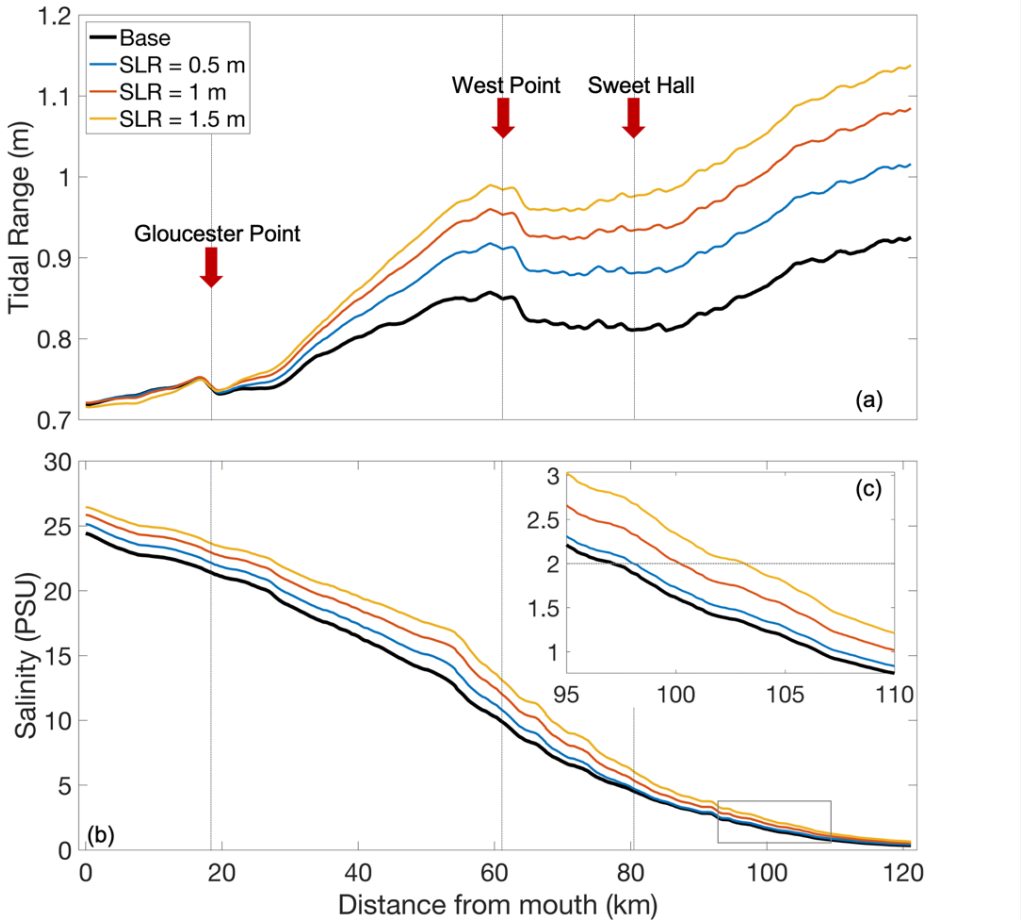

Fig. 5-6: Response of (a) tidal range and (b) bottom salinity to SLR along the channel of Pamunkey and York River as denoted in Fig. 5-1. (c) Zoom in at locations of limitations of saltwater intrusion.

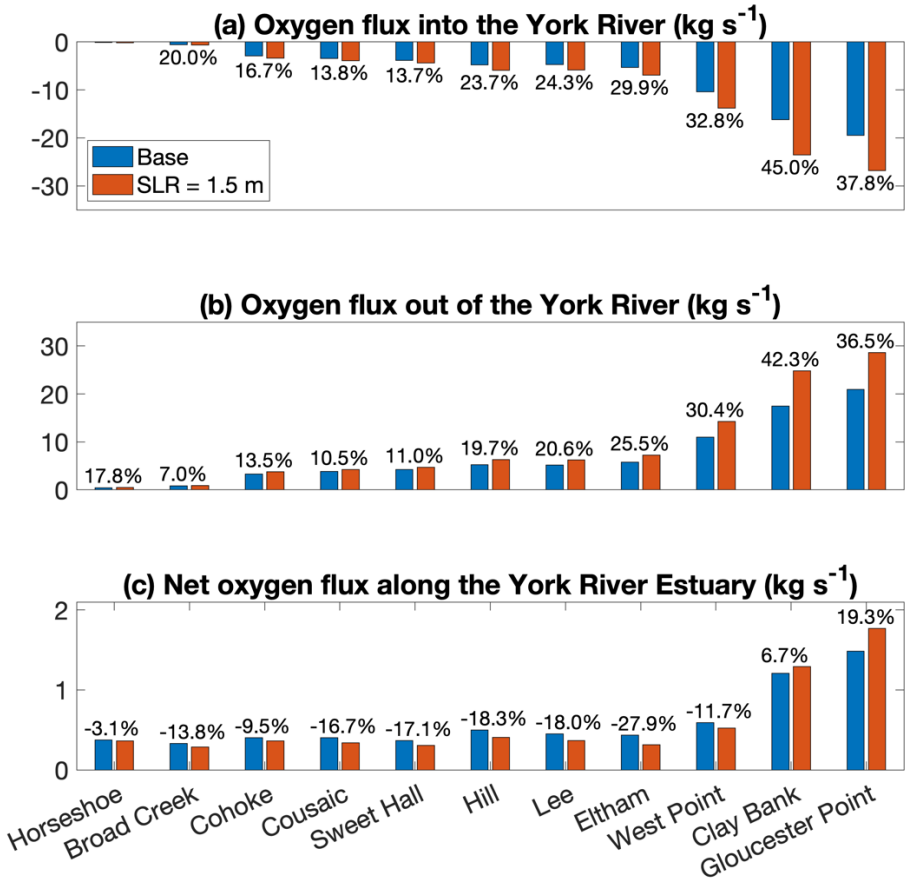

Fig. 5-7: Averages of annual oxygen flux from the upstream of Pamunkey River to the York River mouth in the Base Scenario and SLR scenario of 1.5 m. Locations of these cross-sections are denoted in Fig. 5-1cd. Percentage denoted in each panel equals to (SLR-Base)/Base×100%. In these cross-sections, the influx (negative) corresponds to the direction from the river mouth to the upstream and the outflux (positive) corresponds to the direction from upstream to downstream.

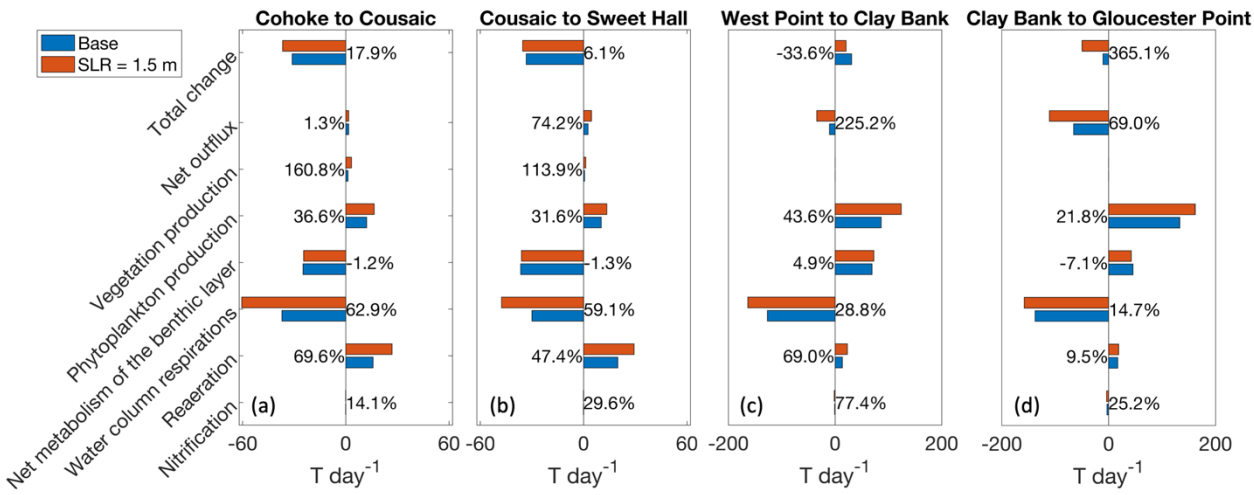

Fig. 5-8: Averaged contribution of each physical or biological process to the DO budget from June to August in the sections where the interfaces are denoted in Fig. 5-1cd. The change percentage (SLR-Base)/Base are labeled.

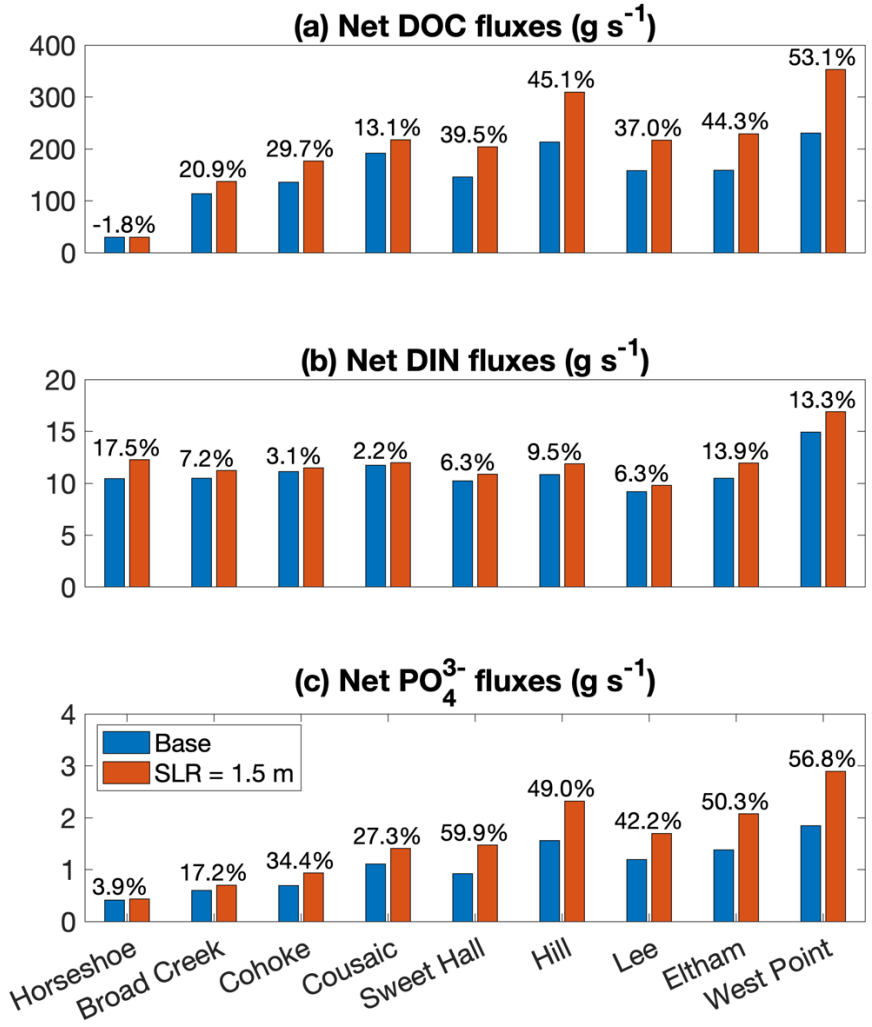

Fig. 5-9: Net fluxes of (a) dissolved organic carbon, (b) dissolved inorganic nitrogen, and (c) total inorganic phosphate from the upstream of Pamunkey River to the downstream in the Base Scenario and SLR scenario of 1.5 m. Locations of these cross-sections are denoted in Fig. 5-1d. Percentage denoted in each panel equals to (SLR-Base)/Base×100%. In these cross-sections, the influx (negative) refers to the direction from the river mouth to the upstream and the outflux (positive) refers to the direction from upstream to downstream.

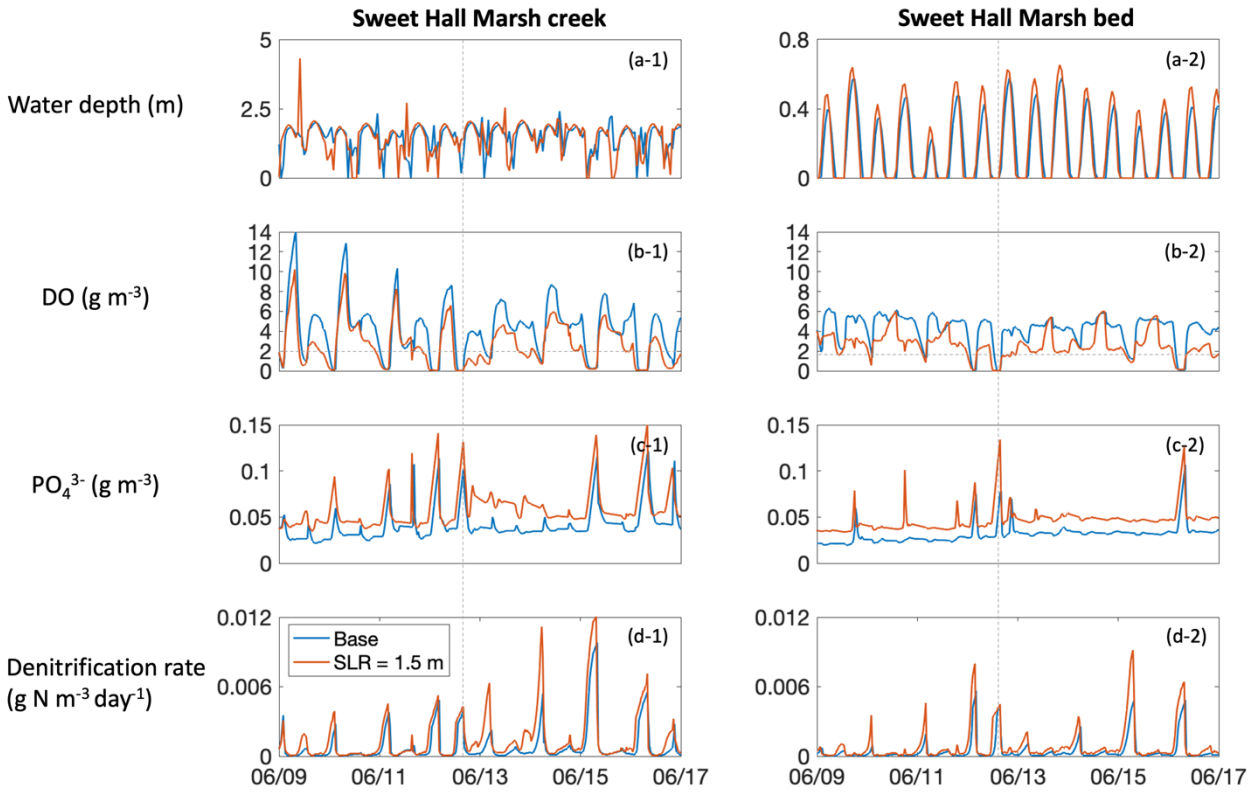

Fig. 5-10: A 8-day window in summer of the simulated water properties (a) local water depth, (b) dissolved oxygen, (c) phosphate, and (d) denitrification rates at two Sweet Hall Marsh stations respectively in the tidal creek and marsh bed, where only the marsh bed had 1.5 m of vertical accretion under SLR. These two stations are denoted in Fig. 5-1c. The grey dotted horizontal line in (b) denotes a dissolved oxygen concentration of 2 g m-3. Grey dotted vertical lines denote moments of a typical low tide along with low DO, high phosphate, and high denitrification loss.

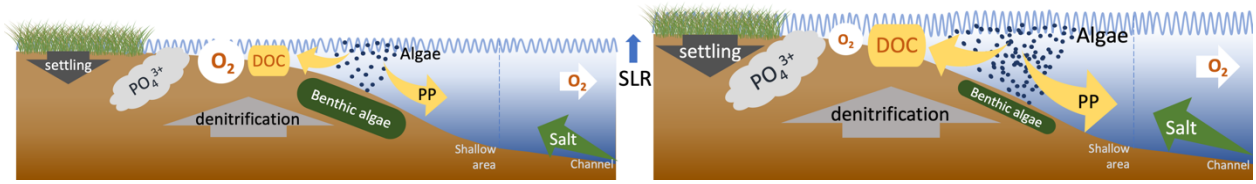

Fig. 5-11: Conceptual diagram of the impacts of SLR on the biochemical processes in an estuary with extensive marshes

6. Conclusions and future directions

This dissertation fulfilled two major goals of both model development and model application. The development of a new comprehensive water quality model for the Chesapeake Bay includes both a high-resolution water quality model using unstructured grids in the water column and a marsh model in the intertidal zone for the vegetations (Chapter 2 and 4). These two components are linked and they are also coupled with a sediment diagenesis model. Use of unstructured grids provides the flexibility for local refinements to fit complex geometry over both large and small scales. Comparisons with observations demonstrate that it is important to use realistic bathymetry (in combination with high mesh resolution) to provide accurate simulations for physical and biogeochemical processes, and to correctly predict the impact of sea-level rise on future summertime hypoxia, which is of great concern for the Bay management. By integrating hydrodynamics, water quality kinetic processes, sediment diagenesis, and vegetation effects in the model simulation, this newly developed modeling system extends its simulations beyond the water column state variables and can be used for real environment study. The seamless cross-scale capability of SCHISM-ICM-Marsh can be effectively utilized as a powerful tool for adaptive management. However, since the model development is based on the current knowledge of understanding of the water quality processes and available data, more study and improvement are needed in the future as the knowledge evolves.

The second goal achieved by this dissertation is the application of this new model to study the impacts of sea-level rise on the biochemical processes in the Bay, such as hypoxia, nutrient dynamics, and phytoplankton production (Chapter 3). Changes in peak summer hypoxic volume (HV) and phytoplankton production are estimated under the SLR condition. Both the altered physical processes (e.g., enhanced stratification and enlarged volume below the

pycnocline) and the higher respiration under SLR contribute to the enlarged HV. The increase in water depth increases light utilization in shallow waters in many tributaries, where the whole water column is within the euphotic zone, to fuel phytoplankton production. Following the study on the main stem, this dissertation also investigated the response of the York River Estuary (a typical tributary in the Bay) to SLR with the roles of tidal marshes considered (Chapter 5). This modeling study demonstrates that the tidal marshes play an important role in the estuarine biochemical processes and contribute to the nonlinear interactions of these processes under SLR. This study focuses on the tidal marshes as an important component of the shallow water living resources, while other primary producers, such as the SAV and macroalgae, can also be included in the future for a more comprehensive study. In addition, the physical environment can be more realistically modeled in future studies by including more processes such as waves that significantly impact mixing, resuspension, and transport in the shallow systems.

VITA

Xun (Nicole) Cai

Born in Changshu (常熟), Jiangsu, China. Earned a B.S. in Oceanography from Nanjing University in 2015. Earned a M.S. in Marine Science from William & Mary in 2018. Entered Ph.D. program at the Virginia Institute of Marine Science / William & Mary School of Marine Science in 2018.